AD-A258 823



AFIT/GA/ENY/92D-07

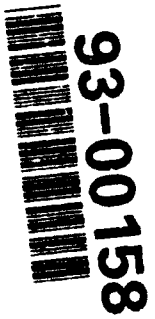
AN EXPERIMENTAL DETERMINATION OF THE EFFECTS OF BLENDING COLLOCATED AND NON-COLLOCATED SENSOR MEASUREMENTS TO CONTROL A FLEXIBLE STRUCTURE

THESIS

RICHARD G. COBB, Captain, USAF

AFIT/GA/ENY/92D-07

DTIC
ELECTE
JAN 0 6 1993
S B D



93-00158

Approved for public release; distribution unlimited.

93 1 04 016

AFIT/GA/ENY/92D-07

AN EXPERIMENTAL DETERMINATION OF THE EFFECTS OF BLENDING COLLOCATED AND NON-COLLOCATED SENSOR MEASUREMENTS TO CONTROL A FLEXIBLE STRUCTURE

THESIS

Presented to the Faculty of the School of Engineering

of the Air Force Institute of Technology

Air University

In Partial Fulfillment of the

Requirements for the Degree of

Master of Science in Astronautical Engineering

RICHARD G. COBB, B.S.

Captain, USAF

December 1992

Approved for public release; distribution unlimited.

REPORT DOCUMENTATION PAGE

Form Approved
OMB No. 0704-0188

Public reporting burden for this collection of information is estimated to average 1 hour per response, including the time for reviewing instructions, searching existing data sources, gathering and maintaining the data needed, and completing and reviewing the collection of information. Send comments regarding this burden estimate or any other aspect of this collection of information, including suggestions for reducing this burden, to Washington Headquarters Services, Directorate for Information Operations and Reports, 1215 Jefferson Davis Highway, Suite 1204, Arlington, VA 22202-4302, and to the Office of Management and Budget, Paperwork Reduction Project (0704-0188), Washington, DC 20503.

1. AGENCY USE ONLY (Leave blank)	2. REPORT DATE	3. REPORT TYPE AND DATES COVERED
	December 1992	Master's Thesis

4. TITLE AND SUBTITLE
AN EXPERIMENTAL DETERMINATION OF THE EFFECTS OF BLENDING COLLOCATED AND NON-COLLOCATED SENSOR MEASUREMENTS TO CONTROL A FLEXIBLE STRUCTURE

5. FUNDING NUMBERS

6. AUTHOR(S)
Richard G. Cobb, Captain, USAF

7. PERFORMING ORGANIZATION NAME(S) AND ADDRESS(ES)
Air Force Institute of Technology
WPAFB OH 45433-6583

8. PERFORMING ORGANIZATION REPORT NUMBER
AFIT/GA/ENY/92D-07

9. SPONSORING/MONITORING AGENCY NAME(S) AND ADDRESS(ES)
Kevin Slimak
OL-AC PL/VTS
Edwards AFB CA 93524-7620

10. SPONSORING/MONITORING AGENCY REPORT NUMBER

11. SUPPLEMENTARY NOTES
Approved for public release; distribution unlimited

12a. DISTRIBUTION/AVAILABILITY STATEMENT

12b. DISTRIBUTION CODE

13. ABSTRACT *(Maximum 200 words)*

An experimental investigation was performed controlling a cantilevered beam in bending using proportional feedback on a blend of collocated and non-collocated sensor measurements using a single actuator. Exact transfer functions between the control input and the measurements were developed and compared to the finite element method. By analyzing the open loop pole-zero locations as a function of the measurement blending, insight into the closed loop behavior is obtained. Minimum phase behavior can be maintained for a range of the blending ratio. Results using blended control were compared to both proportional collocated feedback and compensated collocated feedback using LQG methods. The comparison was then extended to a theoretical investigation using the blended measurements on a free-free torsional model analogous to a gimbal. Advantages and limitations of using blended measurements are presented.

14. SUBJECT TERMS	15. NUMBER OF PAGES
collocated, non-collocated, flexible structures, active control, sensors, actuators	133
	16. PRICE CODE

17. SECURITY CLASSIFICATION OF REPORT	18. SECURITY CLASSIFICATION OF THIS PAGE	19. SECURITY CLASSIFICATION OF ABSTRACT	20. LIMITATION OF ABSTRACT
Unclassified	Unclassified	Unclassified	UL

GENERAL INSTRUCTIONS FOR COMPLETING SF 298

The Report Documentation Page (RDP) is used in announcing and cataloging reports. It is important that this information be consistent with the rest of the report, particularly the cover and title page. Instructions for filling in each block of the form follow. It is important to ***stay within the lines*** to meet ***optical scanning requirements***.

Block 1. Agency Use Only *(Leave blank)*.

Block 2. Report Date. Full publication date including day, month, and year, if available (e.g. 1 Jan 88). Must cite at least the year.

Block 3. Type of Report and Dates Covered. State whether report is interim, final, etc. If applicable, enter inclusive report dates (e.g. 10 Jun 87 - 30 Jun 88).

Block 4. Title and Subtitle. A title is taken from the part of the report that provides the most meaningful and complete information. When a report is prepared in more than one volume, repeat the primary title, add volume number, and include subtitle for the specific volume. On classified documents enter the title classification in parentheses.

Block 5. Funding Numbers. To include contract and grant numbers; may include program element number(s), project number(s), task number(s), and work unit number(s). Use the following labels:

C	- Contract	**PR**	- Project
G	- Grant	**TA**	- Task
PE	- Program Element	**WU**	- Work Unit Accession No.

Block 6. Author(s). Name(s) of person(s) responsible for writing the report, performing the research, or credited with the content of the report. If editor or compiler, this should follow the name(s).

Block 7. Performing Organization Name(s) and Address(es). Self-explanatory.

Block 8. Performing Organization Report Number. Enter the unique alphanumeric report number(s) assigned by the organization performing the report.

Block 9. Sponsoring/Monitoring Agency Name(s) and Address(es). Self-explanatory.

Block 10. Sponsoring/Monitoring Agency Report Number. *(If known)*

Block 11. Supplementary Notes. Enter information not included elsewhere such as: Prepared in cooperation with...; Trans. of...; To be published in.... When a report is revised, include a statement whether the new report supersedes or supplements the older report.

Block 12a. Distribution/Availability Statement. Denotes public availability or limitations. Cite any availability to the public. Enter additional limitations or special markings in all capitals (e.g. NOFORN, REL, ITAR).

- **DOD** - See DoDD 5230.24, "Distribution Statements on Technical Documents."
- **DOE** - See authorities.
- **NASA** - See Handbook NHB 2200.2.
- **NTIS** - Leave blank.

Block 12b. Distribution Code.

- **DOD** - Leave blank.
- **DOE** - Enter DOE distribution categories from the Standard Distribution for Unclassified Scientific and Technical Reports.
- **NASA** - Leave blank.
- **NTIS** - Leave blank.

Block 13. Abstract. Include a brief *(Maximum 200 words)* factual summary of the most significant information contained in the report.

Block 14. Subject Terms. Keywords or phrases identifying major subjects in the report.

Block 15. Number of Pages. Enter the total number of pages.

Block 16. Price Code. Enter appropriate price code *(NTIS only)*.

Blocks 17. - 19. Security Classifications. Self-explanatory. Enter U.S. Security Classification in accordance with U.S. Security Regulations (i.e., UNCLASSIFIED). If form contains classified information, stamp classification on the top and bottom of the page.

Block 20. Limitation of Abstract. This block must be completed to assign a limitation to the abstract. Enter either UL (unlimited) or SAR (same as report). An entry in this block is necessary if the abstract is to be limited. If blank, the abstract is assumed to be unlimited.

Acknowledgements

In any independent research effort such as the AFIT Master's Thesis, independent is somewhat of a misnomer. I wish to thank Mr Jay Anderson and Mr Nicholas Yardich Jr. for ensuring I had the proper equipment and support in conducting my research. My sincerest appreciation goes towards my thesis advisor Dr Brad Liebst for his unending support in helping me through some of the hurdles of experimental work.

Most of all, I'd like to thank my wife Lisa. She sympathized with my problems and listened as I thought aloud, and never let on she wasn't interested. She helped maintain the delicate balance between family and school.

Richard G. Cobb

DTIC QUALITY INSPECTED 6

Accession For	
NTIS GRA&I	☑
DTIC TAB	☐
Unannounced	☐
Justification	
By	
Distribution/	
Availability Codes	
Dist	Avail and/or Special
A-1	

Table of Contents

Acknowledgements ii

List of Figures v

List of Tables viii

List of Symbols ix

Abstract xi

I. Introduction 1-1

II. Background 2-1

Exact Transfer Functions 2-4
Exact Solution for a Free-Free Beam 2-5
Exact Solution for a Cantilevered Beam with End Excitation 2-6
Exact Solution for a Cantilevered Beam with Arbitrary Excitation Point 2-8
Exact Pole-Zero Patterns 2-10
Performance Characteristics of Collocated and Non-Collocated Systems 2-14
Blending Method 2-16

III. Characterization of Experimental Equipment . . . 3-1

Structure 3-3
Analytical Model Development 3-4
Finite Element Method Model Validation 3-9
Actuator 3-11
Controller 3-13
Measurements 3-14
Closed Loop Verification 3-18
Modal Measurements 3-23

IV. Blended Control on ACB with End Mass 4-1

Open Loop Response 4-1
Closed Loop Performance Criteria 4-8
Stability Comparisons 4-9
Bandwidth Comparisons 4-11
Root Mean Square Response 4-17

Closed Loop Results 4-19
Comparison of Blended to LQG Methods 4-23
LQG Theory 4-24
Results 4-27
Conclusions 4-30

V. Control of ACB with End Mass Removed 5-1

Mode Shape Comparisons 5-1
Open Loop Response 5-3
Closed Loop Results 5-6
Conclusions 5-10

VI. Blended Method Applied to a Gimbal Structure . . 6-1

Model Development 6-1
Closed Loop Performance Comparison 6-6
Conclusions 6-12

VII. Conclusions and Recommendations 7-1

Appendix A: Calibration Data A-1

Appendix B: State-Space Models B-1

Appendix C: MATLAB Finite Element Program C-1

Appendix D: Analog Gain Control D-1

Bibliography BIB-1

Vita V-1

List of Figures

Figure		Page
2.1	Sensor Locations on a Gimbal	2-3
2.2	Problem Setup for Beam with Arbitrary Excitation Point.	2-9
2.3	Collocated Pole-Zero Pattern of a Cantilevered Beam with End Excitation.	2-13
2.4	Pole-Zero Pattern for a Cantilevered Beam with Endpoint Excitation and the Sensor at the Midpoint	2-13
2.5	Root Locus Using Negative Rate Feedback with a Collocated Sensor on a Cantilevered Beam.	2-15
2.6	Root Locus Using Negative Rate Feedback with a Non-Collocated Sensor on a Cantilevered Beam.	2-15
2.7	Zero Movement as the Blending Ratio is Increased for the Cantilevered Beam with End Excitation.	2-18
2.8	Zero Movement as the Blending Ratio is Increased for the Free-Free Beam.	2-19
3.1	ACB Experimental Configuration.	3-2
3.2	Ten Element Beam Model.	3-6
3.3	Comparison of Predicted and Measured Transfer Functions for the Digital Integrator.	3-17
3.4	Block Diagram of Closed Loop Test Setup with Digital Integration.	3-19
3.5	Root Locus Pattern Using a Collocated Sensor with Delay.	3-21
3.6	Integration Circuit	3-23
3.7	Final Closed Loop Test Setup Block Diagram.	3-24
4.1	Theoretical Open Loop Comparison for the Three Sensor Positions.	4-2

4.2 Open Loop Comparison for the Collocated Sensor (position 5). 4-4

4.3 Open Loop Comparison for the Position Eight Sensor. 4-5

4.4 Open Loop Comparison for the Position Eleven Sensor. 4-6

4.5 Zero Locations for a Blended Measurement of α= 0.35 4-8

4.6 Root Locus Using Collocated Rate Feedback on the ACB with End Mass. 4-9

4.7 Root Locus Using Rate Feedback with the Non-Collocated Sensor on the ACB with End Mass. . . . 4-10

4.8 Open Loop Zero Locations for an Increasing Blending Ratio 4-13

4.9 Feedback Loop Block Diagram. 4-15

4.10 Comparison of RMS Velocity at Position Eight for both Collocated and Blended Feedback. 4-20

4.11 Comparison of Required Control Effort for an Increasing Feedback Gain. 4-21

4.12 Closed Loop Comparison with Matched Control Effort. 4-22

4.13 Closed Loop Comparison using Blended and LQG Compensation. 4-30

5.1 Mode Shapes of ACB with End Mass Installed. . . . 5-2

5.2 Mode Shapes of ACB with End Mass Removed. 5-2

5.3 Open Loop Response of ACB with End Mass Removed for the Collocated Sensor. 5-4

5.4 Open Loop Response for ACB with End Mass Removed for the Non-Collocated Sensor. 5-5

5.5 Open Loop Zero Locations for a Varying Blending Ratio. 5-6

5.6 Comparison of Posiion Eight RMS Velocity for both Collocated and Blended Feedback. 5-7

5.7 Comparison of Control Effort for an Increasing Feedback Gain. 5-8

5.8 Closed Loop Frequency Response Comparison for the ACB Without End Mass. 5-9

6.1 Frequency Response Comparison Between Exact and FEM Model for Collocated Sensor on a Torsional Rod 6-4

6.2 Frequency Response Comparison Between the Exact and FEM model for the Non-Collocated Sensor on a Torsional Rod. 6-5

6.3 Pole-Zero Pattern as the Blending Ratio is Increased for a Torsional Rod. 6-6

6.4 Closed Loop Block Diagram for a Torsional Rod . . 6-7

6.5 Comparison of RMS Value at Midpoint Position for Random Disturbance. 6-8

6.6 Step Response Comparison at Midpoint of Torsional Rod Using Collocated and Blended (α = 0.45) Feedback. 6-9

6.7 Bandwidth Comparison Using Collocated and Blended (α=0.45) Feedback on the Torsional Rod. 6-10

6.8 Step Response at End Point of a Torsional Rod. . 6-11

D.1 Circuit Diagram for Analog Amplifier D-1

D.2 Calibration Curve for Analog Amplifier D-2

List of Tables

Tables		Page
2.1	Pole-Zero Locations for a Beam in Bending	2-12
3.1	ACB Physical Properties	3-4
3.2	Comparison of FEM to Analytical	3-10
4.1	Pole-Zero Locations for ACB with End Mass	4-3
4.2	Modeled and Measured Natural Frequencies	4-5
4.3	Blended Zero Locations for $\alpha = 0.35$	4-7
4.4	Damping Factors (%) for Matched Control Effort .	4-22
4.5	Damping Factors for Blended and LQG Controllers .	4-29
5.1	Pole-Zero Locations for ACB Without End Mass . .	5-4
5.2	Damping Factors (%) for Matched RMS Response . .	5-9
6.1	Pole-Zero Locations for a Torsional Rod	6-4
A.1	Accelerometer Calibrations	A-3
A.2	Integration Circuit Calibration Factors	A-4

List of Symbols

EI beam bending stiffness

V(x,t) transverse displacement of neutral axis of beam

σ mass density per unit length

s Laplace variable

λ eigenvalue

f(s) force input to beam in Laplace domain

δ distance from beam end to excitation point

V_{co} collocated transverse displacement

V_{nc} non-collocated transverse displacement

u control force input

α measurement blending ratio

K gain matrix (or scaler)

y_{co} collocated measurement

y_{nc} non-collocated measurement

M_{ij} element mass matrix

K_{ij} element stiffness matrix

ρ beam density per unit volume

y measurement vector

C matrix transformation between states & measurements

Φ modal matrix

η modal coordinate vector

ω_n diagonal matrix of natural frequencies

ζ damping factor

ξ vector of modal coordinates and first derivatives

A, B, C, D, E, F state-space matrices

f_n natural frequency in Hz

p system pole

z system zero

T digital sample period

M_i magnitude of time response at peak i

r command input

n numerator polynomial

X covariance of states

Q diagonal matrix of white noise intensities

v disturbance noise

w measurement noise

J_i cost function used in LQG

Q_c state weighting matrix

R_c control usage weighting matrix

Q_e process noise covariance matrix

R_e measurement noise covariance matrix

$\hat{x}$ state estimates

L estimator gain matrix

F_{ij} digital controller partition matrices

GJ torsional stiffness

$\theta(x,t)$ rotation angle

T(s) torque input in Laplace domain

$G_c(s)$ lead compensator

Abstract

An experimental investigation was performed controlling a cantilevered beam in bending using proportional feedback on a blend of collocated and non-collocated sensor measurements using a single actuator. Exact transfer functions between the control input and the measurements were developed and compared to the finite element method. By analyzing the open loop pole-zero locations as a function of the measurement blending, insight into the closed loop behavior is obtained. Minimum phase behavior can be maintained for a range of the blending ratio. Results using blended control were compared to both proportional collocated feedback and compensated collocated feedback using LQG methods. The comparison was then extended to a theoretical investigation using the blended measurements on a free-free torsional model analogous to a gimbal. Advantages and limitations of using blended measurements are presented.

AN EXPERIMENTAL DETERMINATION OF THE EFFECTS OF BLENDING COLLOCATED AND NON-COLLOCATED SENSOR MEASUREMENTS TO CONTROL A FLEXIBLE STRUCTURE

I. Introduction

During the design process of a control system, the design team must make tradeoff decisions between such factors as desired performance, design complexity, cost, reliability, and maintainability. An 'optimal' solution would be one which meets performance criteria while minimizing complexity and cost and maximizes reliability and maintainability. Focusing on simplicity, a blended measurement technique is investigated to control a flexible structure and its merits reported.

A system's achievable performance is greatly influenced by the relative placement of sensors and actuators on the structure. A collocated sensor actuator pair corresponds to physically attaching the sensor and the actuator to the same location on the structure. Non-collocation refers to the sensor being physically displaced from the location of the actuator. For flexible structures, using collocation results in a minimum phase system whereas the non-collocated

systems are non-minimum phase. Non-minimum phase systems are traditionally avoided in control design because they exhibit undesirable properties, such as instability under high gain feedback. There are advantages however in using a non-collocated sensor, as presented in Lee [1]. By comparing the effects of using collocated and non-collocated measurements, Lee concluded a higher bandwidth and lower root mean square response was possible using the non-collocated sensor.

In this thesis a simple technique of blending two sensor measurements, one collocated, the other non-collocated, is employed to control a single actuator. It is anticipated that using a blended measurement will produce desirable properties of both the collocated and non-collocated control systems while maintaining a low order compensator. The performance gained by using a second sensor will be investigated and presented along with its limitations.

An investigation into the use of blended measurements is begun by first examining the open loop pole-zero patterns for several simple configurations. Exact transfer functions are presented for a free-free beam and a cantilevered beam with an applied point load. The exact location of the poles and zeros are determined from the transcendental transfer functions. Using these transfer functions, the blended

measurement's transfer function is determined and the relationship between the blending ratio and the zero locations is investigated. The closed loop response is then related to the open loop zero locations.

To demonstrate and validate the blended technique, three systems will be investigated. The first two are a cantilevered beam with and without an end mass. Analytical finite element method (FEM) models are developed for both cases and are compared to experimental results. Closed loop control is then theoretically determined using MATLAB [2], and is then validated using experimental data. A third theoretical case is investigated using a free-free torsional rod. The torsional rod is analogous to a gimbal system in that it has both rigid body motion and symmetric modes. Comparisons of the three systems will be made and advantages and disadvantages of using blended measurements presented.

II. Background

To investigate the use of a blended measurement, it is first essential to examine the relationship between the actuator and sensor locations. For a single-input single-output (SISO) system, the closed loop performance is easily examined using the classical analysis approach of the root locus method. By examining the position of the roots (system poles) in the complex plane as the system gain is increased, the system response can be determined as a function of the gain. As the system gain is increased the closed loop poles will move toward the open loop system zeros. Systems which have open loop zeros in the right half of the complex plane are termed non-minimum phase (NMP). As the gain of a NMP system is increased, the closed loop poles will eventually move towards the zeros and result in unstable performance once the poles cross into the right half plane.

Numerous techniques have been developed to handle these NMP systems. Rao and Westerheide [3] present a method of modifying an LQR/LTR controller for an experimental grid structure which is modeled as a NMP system. Misra [4] presents a method of using feedthrough compensation, such

that the augmented plant is then minimum phase. Although some success with NMP systems has been demonstrated, they typically result in high order compensators. Essentially these compensators place additional zeros near the plant poles and then add poles to achieve the desired closed loop performance. Each additionally placed zero increases the complexity of the compensator and introduces robustness issues when the modelled poles and actual poles differ significantly.

An alternative method of dealing with the NMP system is that of avoidance; using collocated sensor and actuator pairs. Park and Asada [5] developed a special transmission mechanism for a flexible arm such that the applied torque was collocated with the sensor at the end of the arm. Using this technique, the NMP system typical of robotic links with end point sensors was avoided. The advantage of using collocated measurements is developed in Junkins [6] using symmetric output feedback. It is shown that using this type of feedback, global stability robustness is achieved for all plant variations. However, such a control system may be difficult to implement since it requires a sensor at every actuator which measures inertial position and rate. An additional consideration is where to optimally place a sensor or an actuator to provide the most sensor information or to give the actuator greater control authority.

Placement of sensor actuator combinations is discussed in Lim [7].

The luxury of being able to decide sensor placement may not be realistic, and may be fixed by physical constraints of the system. Consider a gimbal mechanism used to track a target as shown in the figure below. A torque motor is placed on one gimbal axis, and due to physical limitations,

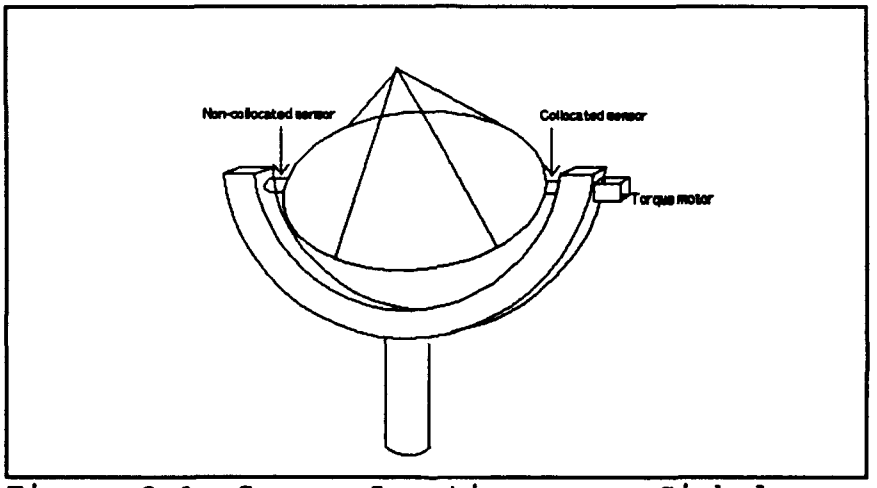


Figure 2.1 Sensor Locations on a Gimbal

the only possible locations of the rotation sensor is either adjacent to the torque motor (collocated) or at the far end of the gimbal (non-collocated). The question this thesis will consider is "Are there advantages of using both sensors to control the system using a blended measurement and if so, what are the tradeoffs?"

To compare the blended method to a control law using a collocated sensor, the placement of the actuator and the sensors will be fixed for both cases. To meet the objective of a low order compensator, the blended method's compensator design will be kept as simple as possible to achieve a stable system. For the cantilevered beam, this corresponds to using proportional rate feedback. For the torsion rod, the minimal compensation is a PD or lead compensator to stabilize the rigid body motion.

Exact Transfer Functions

The effect of the blending ratio on the transfer function zeros is illustrated by first developing the exact transfer function in terms of transcendental functions. The exact poles and zeros will be calculated for the collocated, non-collocated, and blended sensor position for a beam in bending. These values will then be compared to the FEM results to validate the zero locations using an FEM model.

Using Hamilton's principles, the governing equation for a prismatic Beurnoulli-Euler beam with only end loading can be written as [8:210]:

$$EIV^{iv}(x,t) + \sigma\ddot{V}(x,t) = 0$$
$$V^{iv} \triangleq \frac{\partial V^4}{\partial x^4} \quad , \quad \ddot{V} \triangleq \frac{\partial V^2}{\partial t^2} \tag{2.1}$$

V(x,t) represents the transverse displacement, x represents the axial location along the beam, EI represents the bending stiffness and σ the mass density per unit length. The solution is dependant on the boundary conditions imposed on the ends of the beam.

Exact Solution for a Free-Free Beam

As developed in Wie and Bryson [9] for a flexible free-free beam, Eqn 2.1 can be non-dimensionalized with x and V having units of the beam length L, and time in units of $(\sigma L^3/EI)^{\frac{1}{2}}$. Taking the Laplace transform of the governing equation and the boundary conditions yields:

$$\begin{aligned} V^{iv}(x,s) - \lambda^4 V(x,s) &= 0 \\ V^{ii}(0,s) = V^{ii}(1,s) &= 0 \\ V^{iii}(0,s) &= f(s) \\ V^{iii}(1,s) &= 0 \end{aligned} \qquad (2.2)$$

with the Laplace variable defined as:

$$s \triangleq \pm\sqrt{-\lambda^4} \qquad (2.3)$$

For a collocated sensor actuator pair at one end of the beam, the non-dimensionalized transfer function is given as:

$$\frac{V(0,s)}{f(s)} = \frac{\sinh\lambda\cos\lambda - \cosh\lambda\sin\lambda}{\lambda^3(1 - \cos\lambda\cosh\lambda)} \qquad (2.4)$$

As will be shown, this transfer function is characterized in the s domain by an alternating pole-zero pattern along the imaginary axis. In contrast, a separated sensor actuator pair where the actuator is at one end of the beam and the sensor at the other end has the following transfer function:

$$\frac{V(1,s)}{f(s)} = \frac{\sinh\lambda - \sin\lambda}{\lambda^3(1 - \cos\lambda\cosh\lambda)} \qquad (2.5)$$

For the non-collocated case, the zeros all lie on the real axis, symmetric about the imaginary axis. This results in a NMP system due to the zeros in the right half plane. In between the extremes, the s domain characterization contains both real and imaginary axis zeros.

Exact Solution for a Cantilevered Beam with End Excitation

Using the same method as described above, the exact transfer function for the cantilevered beam with the excitation point applied at the tip is found by applying the following boundary conditions to Eqn 2.1.

$$V(0,s) = V^{i}(0,s) = 0$$

$$V^{ii}(1,s) = 0 \qquad V^{iii}(1,s) = f(s)$$

A solution of the form:

$$V(x,s) = C_1 \sin\lambda x + C_2 \cos\lambda x + C_3 \sinh\lambda x + C_4 \cosh\lambda x \quad (2.6)$$

is assumed and the constants are found from application of the boundary conditions. The transfer function for an arbitrary location x along the beam is given by:

$$\frac{V(x,s)}{f(s)} = \frac{(c\lambda + ch\lambda)(sh\lambda x - s\lambda x) + (s\lambda + sh\lambda)(c\lambda x - ch\lambda x)}{2\lambda^3(1 + c\lambda ch\lambda)} \quad (2.7)$$

For the collocated case, where the sensor is located at the tip, the transfer function is given by:

$$\frac{V(1,s)}{f(s)} = \frac{\cos\lambda \sinh\lambda - \cosh\lambda \sin\lambda}{\lambda^3(1 + \cos\lambda \cosh\lambda)} \quad (2.8)$$

The pole-zero patterns corresponding to the transfer functions given in Eqn 2.7 and Eqn 2.8 will be presented in a subsequent section.

Exact Solution for Cantilevered Beam with Arbitrary Excitation Point

To compute the transfer function for an arbitrary input location, it is necessary to break the problem into two portions. This is required since the governing Eqn 2.1 was developed for the case where only end loads were applied. The solution is found by breaking the beam in two sections at the point of excitation and forcing continuity at the break, corresponding to no breaks or kinks in the beam. The two sets of boundary conditions are given as:

$$
\begin{aligned}
V(0,s) &= V^{i}(0,s) = 0 \\
V^{iii}(\delta^{-},s) &+ f(s) = V^{iii}(\delta^{+},s) \\
V^{ii}(\delta^{-},s) &= V^{ii}(\delta^{+},s) \\
V^{i}(\delta^{-},s) &= V^{i}(\delta^{+},s) \\
V(\delta^{-},s) &= V(\delta^{+},s) \\
V^{ii}(1,s) &= V^{iii}(1,s) = 0
\end{aligned}
$$

with δ representing the point of application of the excitation. The problem setup is shown in Figure 2.2.

Again an assumed solution of the form of Eqn 2.6 is used for each of the two portions of the beam. The solution then involves solving for the eight constants in the assumed form of the solution. The problem was setup in matrix form and input to Mathematica [10] to obtain a solution in

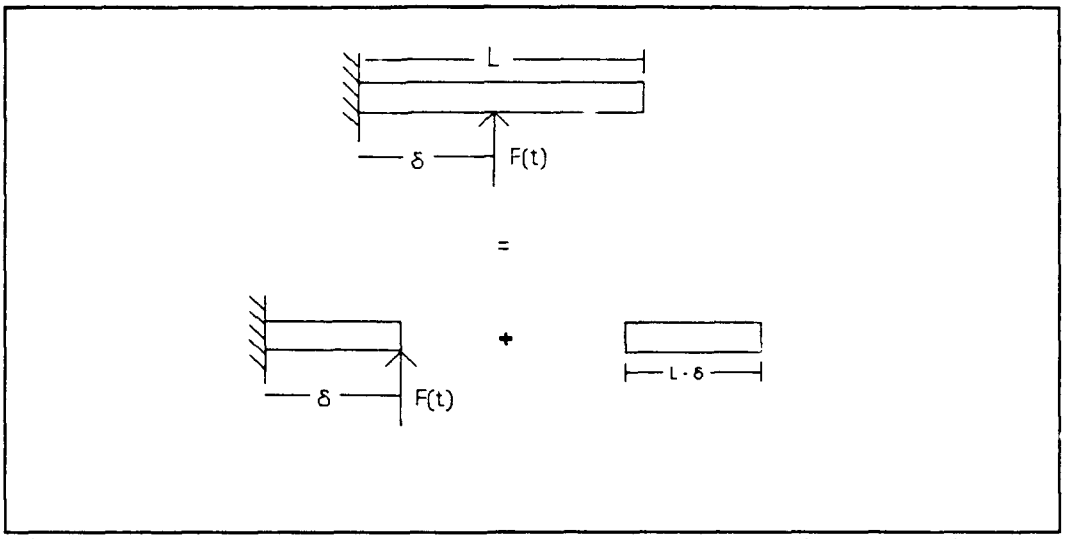


Figure 2.2 Problem Setup for Beam with Arbitrary Excitation Point.

symbolic form. Transfer functions were then computed for the collocated position and the non-collocated position at the end of the beam.

The collocated transfer function is given as:

$$\frac{V(\delta,s)}{f(s)} = \frac{N1 + N2 + N3 + N4}{4\lambda^3(1 + c\lambda ch\lambda)}$$

$$N1 \triangleq ch\lambda s\lambda + ch\lambda(1-2\delta)s\lambda$$

$$N2 \triangleq 2ch\lambda\delta s\lambda\delta - 2ch\lambda(1-\delta)s\lambda(1-\delta) \qquad (2.9)$$

$$N3 \triangleq -c\lambda sh\lambda - c\lambda(1-2\delta)sh\lambda$$

$$N4 \triangleq -2c\lambda\delta sh\lambda\delta + 2c\lambda(1-\delta)sh\lambda(1-\delta)$$

$$c \triangleq \cos(), \quad s \triangleq \sin(), \quad ch \triangleq \cosh(), \quad sh \triangleq \sinh()$$

whereas the non-collocated transfer function is given as:

$$\frac{V(1,s)}{f(s)} = \frac{N1 + N2}{2\lambda^3(1 + c\lambda ch\lambda)}$$

$$N1 \triangleq ch\lambda\delta s\lambda - s\lambda(1-\delta) + ch\lambda s\lambda\delta \qquad (2.10)$$

$$N2 \triangleq -c\lambda\delta sh\lambda + sh\lambda(1-\delta) - c\lambda sh\lambda\delta$$

Both transfer functions are dependent on the excitation position δ. Note that Eqn 2.9 reduces to Eqn 2.8 for $\delta = 1$, as expected, for the sensor and excitation point at the tip of the beam. A second crosscheck between transfer functions can be demonstrated using the theory of reciprocity [11:311], where interchanging the input and output results in the same transfer function. Thus, Eqn 2.7 is equivalent to Eqn 2.10 when the sensor location in Eqn 2.7 is matched to the input location in Eqn 2.10 (i.e. $\delta = x$). The reciprocity theorem is exploited in experimental modal analysis where data can be equivalently taken using either a fixed excitation and roving sensor measurement or vice-versa. The most convenient method is chosen to extract the data of interest. It should also be noted that as expected, the transfer functions of the cantilevered beam all have equivalent denominator roots. This is because the denominator represents the natural frequencies of the structure (system poles) and is independent of both the excitation location and the sensor position.

Exact Pole-Zero Patterns

Using the above transfer functions, the exact locations of the poles and zeros are found by solution of the roots of the denominators and numerators respectively. Poles and

zeros on the imaginary axis equate to purely real roots of the transcendental equations, whereas real axis roots are complex solutions of the form a+ai, with equal magnitude real and imaginary components, as seen by examination of Eqn 2.3. This special form where the magnitude of the real and imaginary parts were equal (to produce real axis roots) was used to compute the real axis zeros. This avoids a multi-parameter search for zeros of the transfer function with an arbitrary complex root of a+bi.

Martin [12] has shown that for undamped flexible bodies where the sensor and actuator are collocated, the resulting transfer function will have alternating poles and zeros on the imaginary axis. Transfer functions for non-collocated sensors will have both real and imaginary axis zeros. Furthermore, when reduced order models of the transfer functions are used, as in FEM models, the truncation method will effect the zero locations [9]. Using MATLAB and both the FZERO and FMIN algorithms, the exact poles and zeros were computed and are listed in Table 2.1. Results of the ten element FEM models using MATLAB's TZERO and EIG commands are listed for comparison to the exact solutions. Development of the FEM model along with the state-space formulation is presented in Chapter III.

Table 2.1. Pole-Zero Locations for a Beam in Bending.

Free-free beam

Exact poles	zeros coll	zeros non-coll	FEM poles	zeros coll	zeros non-coll
±22.37i	±15.42i	±30.84	±22.37i	±15.42i	±30.83
±61.67i	±49.96i	±99.93	±61.69i	±49.97i	±99.86
±120.9i	±104.2i		±121.0i	±104.3i	

Cantilevered beam with end excitation (non-coll -> x=.5L)

Exact poles	zeros coll	zeros non-coll	FEM poles	zeros coll	zeros non-coll
±3.516i	±15.42i	±21.76	±3.516i	±15.46i	±21.80
±22.03i	±49.96i	±62.57i	±22.04i	±50.50i	±62.56i
±61.70i	±104.2i	±177.7	±61.71i	±106.8i	±177.2

Cantilevered beam with excitation at .4L (non-coll -> x=L)

Exact poles	zeros coll	zeros non-coll	FEM poles	zeros coll	zeros non-coll
±3.516i	±7.541i	±17.34	±3.516i	±7.541i	±17.34
±22.03i	±50.53i	±97.11i	±20.04i	±50.54i	±97.17i
±61.70i	±112.5i		±61.71i	±112.6i	

For all three cases, the alternating imaginary axis pole-zero pattern is exhibited for the collocated sensor. The non-collocated cases have a combination of real and imaginary axis zeros. Figure 2.3 illustrates the exact pole-zero locations for the cantilevered beam with end point excitation and collocated sensor. In contrast, Figure 2.4 shows the exact pole-zero locations when the sensor is located at the midpoint of the beam.

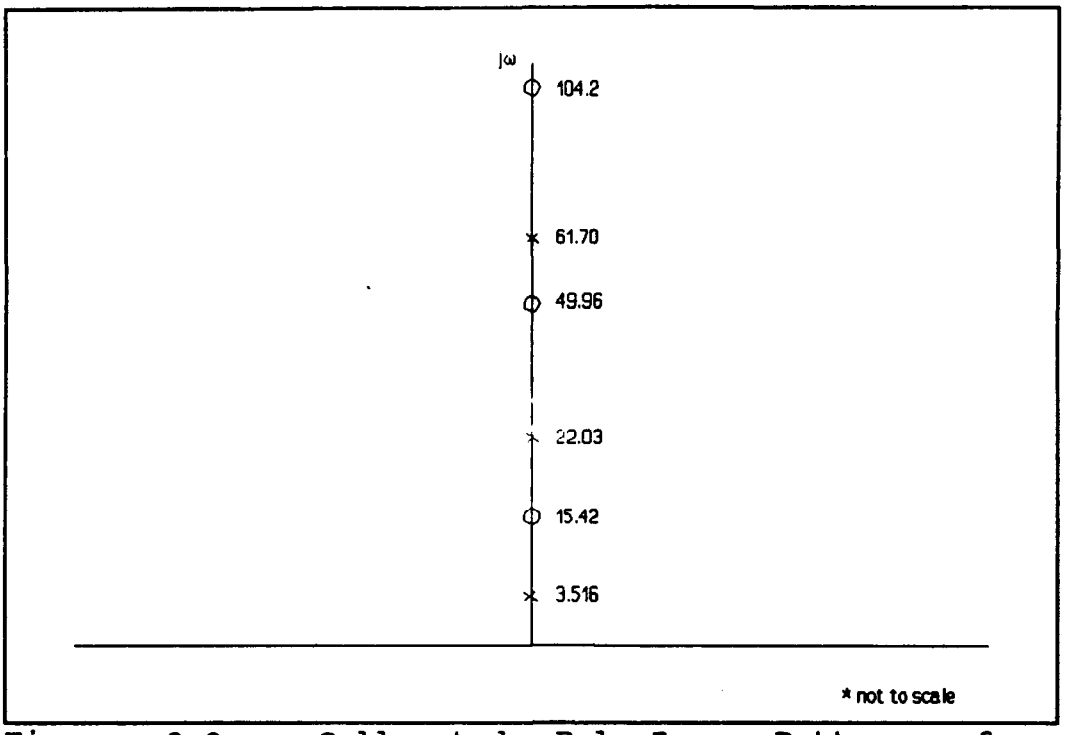


Figure 2.3 Collocated Pole-Zero Pattern of a Cantilevered Beam with End Excitation.

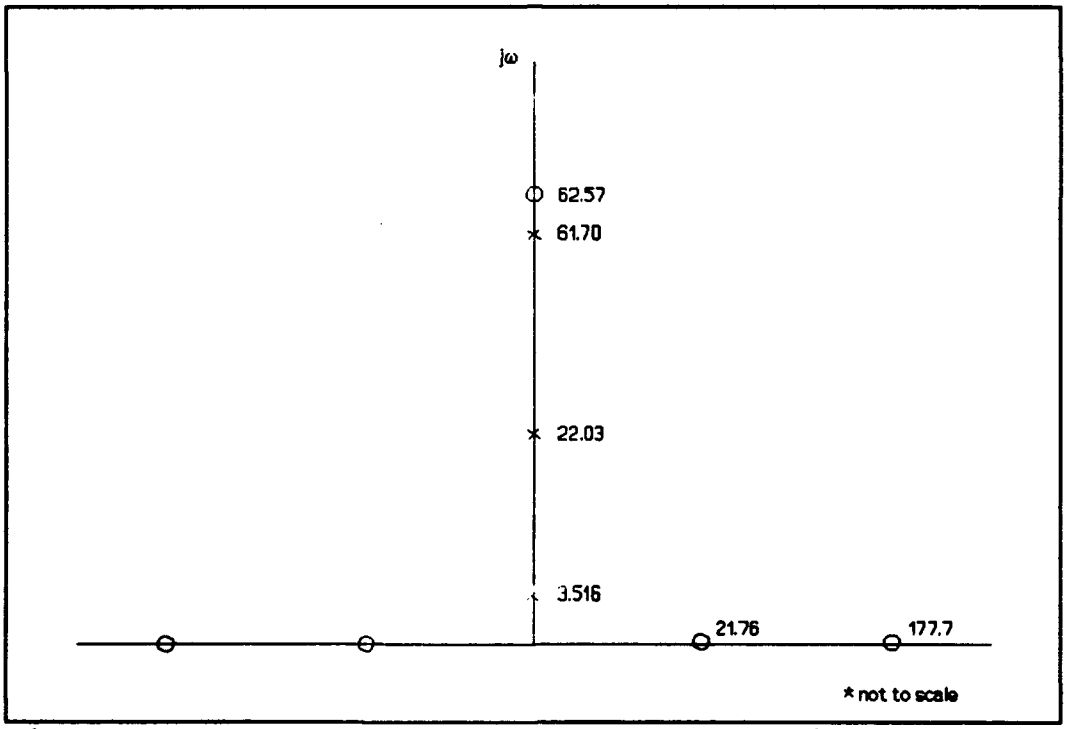


Figure 2.4 Pole-Zero Pattern for a Cantilevered Beam with Endpoint Excitation and the Sensor at the Midpoint.

Performance Characteristics of Collocated and Non-Collocated Systems

Using standard closed-loop performance criteria, the difference between the two systems can be summarized as follows, based on previous work by Lee [1]. The collocated system is very robust to gain variations and has a faster settling time, whereas the non-collocated system has a higher achievable bandwidth and a lower root mean square (RMS) response. Thus the impetus for using blended measurements is to achieve the positive aspects of both systems.

The primary advantage of using a collocated sensor, and hence a minimum phase system, can be seen by comparing the closed loop root loci. For the cantilevered beam with end point excitation, the closed loop root locus using collocated rate feedback is shown in Figure 2.5. For this minimum phase system, the closed loop roots all remain in the left half plane (LHP) for all negative values of the feedback gain. In contrast, the non-collocated closed loop root locus shown in Figure 2.6 shows the consequence of having right half plane (RHP) zeros. This system is unstable for all values of the feedback gain. A higher order compensator is required to stabilize this NMP system.

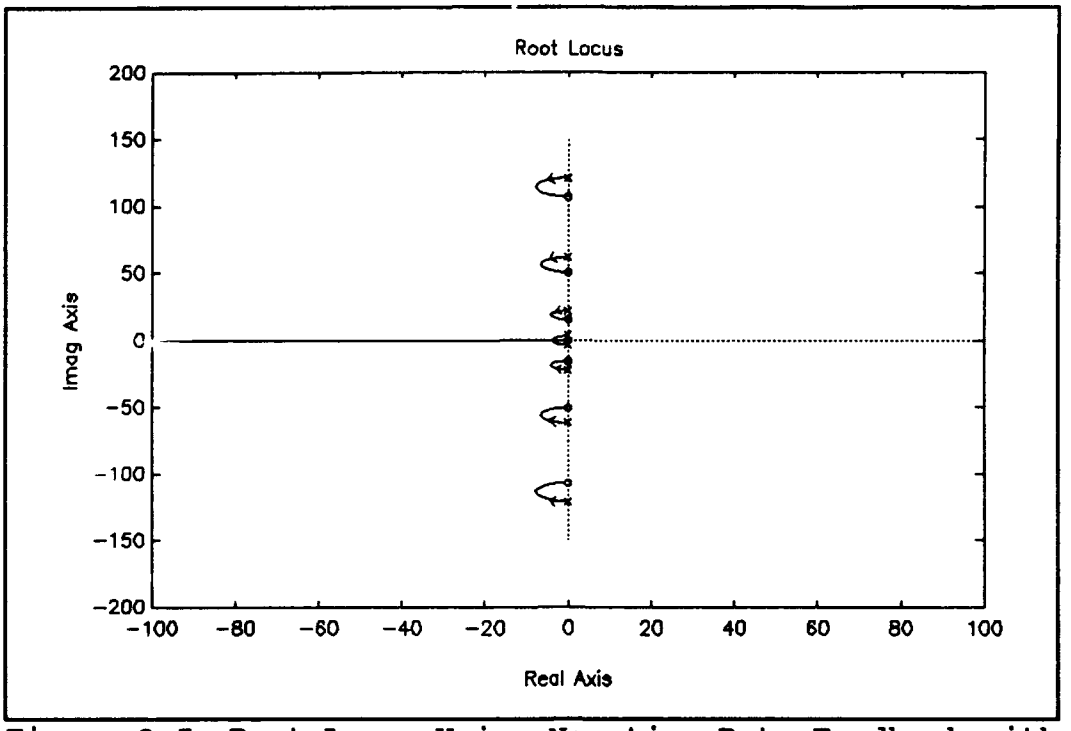


Figure 2.5 Root Locus Using Negative Rate Feedback with a Collocated Sensor on a Cantilevered Beam.

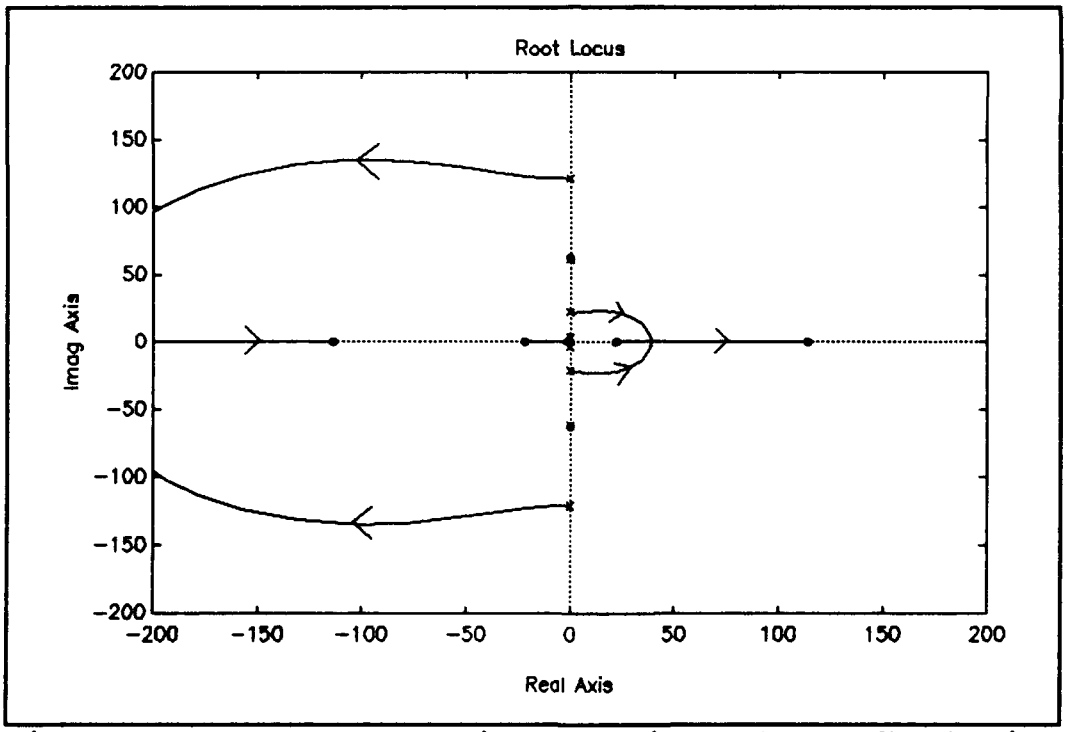


Figure 2.6 Root Locus Using Negative Rate Feedback with a Non-Collocated Sensor on a Cantilevered Beam.

Blending Method

Based on pole-zero patterns, there is a transition between the all imaginary zeros of the collocated case to the real zeros of the non-collocated system. By examining the open loop pole-zero patterns of a blended measurement, some of the system's closed loop behavior can be determined and utilized to select a value for the blending ratio. The transfer function for the blended sensor is written as:

$$\frac{V_{blend}}{f(s)} = \frac{(1 - \alpha) V_{co} + \alpha V_{nc}}{f(s)} \qquad (2.11)$$

where α is defined as the blending ratio and $V_{co}/f(s)$ and $V_{nc}/f(s)$ represent the collocated and non-collocated transfer functions previously defined. Using output feedback, the control force is then written as:

$$u = -K * [1-\alpha \;\; \alpha] * \begin{bmatrix} y_{co} \\ y_{nc} \end{bmatrix} \qquad (2.12)$$

$$0 \leq \alpha \leq 1$$

with y_{co} and y_{nc} representing the collocated and non-collocated measurements respectively. The value K represents the compensator which can either be a single gain

constant or a higher order dynamic compensator acting on the single blended measurement.

For a fixed actuator location and pair of sensors, the open loop pole-zero pattern is plotted as a function of α using Eqn 2.11. As the blending ratio is increased, greater weighting is placed on the non-collocated measurement and less on the collocated. On the pole-zero plot, the changing blending ratio corresponds to the zeros moving along the imaginary axis and eventually onto the real axis. While movement of the zeros is along the imaginary axis, the system remains minimum phase. Once the zeros coalesce and split toward the real axes, the system is NMP. Thus the system can be varied from minimum phase to non-minimum phase by simply varying the blending ratio.

For the three cases considered above, the point at which the system transitioned to NMP (occurrence of real axis zeros) was computed using the FEM model and MATLAB's TZERO algorithm. For the free-free beam, the transition point was approximately $\alpha = 0.58$, while for the cantilevered beam with end excitation, the transition point was approximately at $\alpha = 0.68$. The cantilevered beam with excitation at $x = 0.4L$ had real axis zeros for values of α greater than 0.4. Verification of the FEM results were computed for several values of the blending ratio using the exact solutions for the first two cases and Eqn 2.11. The

zero locations as a function of the blending ratio are shown in Figure 2.7 for the cantilevered beam with end excitation, and in Figure 2.8 for the free-free beam. The patterns of the zero movements are repeated up and down the imaginary axis for higher order models.

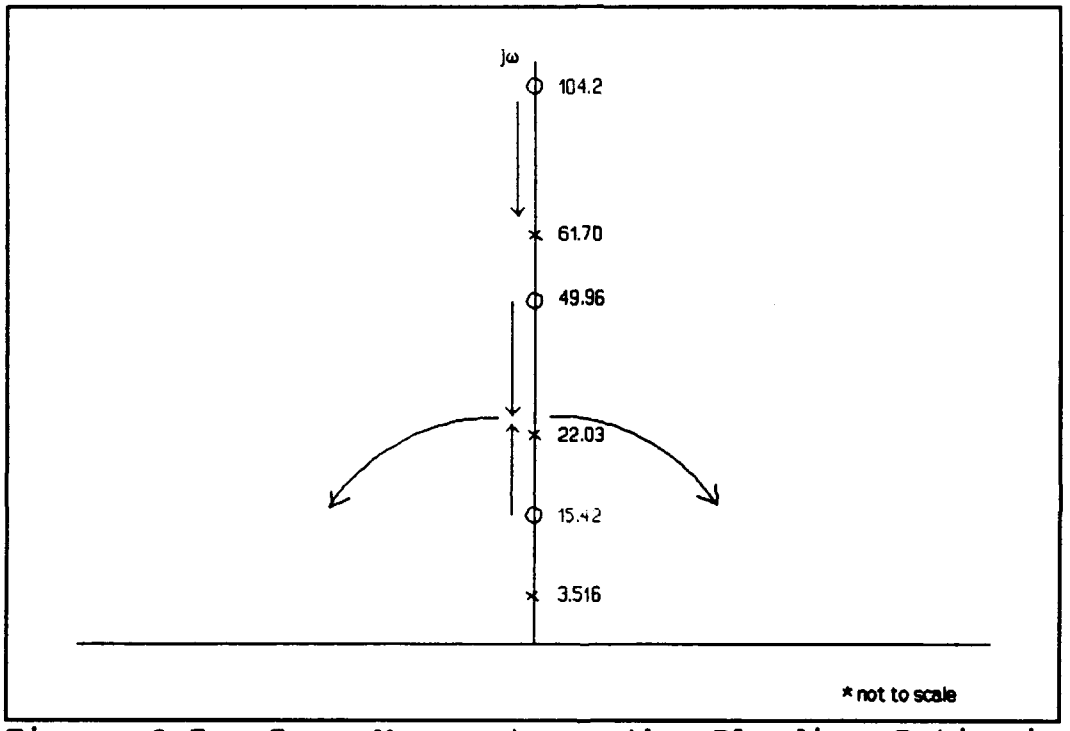


Figure 2.7 Zero Movement as the Blending Ratio is Increased for the Cantilevered Beam with End Excitation.

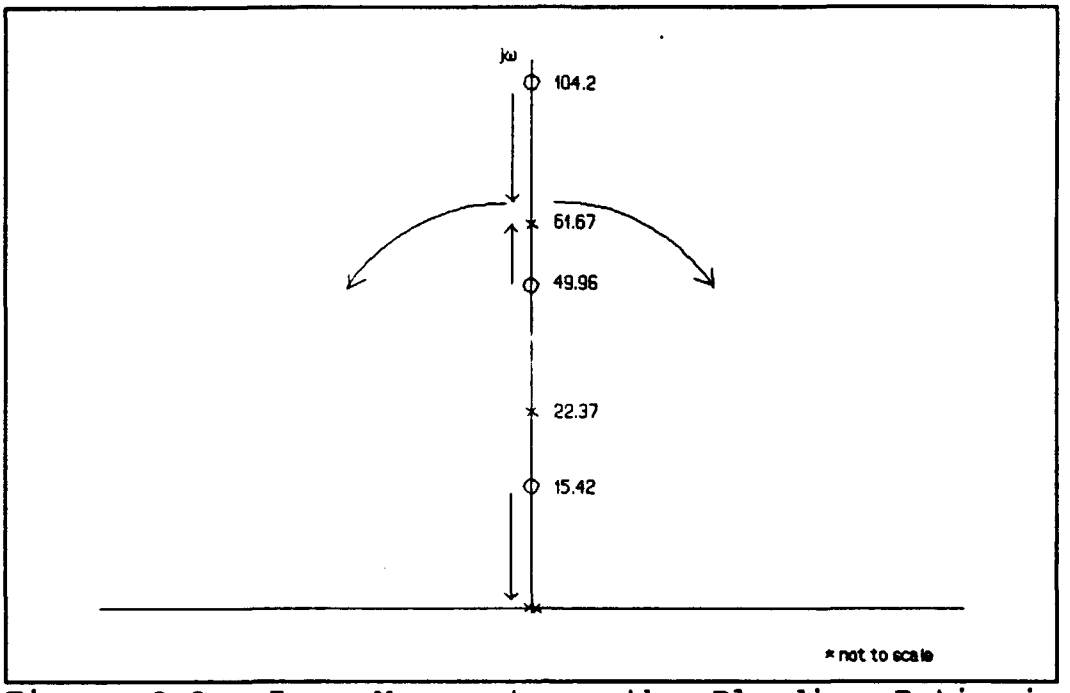


Figure 2.8 Zero Movement as the Blending Ratio is Increased for the Free-Free Beam.

For a beam in bending, the pole-zeros patterns for both a collocated and a non-collocated sensor location were presented. Comparisons were made between the exact pole-zeros using transcendental transfer functions and those obtained using the FEM models. The FEM models and MATLAB accurately computed the pole-zero locations for the three cases considered. It was then shown that by blending collocated and non-collocated measurements, the transfer function will remain minimum phase for some range of the blending ratio. In Chapter IV, the advantages and the limitations of using a blended measurement to control a flexible beam will be presented.

III. Characterization of Experimental Equipment

The AFIT Cantilevered Beam (ACB) was originally developed by WRDC/FIBG, to demonstrate active control of a cantilevered beam in two orthogonal bending axes and torsion. In this configuration, the ACB was used as an analog to a large flexible space structure in which only inertial sensors and actuators are used. The original configuration had problems associated with the proof mass actuators (limited force at low frequencies) and a low frequency drift in the measurement channels. AFIT chose to resurrect the ACB and use it as test article for candidate control algorithms. Modifications to the original setup and experimental results for closed loop control are included in Jacques [13]. In its present configuration, the ACB is no longer analogous to a flexible space structure due to the use of a ground based actuator.

The ACB consists of a 70 inch inverted cantilevered beam with end mass. Three piezo-resistive accelerometers are available for acceleration measurements. A structural dynamics shaker is used which can function as either the disturbance input or the control actuator. Alternative excitation is achieved through the use of an impact hammer

with a force transducer. Digital control is facilitated through the use of Systolic Array Systems' PC-1000 programmable controller [14]. Frequency response data is obtained using a Tektronix 2642A spectrum analyzer [15]. Modal information is extracted from the frequency spectra data using the STAR Modal software package [16]. A representative configuration is shown in Figure 3.1.

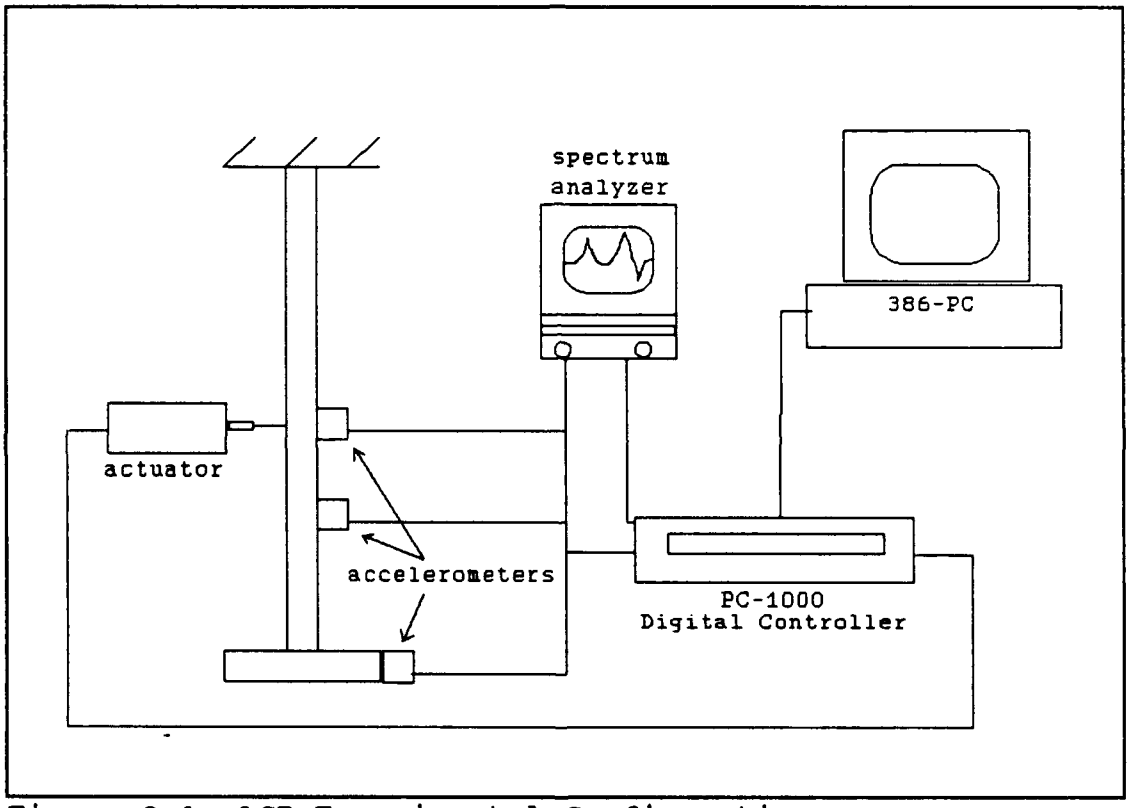


Figure 3.1 ACB Experimental Configuration.

Structure

The ACB is a 70" inverted cantilevered aluminum beam with end mass. The beam is attached to an aluminum frame structure. Originally, the end plate allowed for mounting of linear proof mass actuators to control beam rotations. Subsequent experiments with the ACB did not include the plate because only control of bending modes were under investigation. As will be shown in Chapter IV, the ACB's mode shapes are significantly different with and without the end mass. With the end plate installed the beam behaves as a fixed-pinned beam rather than a fixed-free beam. This allowed two separate examinations of the blending method on the ACB, one with the end mass installed, and a second with the mass removed. The physical characteristics of the beam are listed in Table 3.1.

Table 3.1 ACB Physical Properties

Property Description	Value	Units
Beam Length (L)	5.896	ft
Y Cross-Section Width	1.03	in
Z Cross-Section Width	0.754	in
Cross section Area (A)	5.393×10^{-3}	ft^2
Young's Modulus (E)	1.555×10^{9}	lbf/ft^2
Beam Density (ρ)	5.373	$slug/ft^3$
Beam Mass	0.1708	slug
Z Moment of Inertia (I_z)	3.311×10^{-6}	ft^4
Plate Diameter	1.0	ft
Plate Thickness	1.0	in
Plate Mass	0.3416	slug
Plate Y-Z Moment of Inertia	2.155×10^{-2}	slug ft^2

Analytical Model Development

Although the ACB has been used for several research efforts, a good analytical model did not exist for the beam in its current configuration. The two degree of freedom

model used by McCall [17] did not include the endplate mass, nor did the model compare well with experimentally obtained results. The model developed by Jacques [13] based on experimentally measuring modal frequencies and displacements agreed well with the experimental data, as it should; however, it had the additional mass of the linear actuators on the end plate which are no longer present. Furthermore, the sensors were not all placed in the same position (because torsional rotations were also measured), and thus the transfer function zeros do not correspond to the current setup. It was desirable to have an analytical model in state space form for theoretical analysis which could be easily altered to accommodate different sensor/actuator locations and/or beam configurations. To provide the greatest flexibility, it was decided to assemble an FEM using MATLAB, since this was the environment all the theoretical work would be done in.

As was done in previous FEMs for this beam, it was modeled as a ten element beam with lumped masses representing the endplate and the sensor and actuator attachments. Each element is represented as a Bernoulli-Euler beam with two degrees of freedom at each node as shown in Figure 3.2.

For each element, shape functions are matched to the boundary conditions assuming the element is in static

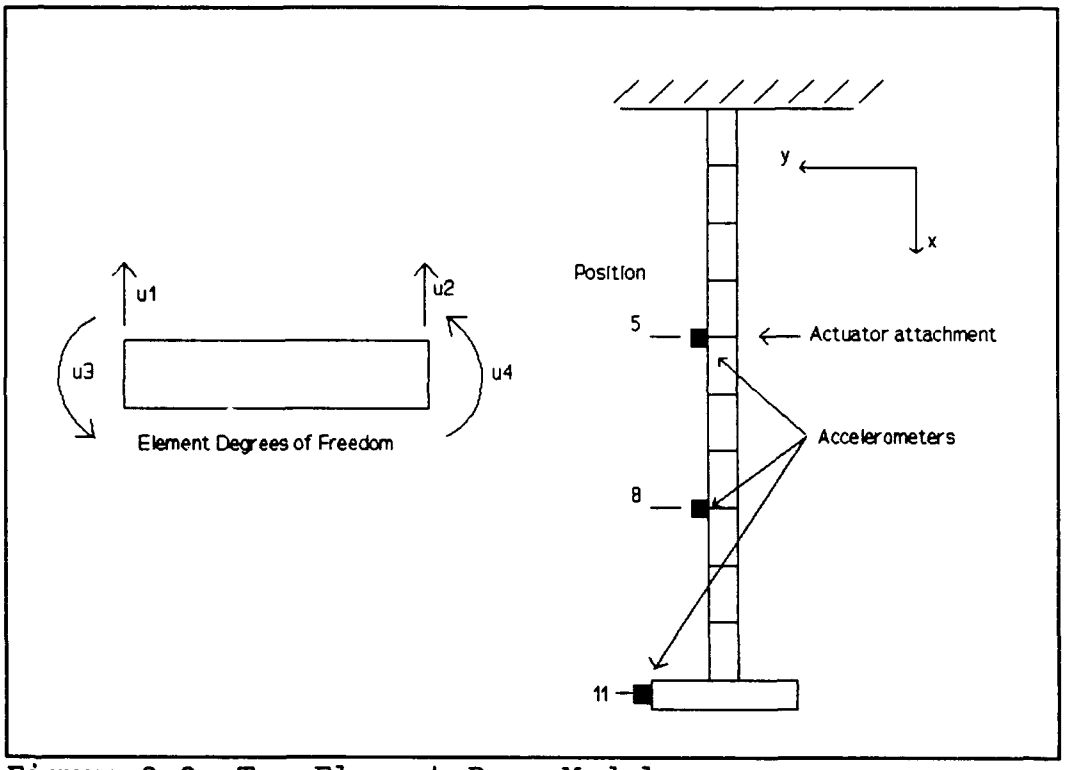


Figure 3.2 Ten Element Beam Model.

equilibrium and has only end loads applied. As developed in Craig [8:387], each element has the following corresponding mass and stiffness matrix:

$$M_{ij} = \frac{\rho AL}{420}\begin{bmatrix} 156 & 22L & 54 & -13L \\ 22L & 4L^2 & 13L & -3L^2 \\ 54 & 13L & 156 & -22L \\ -13L & -3L^2 & -22L & 4L^2 \end{bmatrix} \tag{3.1}$$

$$K_{ij} = \frac{EI}{L^3}\begin{bmatrix} 12 & 6L & -12 & 6L \\ 6L & 4L^2 & -6L & 2L^2 \\ -12 & -6L & 12L & -6L \\ 6L & 2L^2 & -6L & 4L^2 \end{bmatrix} \tag{3.2}$$

The global mass and stiffness matrices are then formed

by assembling the elemental matrices along the main diagonal of the global matrices. The lumped masses are then added to the appropriate diagonal entries of the global mass matrix, as are the rotary inertia terms. The cantilevered end constraint is imposed by simply removing the first two rows and columns of the global matrices indicating no displacements or rotations of the first node. Using the global matrices, the governing equations are:

$$M\ddot{x} + Kx = F \tag{3.3}$$

where $\underline{F}$ has only a single non-zero entry corresponding to the actuator location. The velocity measurements (integrated accelerations) are written as:

$$y = \hat{C}\dot{x} \tag{3.4}$$

where $\hat{C}$ has non-zero entries at nodes where the sensors are located. The transformation to state space is then computed by first forming the transformation:

$$\Phi\eta = x \tag{3.5}$$

where Φ is the modal matrix formed from the eigenvectors of the global mass and stiffness matrices. Forming the transformation and multiplying through by Φ^{-1} to diagonalize the mass and stiffness matrices results in:

$$\Phi^{-1}M\Phi\ddot{\eta} + \Phi^{-1}K\Phi\eta = \Phi^{-1}F \tag{3.6}$$

Multiplying through by the inverse of the diagonalized mass

matrix yields:

$$\ddot{\eta} + [\Phi^{-1}M^{-1}K\Phi]\eta = [M\Phi]^{-1}F \tag{3.7}$$

which can be written as:

$$\ddot{\eta} + \omega_n^2\eta = [M\Phi]^{-1}F \tag{3.8}$$

where ω_n is a diagonal matrix with the natural frequencies of the structure as the diagonal entries. Although no attempt was made to analytically predict the modal damping value, if viscous damping in the structure is assumed, it can be introduced into Eqn 3.8 as:

$$\ddot{\eta} + 2\zeta\omega_n\dot{\eta} + \omega_n^2\eta = [M\Phi]^{-1}F \tag{3.9}$$

where ζ is determined from experimental open loop data for each mode.

The second order system is then easily converted to first order using Eqn 3.9 with the following results:

$$\dot{\xi} = \begin{bmatrix} 0 & I \\ -\omega_n^2 & -2\zeta\omega_n \end{bmatrix}\xi + \begin{bmatrix} 0 \\ [M\Phi]^{-1}F \end{bmatrix} \tag{3.10}$$

$$\xi \triangleq \begin{bmatrix} \eta \\ \dot{\eta} \end{bmatrix}$$

which is now in the required state-space form. The measurements in terms of the new state variable ξ is:

$$Y = [0, \hat{C}\Phi]\xi \tag{3.11}$$

The resulting A, B and C matrices are then given by:

$$A = \begin{bmatrix} 0 & I \\ -\omega_n^2 & -2\zeta\omega_n \end{bmatrix} \tag{3.12}$$

$$B = \begin{bmatrix} 0 \\ [M\Phi]^{-1}E \end{bmatrix}$$

$$C = [0, \hat{C}\Phi]$$

In this form, the A matrix for the ten element beam is a 40x40 matrix. For implementation on a digital controller and ease of comparison, the model was truncated to reduce this matrix to an 8x8 by retaining only the first four bending modes. Note that there is no feedforward term and hence the D matrix is a matrix of zeros of the appropriate size.

Using the above method, a script file in MATLAB was written to produce the required A, B and C matrices and is given in Appendix C. This script file was used to model the ACB as well as the free-free and cantilevered beams in non-dimensionalized form used in the previous chapter.

Finite Element Method Model Validation

Comparing the analytical results to those experimentally obtained, the difference was greater than ten percent. To validate the FEM code, the exact solution to a cantilevered beam was compared to the results of the FEM. For a

cantilevered beam, the characteristic equation resulting from the solution of the eigenvalue problem of Eqn 2.1 (developed in Chapter II) is given by:

$$\cosh(\lambda L)\cos(\lambda L)+1=0 \tag{3.13}$$

The natural frequencies (in Hertz) of the beam are then found for each eigenvalue and are given by:

$$f_n=\frac{(\lambda L)^2}{2\pi L^2}\times[\frac{EI}{\sigma}]^{1/2} \tag{3.14}$$

Eqn 3.13 is solved iteratively for the values of λL. Comparing the results from the FEM to the exact solution given above, the FEM model had less than one percent error for the first three modes, and thus the FEM code was considered valid.

Table 3.2 Comparison of FEM to Analytical

mode #	Analytical (Hz)	FEM (Hz)	error (%)
1	6.6545	6.6536	.01
2	41.703	41.664	.09
3	116.77	116.53	.21

In Cristler [18], reference was made that a better match of the FEM results to experimental data was attempted by modelling the entire beam and supporting frame with a FEM model. A closer match was not achieved. Previous work by Yang [19] modeled the ACB and obtained a better match to experimental values by modeling the cantilevered constraint as a combination of a linear and torsional spring. An

iteration was then performed on the values of the spring constants to match the data. Although this method was tested, it was found that better results were obtained by simply iterating on the beam stiffness and end plate mass to match the experimental data. Note that although it would have been satisfying to have the analytical model match experimental data without iterating on the beam physical properties, the important result was to obtain a math model which accurately matches experimental results for simulations. Once the iteration was performed, this result was achieved. The easily checked physical beam properties such as length and cross sectional area of the beam were verified; however, no attempt was made to check the values of the beam density and elastic modulus. An approximate ten percent variation from the values listed in Table 2.1 for the modulus and the mass of the end plate was required to match the experimental data. The resulting state-space A, B and C matrices used for analysis are contained in Appendix B.

Actuator

Both excitation of the structure and control actuation were achieved using an Acoustic Power Systems (APS) Model 113-LA structure dynamics shaker driven by an APS Model 114

amplifier [20]. The shaker is linear over its operating range (0 - 200 Hz) and no compensation was required to account for the shaker dynamics. A frequency response test was performed to ensure that using a single gain constant as the transfer function over the operating range was valid. Two modes of operation are possible: either current or voltage and an optional rubber band suspension system to counter gravity forces. By comparing the frequency response for the two modes of operation, it was decided to operate the shaker in the current mode because it exhibited a very flat response in the frequency range of interest. In the voltage mode, there was a large force spike at the low frequency end of the bandwidth which was close to the fundamental mode of the beam. For all tests, the optional suspension was removed. The mass of the shaker's armature was included in the analytical model of the structure.

During closed loop control tests, the actuator was used to provide both the random disturbance and the control force. This was achieved by adding the disturbance (bandwidth limited random noise) and the control signal in the digital controller. This method of using an actuator to simultaneously provide both the excitation and the control was used successfully in previous vibration experiments [21]. Verification of the method was performed by comparing results to those obtained using impact hammer excitation.

Compared results agreed within the uncertainty in the test equipment.

Controller

For control implementation, a Systolic Array Systems' PC-1000 programmable digital controller was used. The PC-1000 was operated through a PC compatible 386 host computer. The PC-1000 is capable of handling 16 analog input and output signals and is equipped with an 8086 based array processor for processing sensor signals. There are 16 internal states available for estimation and control. The sampling frequency is user selectable with a maximum sampling rate of 2000 Hz. The PC-1000 uses 12 bit A/D converters with user selectable ranges of +/-2.5, 5, and 10 Volts. To accommodate calibration constants, the controller has programmable amplification/attenuation constants for each of the measurement channels. Control algorithms are accomplished on the controller by programming in the state transition matrix as illustrated in Eqn 3.15.

$$\begin{bmatrix} U_{k+1} \\ X_{k+1} \end{bmatrix} = \begin{bmatrix} F_{11} & F_{12} \\ F_{21} & F_{22} \end{bmatrix} \begin{bmatrix} Y_k \\ X_k \end{bmatrix} \qquad (3.15)$$

Measurements

Inertial acceleration measurements are achieved through the use of the Endevco model 2262 piezo-resistive accelerometers. The advantage of this type of accelerometer is its ability to read down to DC levels. This allows for simple calibration procedure of simply taking the difference in the output voltage in the upright and inverted position and dividing by twice the local acceleration of gravity. This calibration constant is then assumed constant (experimentally verified) throughout its range of operation (0-650 Hz). However, because of the ability to read DC, care must be taken to ensure the acceleration measurements are zeroed prior to testing. Accelerometer calibration data is contained in Appendix A.

The demonstrated control system used in this thesis is based on using a blending of velocity measurements. It is possible to use linear velocity transducers (LVTs) to measure velocity directly; however, the LVTs require establishing a ground reference. A second disadvantage of using the LVTs is that the beam deflections are not purely linear and the use of the LVTs would limit the allowable beam deflections. It was therefore decided to use only acceleration measurements. To obtain velocity measurements using the accelerometers, it is necessary to integrate the

acceleration measurements. Although analog integration circuits were available from previous research efforts on the ACB, it was decided to take advantage of the state space controller and perform the integration digitally.

Ideally, an integration circuit would provide a -20 dB/decade attenuation and a -90 degree phase shift. However, when the possibility of non-zero DC levels is considered, the high gain of an ideal integrator at low frequencies presents a problem. This quickly causes the integrator to 'wind up' and saturate the controller input. To avoid this, an integrator suitable for the ACB would provide ideal integration within the control bandwidth, combined with attenuation at very low frequencies. To achieve the low frequency attenuation requires a zero be placed in this frequency range.

Combining the above constraints to achieve the desired integration and low frequency attenuation results in an integrator transfer function of the following form:

$$G(s) = \frac{K(s + z)}{s^2 + 2\zeta ps + p^2} \qquad (3.16)$$

where the pole p is chosen at approximately one decade before the first mode to preserve phase information and the zero z is chosen at a decade below this for the same reason. The damping ratio ζ is picked to avoid a resonant peak, at

the break frequency of the second order pole. The gain K is then set to provide the desired overall gain level. Once the transfer function values where chosen, the discrete finite difference equations were computed. For the ACB (without end mass) an appropriate transfer function is given by:

$$G(s) = \frac{2\ (s + .01)}{s^2 + 2\pi s + (2\pi)^2} \qquad (3.17)$$

with resulting discrete state-space equations for a 2000 Hz sample rate of:

$$A = \begin{bmatrix} .9969 & -.0197 \\ .0005 & 1 \end{bmatrix}$$

$$B = \begin{bmatrix} .4992 \\ .0001 \end{bmatrix} x10^{-3} \qquad (3.18)$$

$$C = [2\ \ .02] \qquad D = 0$$

The discrete equations were then programmed into the PC-1000 and the transfer function of the digital integrator was measured using the spectrum analyzer and compared to the discrete Bode plot generated using MATLAB. Comparing the two, there was an exact agreement in the magnitude plot whereas the phase plots deviated at higher frequencies as shown in Figure 3.3. The additional phase delay in the PC-1000 integration was traced to an additional two sample period delay in the controllers throughput. This was

verified by passing a pulse through the controller and comparing the time domain signals before and after the controller.

The pure two count time delay of the controller can be represented in the Laplace domain as:

$$t\text{-}2T \leftrightarrow e^{-2Ts} \qquad (3.19)$$

where T is the sample period and s is the Laplace variable. Using Euler's formula and letting s = jω results in:

$$e^{-2Tj\omega} = \cos(2T\omega) - j\sin(2T\omega) \qquad (3.20)$$

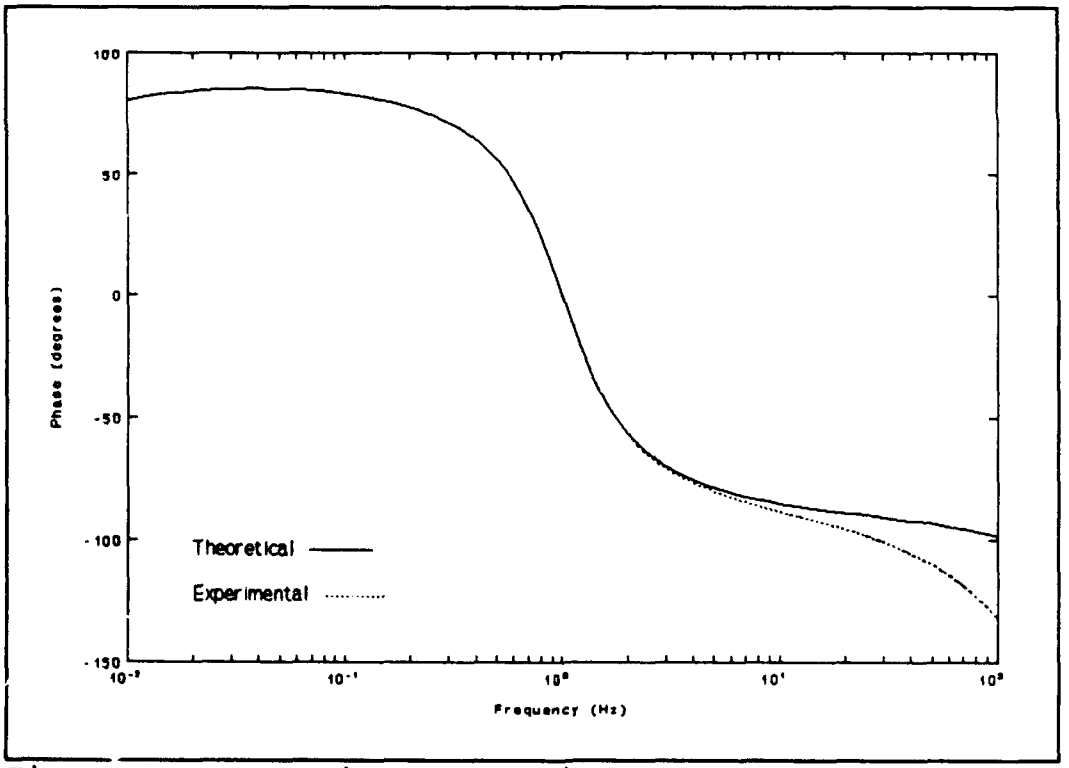


Figure 3.3 Comparison of Predicted and Measured Transfer Functions for the Digital Integrator.

which has unity magnitude for all ω and a phase of $-2\omega T$ radians. Adding this additional phase lag into the predicted plot matched the controller integration plot. The ramifications of this unexpected two count delay is that there is a large phase lag at higher frequencies (72 degrees at 200 Hz) which will de-stabilize the high frequency modes if not adequately attenuated.

Closed Loop Verification

To verify the overall setup, prior to testing the blended measurements, a collocated proportional rate feedback test was performed. A block diagram of the setup is shown in Figure 3.4. The matrix K in the diagram for this test was set to provide gain on only the collocated sensor measurement. It was expected that the test would produce closed loop damping values which agree well with predicted results and in particular demonstrate the robust stability of the collocated measurement. However, this was not the case. Upon closing the loop, high frequency audible resonances occurred and input saturation of the controllers A/D converter was observed. This same behavior was documented in McCall [17] where it was attributed to cascading the multiple order integrators before the controller input. For this test, however, only a single

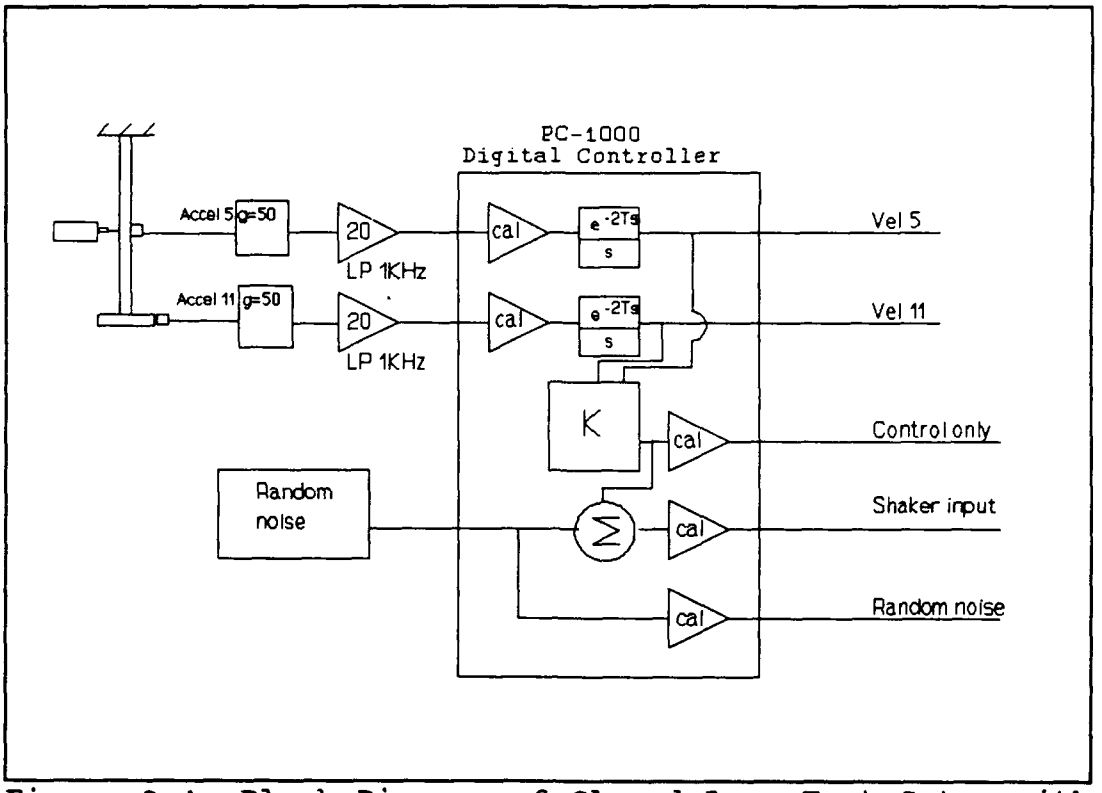


Figure 3.4 Block Diagram of Closed Loop Test Setup with Digital Integration.

digital integrator was being used.

After significant troubleshooting, the closed loop digital integration process can be summarized as follows. Accelerometer signals need to be amplified to acceptable levels for proper A/D conversion at the controller. For a 2 Hz acceleration signal, corresponding to the first mode, a pre-gain of 20 was required for proper A/D conversion at the PC-1000 input operated in the +/- 2.5V range. The controller's output noise level, although small, is enough to excite measurable high frequency modes of the beam. The high frequency beam vibrations are measured by the

accelerometers, amplified and fed back to the actuator. In the process, the large phase lag at these higher frequencies imposed by the digital controller further excited these unstable modes. The higher frequency signals quickly saturate the controller's input and a resulting limit cycle is established. In theory, placing low pass filters between the accelerometers and the controller would remedy the problem. However, lowering the cutoff frequency of the low pass filters in the amplification channel resulted in an increase in the overall phase lag and caused instability at even lower frequencies. Several filter combinations were tried, using Butterworth filters both at the input and output of the controller, but none remedied the problem. The end result is that in theory the digital integration would work if ideal filter components could be used that had zero phase lag.

An approximate evaluation of this unstable behavior was performed by using root locus techniques and a Pade' approximate [22:208] where the pure time delay is approximated as:

$$e^{-2Ts} \approx \frac{1-Ts}{1+Ts} \qquad (3.21)$$

which is based on expanding the left hand side of the above equation in a series expansion and matching the first three

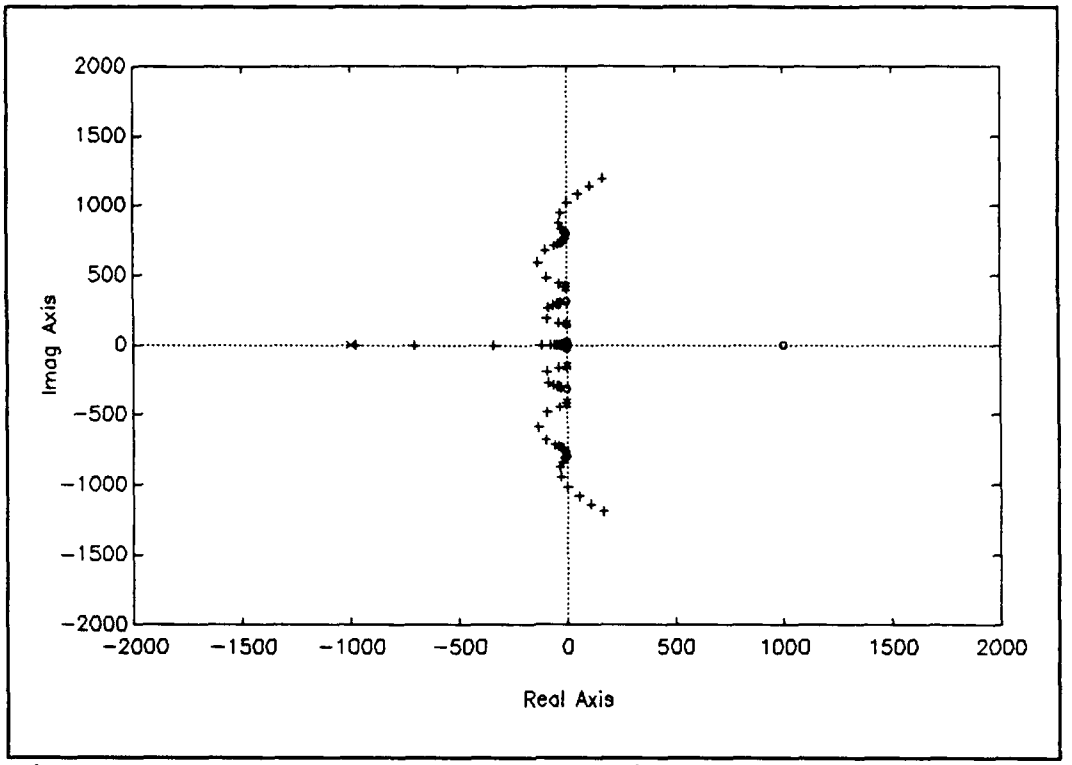


Figure 3.5 Root Locus Pattern Using a Collocated Sensor with Delay.

coefficients to an assumed rational transfer function. The equation above represents a first order approximate. Adding in the Pade' approximate and plotting the root locus shows the unstable behavior for the higher modes by their movement into the right half plane, depicted in Figure 3.5. Because only a four mode model was used for the root locus, it could not be used to determine which of the higher order modes should go unstable and at what gain values, but it does demonstrate the overall effect of the time delay in the feedback path.

A second attempt using the digital integrators was

demonstrated using the non-collocated (position 11) measurement. This time the results agreed well with simulations and the high frequency saturation was not observed. The high frequency signals were not present in the response because the position 11 measurement corresponds to a node location for all but the fundamental frequency (beam end mass installed) as will be shown in Chapter IV. Since this thesis explores blending collocated and non-collocated measurements, the inability to achieve satisfactory results with the collocated sensor forced an alternative to the digital integration process be employed.

As a second choice, analog integration was used. By placing the integrators in the feedback loop before the controller, the high frequency signals are naturally attenuated in the integration process and thus did not cause saturation problems. The analog integrators used were those available from previous work with the ACB by Jacques [13]. The integrators are based on the same design criteria as discussed for the digital integrators. Figure 3.6 shows the block diagram for each integrator. Two stages of amplification are required to achieve the desired output level without clipping the signal. Additionally, each integrator provides a zero adjust to null the signal prior to testing. Calibration data is contained in Appendix A.

A block diagram of the final measurement channels using

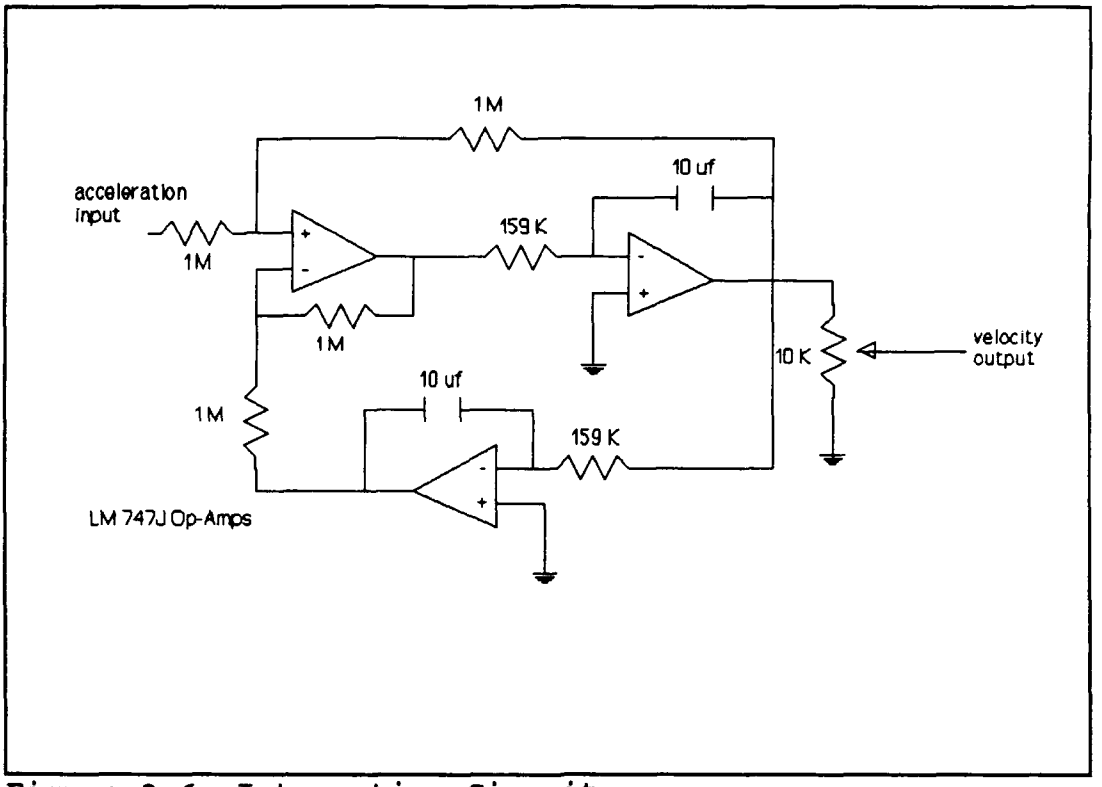


Figure 3.6 Integration Circuit

the analog integrators is shown in the Figure 3.7. Note that although not explicitly shown, the double sample period delay is present in the throughput of the controller. Pure collocated and pure non-collocated feedback tests were adequately performed using the analog integrators. Results will be discussed in the following chapter.

Modal Measurements

Open and closed loop measurements were obtained using a Tektronix 2642A four channel spectrum analyzer. Modal data was extracted from the analyzer plots using a STAR Modal

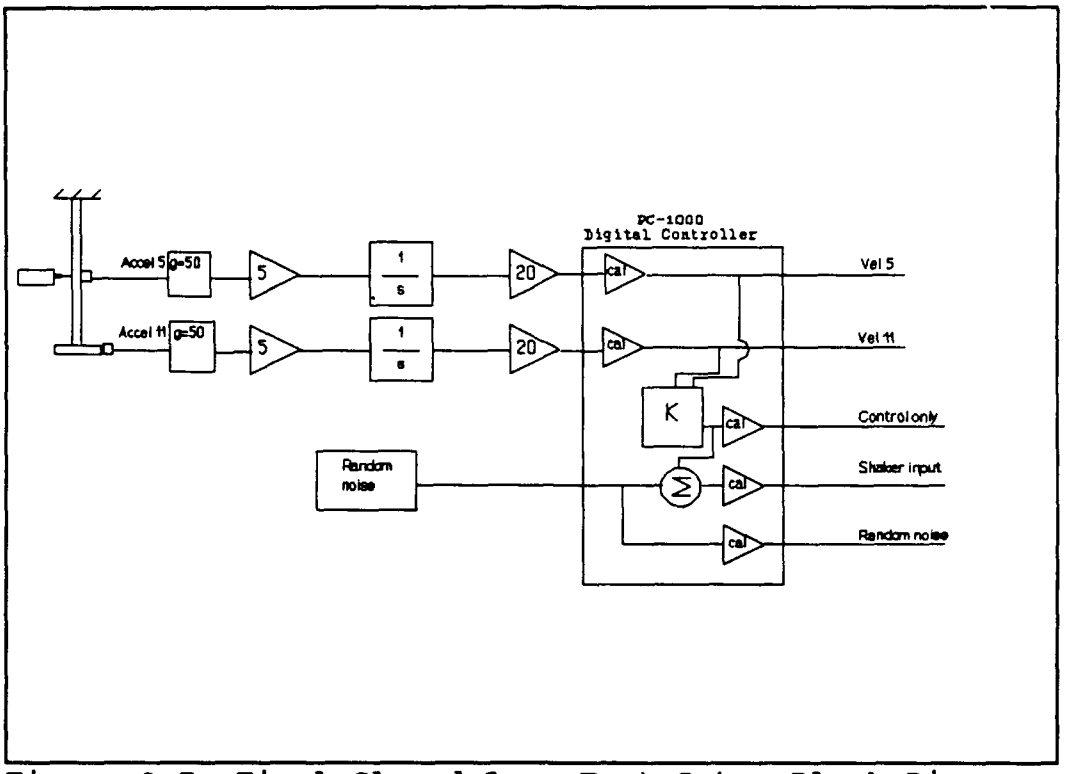


Figure 3.7 Final Closed Loop Test Setup Block Diagram.

software package. The software features a curve fitting routine which fits the measured frequency response functions and determines values for the modal frequencies and damping factors. Details of the analyzer and the software are contained in references 15 and 16 respectively. Although most data was obtained using the APS shaker as previously described, an impact hammer was also used for impulse response data and as an alternative check on closed loop measurements without using a random input. The impact hammer used was identical to the one used by McCall, and calibration procedures and specifications can be found in reference 17. Using impact testing, both frequency domain

and time domain results could be used to compute the damping and compared to the STAR Modal software. Frequency domain damping values are computed using Eqn 3.22 [8:97]:

$$\zeta = \frac{\omega_2 - \omega_1}{2\omega_n} \tag{3.22}$$

with ω_1 and ω_2 representing the -3 dB points on either side of the resonant spike ω_n. In the time domain, the log decrement method is used with the damping given as [8:61]:

$$\zeta = \frac{1n}{2\pi}\left[\frac{M_1}{M_2}\right] \tag{3.23}$$

with M_1 and M_2 representing the magnitude of the response on two successive peaks of the response plot. The log decrement method was used primarily for obtaining mode one damping factors. The poor frequency resolution at the lowest mode precluded accurate measurements of mode one damping using Eqn 3.22.

In summary, an eighth order state-space model of the ACB was developed using an FEM model. The model was tuned to match experimental data. Velocity measurements are obtained by passing the acceleration measurements through an analog integration circuit. In the next chapter, closed-loop results will be presented.

IV. Blended Control on ACB with End Mass

Open Loop Response

Before demonstrating the closed loop response on the ACB, validation of the analytical model was performed. Using the FEM model described in Chapter III, a four mode state-space model of the beam was obtained with an input at position five on the beam and outputs corresponding to the velocities at positions five, eight and eleven. To make direct comparisons between theoretical and experimental results, a conversion is required to convert between predicted velocity measurements and experimentally measured accelerations. This conversion is easily accomplished in the frequency domain by multiplying (dividing) each velocity (acceleration) measurement by the frequency (in rad/sec) to obtain the corresponding acceleration (velocity). This method was used throughout the thesis to make direct comparisons between experimental and analytical results when experimental accelerances were measured. Figure 4.1 shows the theoretical open loop frequency response obtained using the four mode FEM model for the three sensor locations. The system poles (natural frequencies of the structure) appear as spikes on the frequency plot whereas the zeros correspond

to the dips. Note that all three sensor locations have spikes at the same frequency. This is because the poles are determined by the physical properties of the system and are independent of sensor location. In contrast, as developed in Chapter II, the system zeros are a function of sensor location. The magnitude plot for each sensor location will have dips at different frequencies due to the different zero locations. Physically, the transmission zeros correspond to

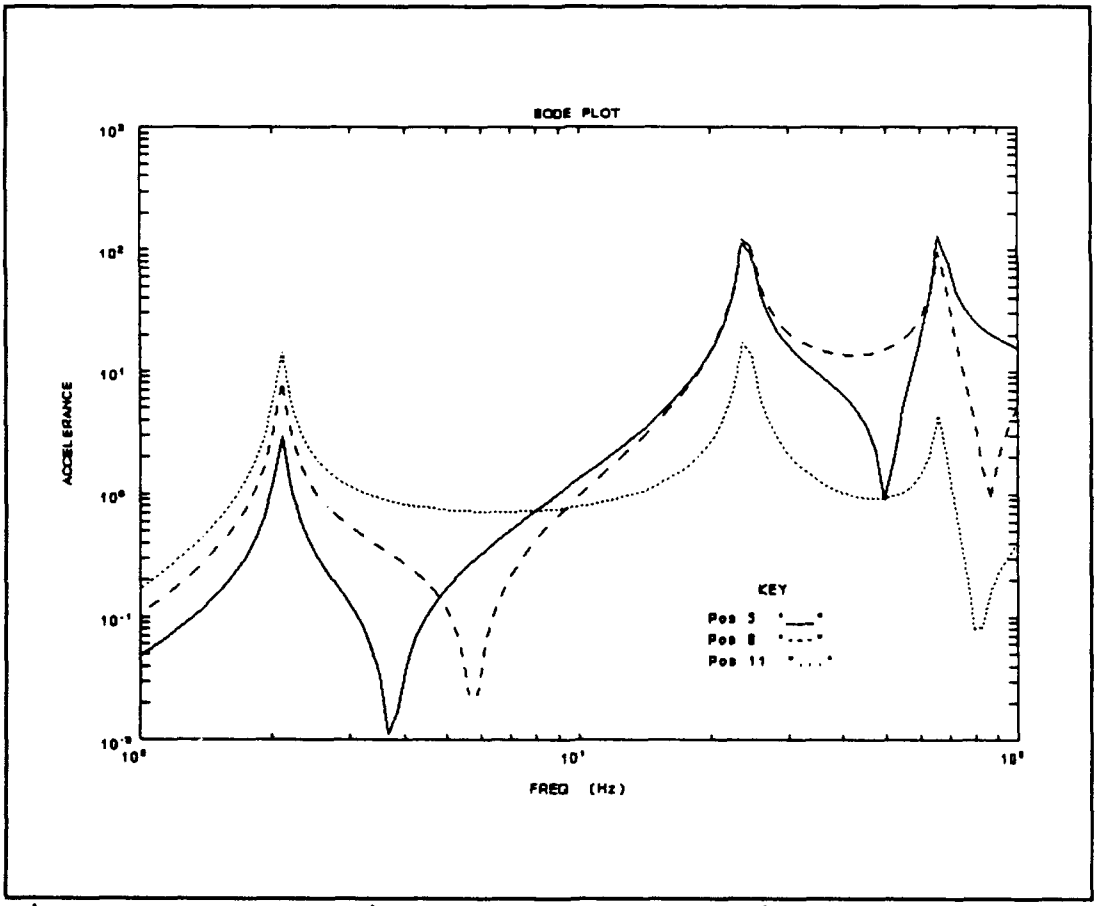


Figure 4.1 Theoretical Open Loop Comparison for the Three Sensor Positions.

frequencies at which sinusoidal actuator inputs are undetected by the sensor. As the sensor's position is changed, the transmission zeros also change. As expected, the collocated sensor output (position 5) has an alternating set of resonances (spikes) and anti-resonances (dips) which correlate to the alternating pole-zero pattern on the imaginary axis in the s domain. The non-collocated sensor (position 11) does not exhibit the alternating resonance/antiresonance pattern. This is due to the non-collocated sensor having zero locations which lie on both the real and imaginary axes in the s domain. The pole-zero locations are given in Table 4.1. The frequency plot in Figure 4.1 shows the relationship between the actuator/sensor separation and the location of the antiresonances. The further the separation distance is increased, the higher the frequency at which the first antiresonance will occur. For the pure non-collocated case of a free-free beam with fully separated sensor and actuator, the antiresonances occur only at infinity [9].

Table 4.1 Pole-Zero Locations for ACB with End Mass

	zeros	
poles (rad/sec)	pos 5	pos 11
±13.19i	±23.5i	±215
±151.4i	±316i	±507i
±417.2i	±769i	±2280

A comparison between the theoretical and experimental frequency response for the three sensor locations is shown in Figures 4.2, 4.3 and 4.4. The experimental frequency response was obtained by measuring the transfer function between a bandlimited (0-100 Hz) random noise excitation to the shaker and the three different accelerometer outputs. The ordinate axis is a measure of the accelerance and has units of ($ft/s^2/Lbf$). The actual transfer function measured by the spectrum analyzer is in terms of volts/volt. For direct comparison, the measurement is then scaled using the calibration constants of the shaker and the accelerometers

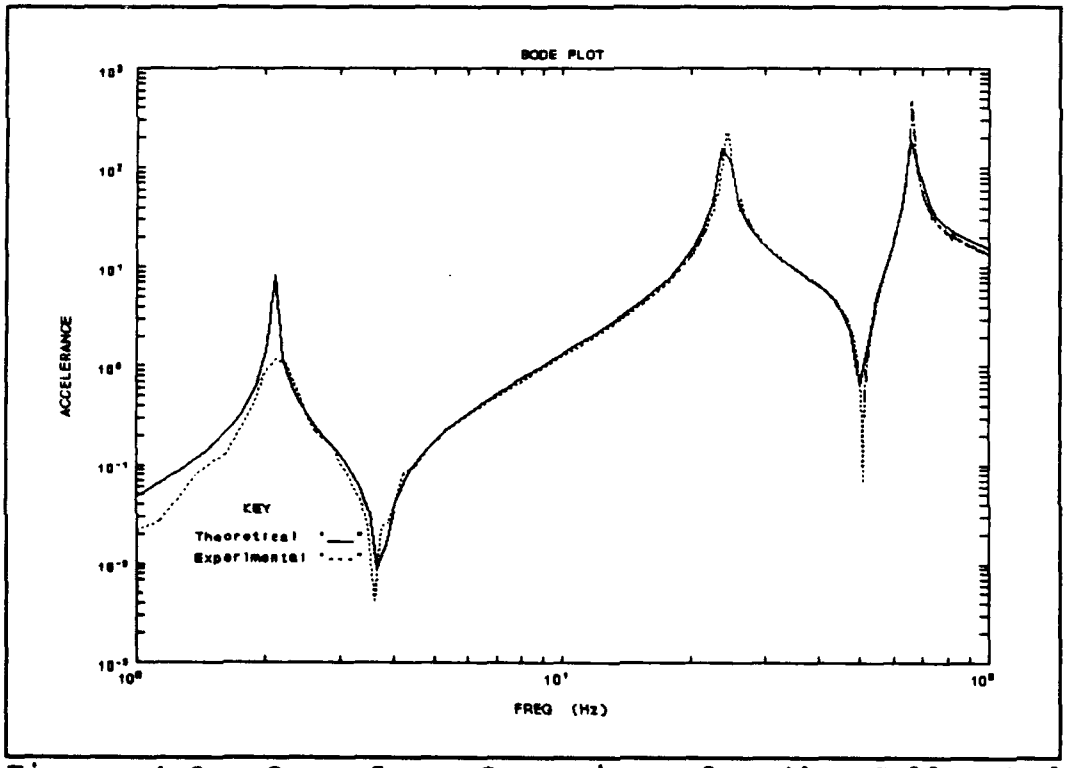


Figure 4.2 Open Loop Comparison for the Collocated Sensor (position 5).

found in Appendix A. The comparison plots show good agreement between the analytical and experimental data, with accurate representation of both the system poles and zeros for the three different sensor locations. A comparison between the modeled and measured natural frequencies is given in Table 4.2.

Table 4.2 Modeled and Measured Natural Frequencies

mode	modeled	measured
1	2.10 Hz	2.12 Hz
2	24.1 Hz	24.3 Hz
3	66.4 Hz	66.1 Hz

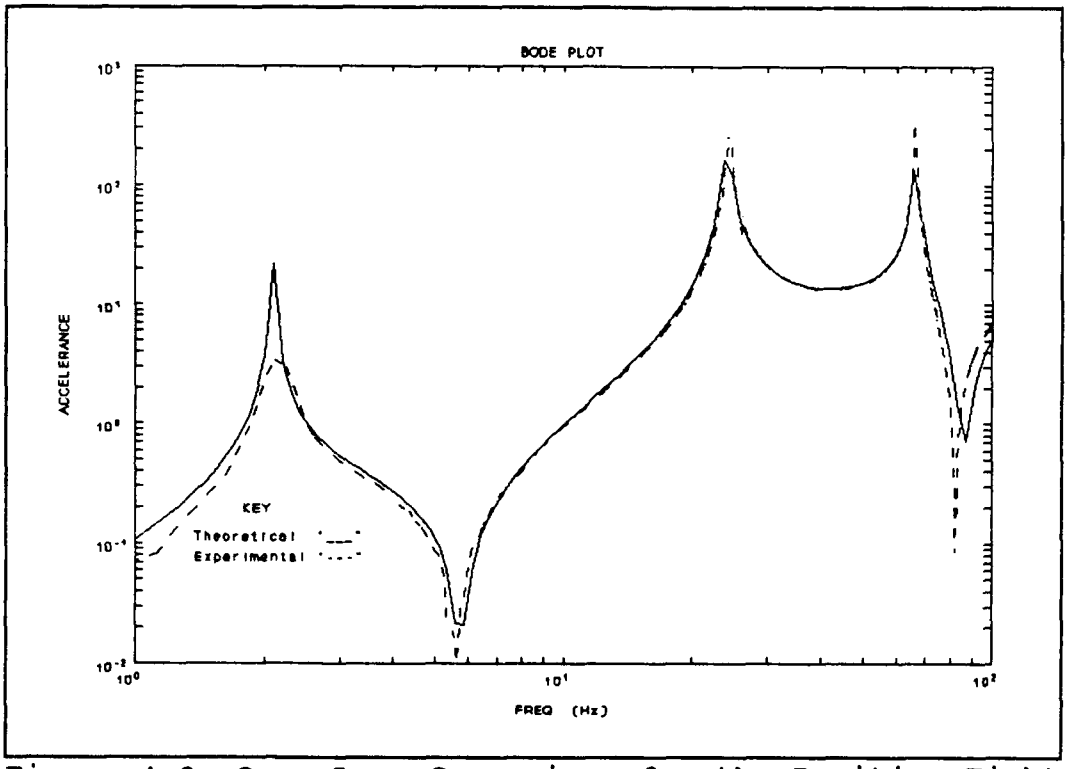


Figure 4.3 Open Loop Comparison for the Position Eight Sensor.

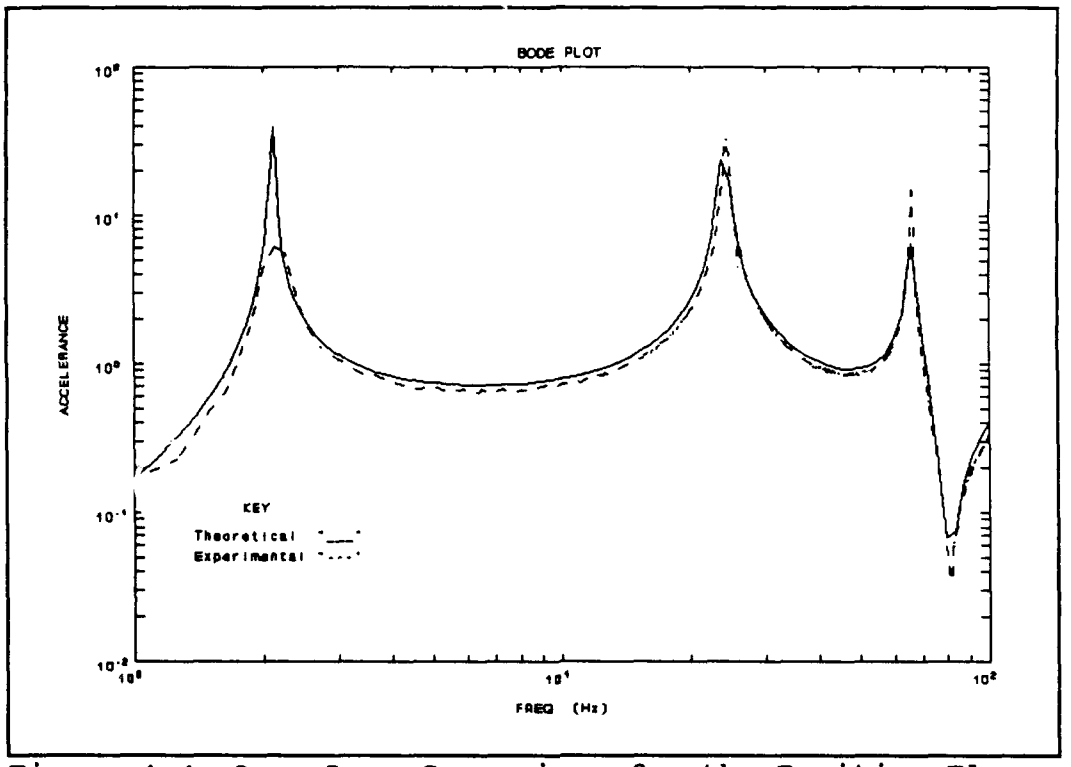


Figure 4.4 Open Loop Comparison for the Position Eleven Sensor.

To experimentally demonstrate the movement of the open loop zeros as a function of the blending ratio, a test was performed comparing the blended transfer function to the analytical blended results for a cantilevered beam. For the test, a blending ratio of .35 was chosen. This value yields ample movement of the zeros from the collocated measurement, yet has adequate separation between the zeros for easy identification. The experimental transfer function was obtained by measuring the output of the digitally added velocities of the collocated and non-collocated sensors

compared to a random input disturbance. Comparison to the analytical results is shown in Figure 4.5. The plot shows good agreement between the two, and demonstrates the movement of the transmission zeros towards each other as expected, without affecting the pole locations. For this comparison test, the end mass of the ACB was removed in order to make a direct comparison to the exact solutions of the cantilevered beam developed in Chapter II. Further testing of the ACB with the end mass removed will be presented in Chapter V. Table 4.3 lists the predicted and measured zero locations.

Table 4.3 Blended Zero Locations for $\alpha = 0.35$.

Exact	FEM	Experimental
21.38 Hz	29.2 Hz	~ 27 Hz
81.55 Hz	65.4 Hz	~ 70 Hz

The differences in the zeros between the FEM and the exact solution is due in part to the fact that the exact solution does not include the mass of the accelerometers and the shaker armature in the model, combined with the fact that the FEM model used is only a four mode model. The results do demonstrate that the experimental blended measurements, which will be used by the controller, follow the FEM model results closely.

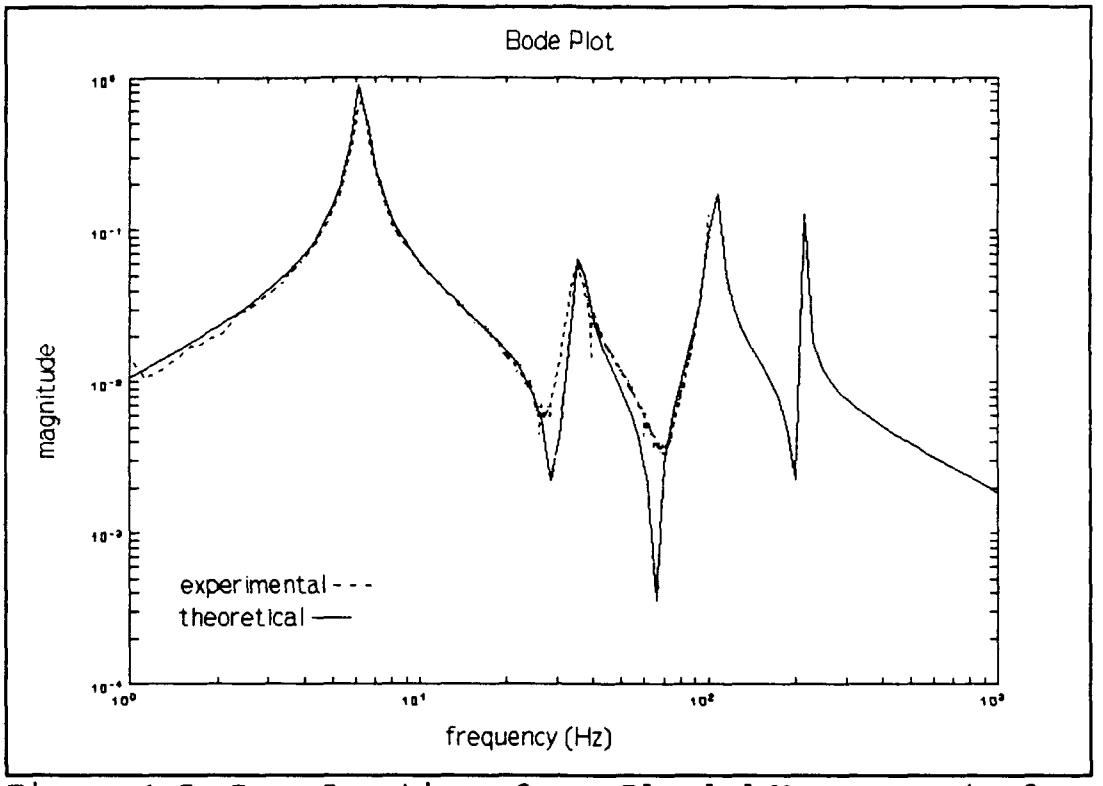


Figure 4.5 Zero Locations for a Blended Measurement of α= 0.35 .

Closed Loop Performance Criteria

To make a fair comparison between two control systems, performance criteria needs to be identified and compared with respect to a common reference. Possible criteria for comparison include closed loop bandwidths, modal damping factors, stability margins, root mean square (RMS) noise response and required control effort. To examine the blended measurement method, several criterion were applied.

Stability Comparisons The first comparison was performed by using negative proportional velocity feedback for both the collocated and non-collocated measurements and comparing them to that of the blended measurement. Closed loop stability for a single-input single-output (SISO) system is easily visualized using the root locus method. For SISO systems, stability can be examined by comparing the values of the feedback gain which cause instability. Figures 4.6 and 4.7 show the root locus patterns for the collocated and non-collocated measurements respectively. As

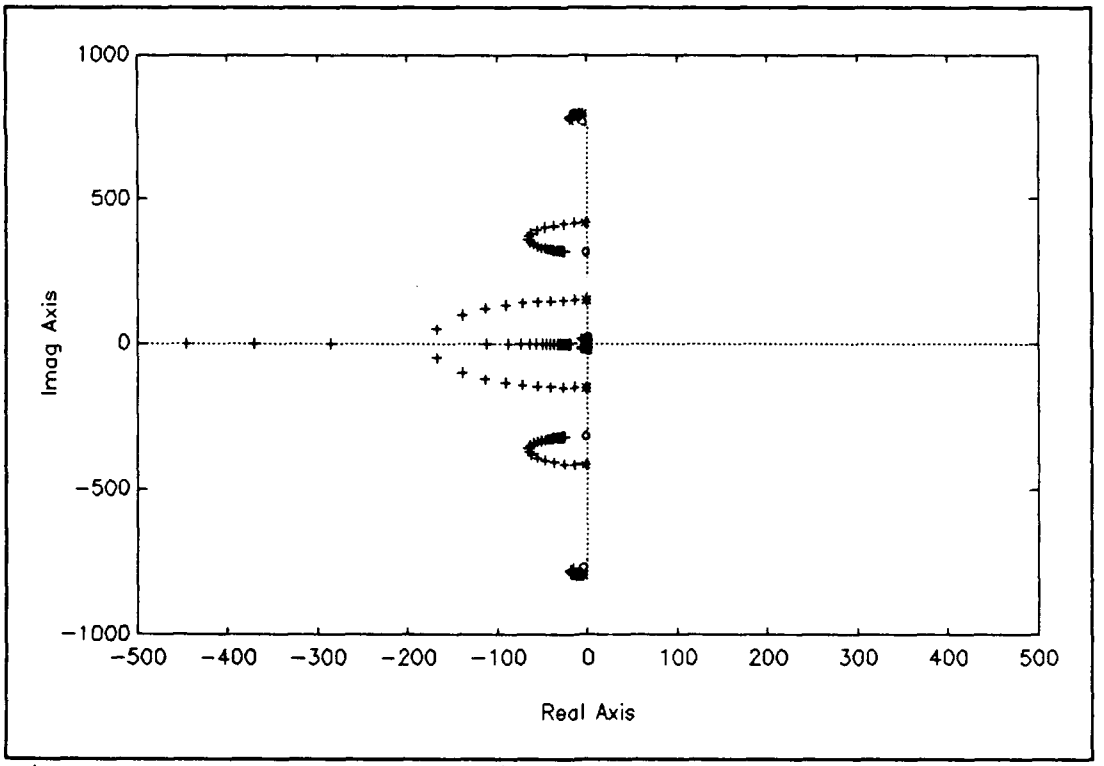


Figure 4.6 Root Locus Using Collocated Rate Feedback on the ACB with End Mass.

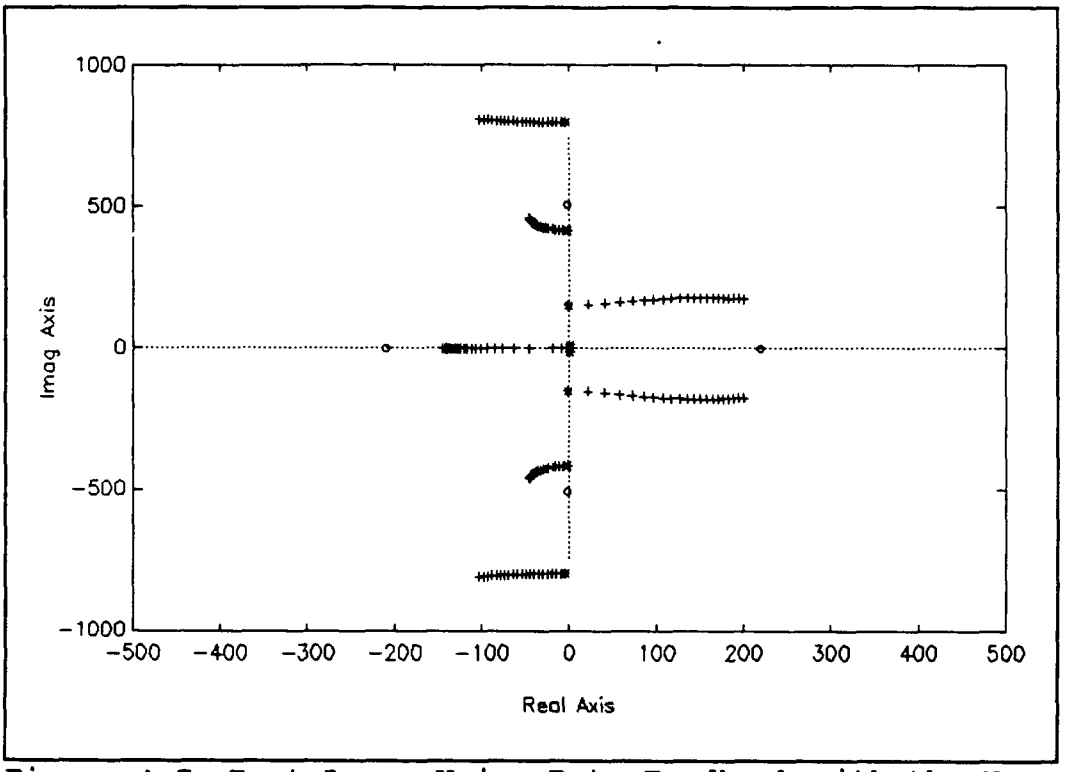


Figure 4.7 Root Locus Using Rate Feedback with the Non-Collocated Sensor on the ACB with End Mass.

can be seen from Figure 4.6, the collocated measurement is stable for all positive values of the proportional feedback gain k, as evidenced by the locus remaining in the LHP. In contrast, the non-collocated locus in Figure 4.7 shows the movement of the locus into the RHP. This is due to the non-minimum phase zeros. Instability occurs for a value of k greater than 4. This value is strictly determined by the amount of modal damping assumed in the model, which was based on experimentally measured values. For an undamped model, the system would be unstable for all values of k greater than zero. Modal damping used in the FEM model was

obtained by curve fitting the open loop frequency responses using the STAR Modal software.

A check on the damping values measured was performed using feedback of the position eleven measurement. Experimentally, the feedback gain was varied from one to ten in integer increments. The beam was then excited by applying an impact at the beam's midpoint to excite the higher frequency modes. The results showed the second mode was marginally stable for $k = 4$ and clearly unstable for higher values of k. To the precision of the test (instability at $k = 4 \pm 1$), the measured damping value for the second mode was considered accurate. This test also showed the limitation on using only the position eleven measurement in the feedback loop. Clearly a more sophisticated compensation scheme would be required to achieve adequate performance if this were the only measurement used.

Bandwidth Comparisons The anticipated advantage of the blended measurement is an increase in the achievable closed loop bandwidth while maintaining the stability properties of the collocated case. Bandwidth is a measure of a systems ability to track a sinusoidal input. The bandwidth is defined as the frequency at which the response is down 3 dB from the value of the steady-state closed loop gain. For

the collocated case, the upper limit of the bandwidth is bounded by the location of the first zero. However, the non-collocated sensor does not have this antiresonance and thus the bandwidth does not have this limitation. This led Lee [1] to the conclusion that the controller using a non-collocated sensor would have a higher achievable bandwidth. Following this assumption, to achieve the greatest possible bandwidth and maintain stability, an initial choice of the blending ratio is one in which the weighting on the non-collocated measurement is greatest while maintaining a minimum phase system. This value can be chosen by plotting the open loop zeros as a function of the blending ratio. Figure 4.8 shows the location of the zeros for an increasing blending ratio. The poles of the system are unaffected by the blending ratio since they are dependent on the physical properties of the system and not the sensor locations. Note that the pattern for the ACB exhibits the same behavior as was demonstrated in Chapter II for the non-dimensionalized beam. The additional mass and inertias added into the FEM model for the ACB does not alter the basic pattern. Using this method, a value of α equal to 0.85 represents the greatest blending ratio while maintaining a minimum phase system. With this bound on α, the system is stable for all positive values of k.

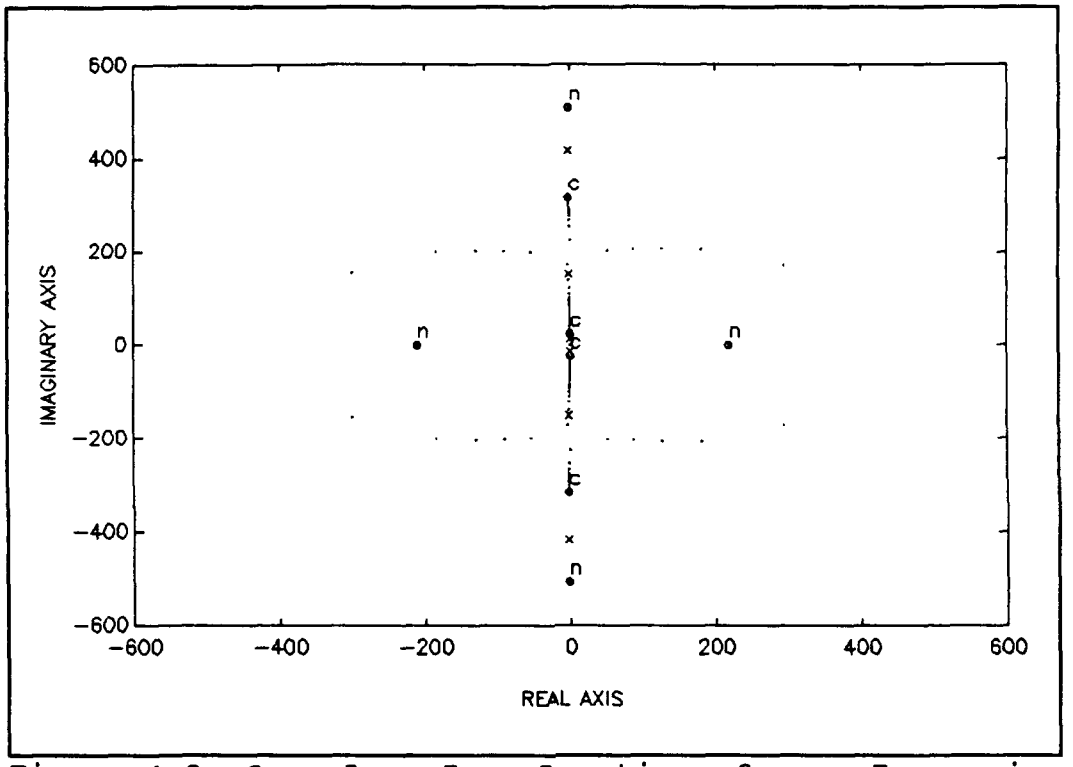


Figure 4.8 Open Loop Zero Locations for an Increasing Blending Ratio.

The bandwidth can now be calculated using the blended measurement by evaluating the output position as a function of the commanded input frequency and determining the -3 dB point from the steady-state gain. For the ACB however, a velocity loop is closed rather than a position loop, and an alternative method of determining bandwidth must be used. This configuration is comparable to the control of flexible structures where an inner and outer loop control scheme is used. The inner loop is dedicated to controlling relative velocities and positions, whereas the outer loop controller must maintain control of the absolute (rigid body)

velocities and positions. For this thesis, it was decided to define the bandwidth in the usual manner and simply derive the position measurements from the velocity measurements by an integration. In the frequency domain, this corresponds to a division by the frequency at each value. While it is recognized that this is not a true measure of bandwidth, it is in the author's opinion that for control systems such as the ACB where only velocity loops are closed, this method is acceptable for comparison purposes between two candidate control systems.

Defining bandwidth as discussed above, with the output taken at an intermediate position along the beam (position eight), the resultant bandwidth for collocated and blended measurement was compared. Both systems had essentially the same bandwidth and the anticipated increase in bandwidth was not achieved. This is due to the fact that the open loop and closed loop zero locations are identical. The previous work suggesting higher achievable bandwidths made comparisons at two different output locations, one collocated, the other non-collocated. In an actual control system, the designated output should be a fixed position on the structure with a desired performance. For a gimbal mechanism, this may correspond to the midpoint on the gimbal where a line of sight error is measured. Once this physical output location is fixed, the transmission zero between the

actuator and the position is fixed and can not be altered under feedback. To demonstrate this, consider the block diagram of the SISO system shown in Figure 4.9. The open loop transfer function is written as:

$$\frac{y}{r} = C_o\,[sI - A]^{-1}\,B \qquad (4.1)$$

which can be expressed in polynomial form as:

$$\frac{y}{r} = \frac{n_o}{D}\ ,\quad n_o \triangleq \prod_i (s + z_i)\ ,\quad D \triangleq \prod_i (s + p_i) \qquad (4.2)$$

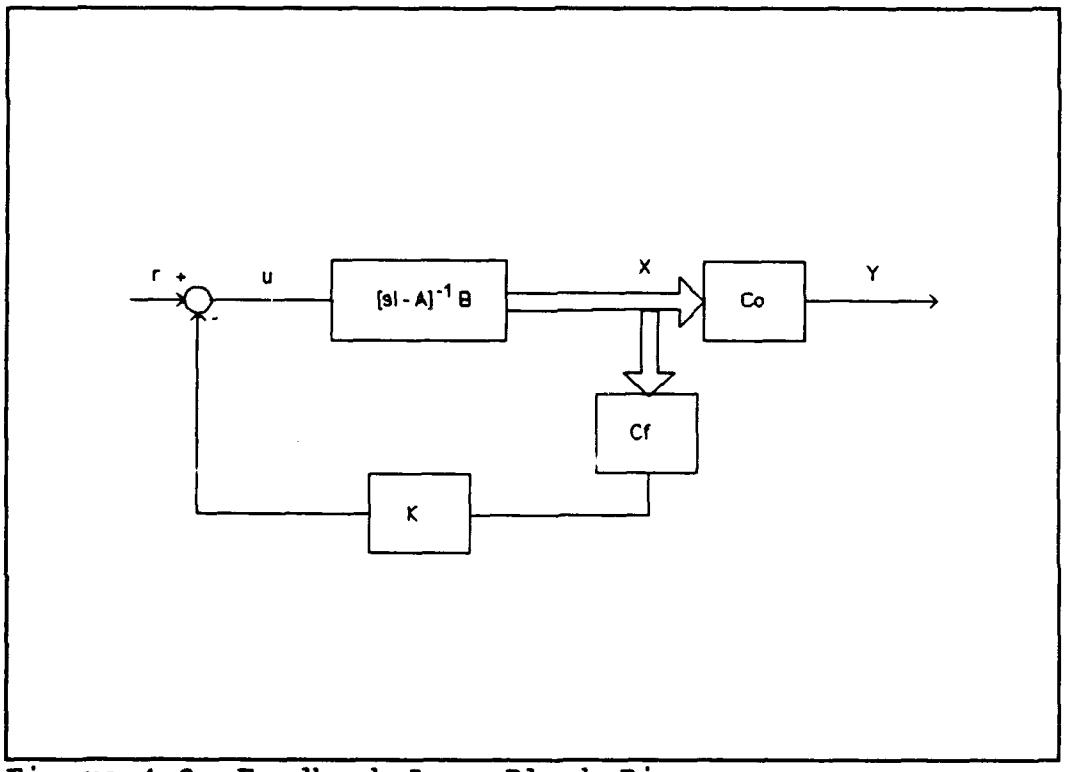


Figure 4.9 Feedback Loop Block Diagram.

With p_i and z_i defined as the open loop poles and zeros. For the closed loop system, the output can be written as:

$$y = C_o \underline{x} = C_o \, [sI - A]^{-1} \, B \, u \tag{4.3}$$

and the control input as:

$$u = r - K \, C_f \, \underline{x} \tag{4.4}$$

where the state vector $\underline{x}$ is expressed as:

$$\underline{x} = [sI - A]^{-1} \, B \, u \tag{4.5}$$

Combining Eqns 4.3, 4.4 and 4.5, the control is equivalently:

$$u = \frac{r}{1 + K \, C_f \, [sI-A]^{-1} \, B} \tag{4.6}$$

and the closed loop transfer function found from combining Eqn 4.3 and 4.6 is:

$$\frac{y}{r} = \frac{C_o \, [sI - A]^{-1} \, B}{1 + K \, C_f \, [sI - A]^{-1} \, B} \tag{4.7}$$

To see the equivalence with Eqn 4.1, define the following:

$$C_f \, [sI - A]^{-1} \, B \triangleq \frac{n_f}{D} \tag{4.8}$$

such that the transfer function in polynomial form is given by:

$$\frac{y}{r} = \frac{n_o}{D + K n_f} \tag{4.9}$$

which has the identical zeros as in Eqn 4.2.

Although a primary consideration in exploring the blended measurement was the aspect of a higher achievable bandwidth, the stability and simplicity of using the blended method warranted further investigation into its performance.

Root Mean Square Response For a given value of the blending ratio, a fair comparison can only be made for particular values of the feedback value k that match a second criteria. For comparison, the value of the RMS response at position eight to a given input disturbance for the different cases was chosen. Additionally, the control effort can be compared by evaluating the RMS response of blended measurement (used as the controller input) and multiplying it by the feedback gain k.

As derived in Kwaakernack and Sivan [23], the RMS response of a system driven by zero mean stationary white noise is found from the solution of the Lyapunov equation:

$$AX + XA^T + BQB^T = 0 \tag{4.10}$$

where A and B are as defined in the closed loop state space equations, Q is a diagonal matrix containing white noise input intensities, and X represents the covariance matrix of the states. The RMS output is then found by forming the output covariance matrix,

$$Y = CXC^T \tag{4.11}$$

and computing the square root of the sum of the diagonal entries. For the SISO case, Y will be a scaler corresponding to the square of the output measurement.

Using this method, the RMS value of the output was found as follows. The state-space equations including random disturbance (v) and random measurement noise (w) are:

$$\begin{aligned} \dot{\underline{x}} &= A\underline{x} + Bu + Ev \\ \underline{y} &= C\underline{x} + Fw \end{aligned} \tag{4.12}$$

and using the control law u = -Ky the closed loop state equation is:

$$\dot{\underline{x}} = [A-BKC]\ \underline{x} + [E,\ -BKF]\begin{bmatrix} v \\ w \end{bmatrix} \tag{4.13}$$

which is a linear system driven by white noise. The RMS response is then found from Eqn 4.10 and 4.11 with the A, B and Q matrices as defined in the closed loop Eqn 4.13.

Closed Loop Results

A comparison of the RMS response at position eight was performed by applying a 70mv RMS (.376 Lbf) bandlimited , 0-100 Hz, random input to the control actuator. The RMS value of the position eight sensor was measured using the spectrum analyzer. A theoretical comparison was performed using Eqn 4.10 matching the theoretical white noise disturbance intensity to the experimental intensity. The results are shown in Figure 4.10, which reveals that as the blending ratio is increased, the RMS value at the position eight sensor is also increased. This result is a consequence of the blended zeros moving towards the second flexible pole and effectively notching out the feedback signal at that frequency. For higher order models, this notching effect will occur at multiple higher frequency flexible modes. The discrepancy between theoretical and experimental data is attributed to the finite order model used as well as the unmodeled dynamics of the control equipment. As illustrated in Figure 4.10, the best blending ratio based on the RMS response alone would be to set the blending to zero and use just the collocated sensor. A second comparison was performed by comparing the required control effort. The control effort required as a function of the feedback gain k was compared for the collocated and blended measurements as

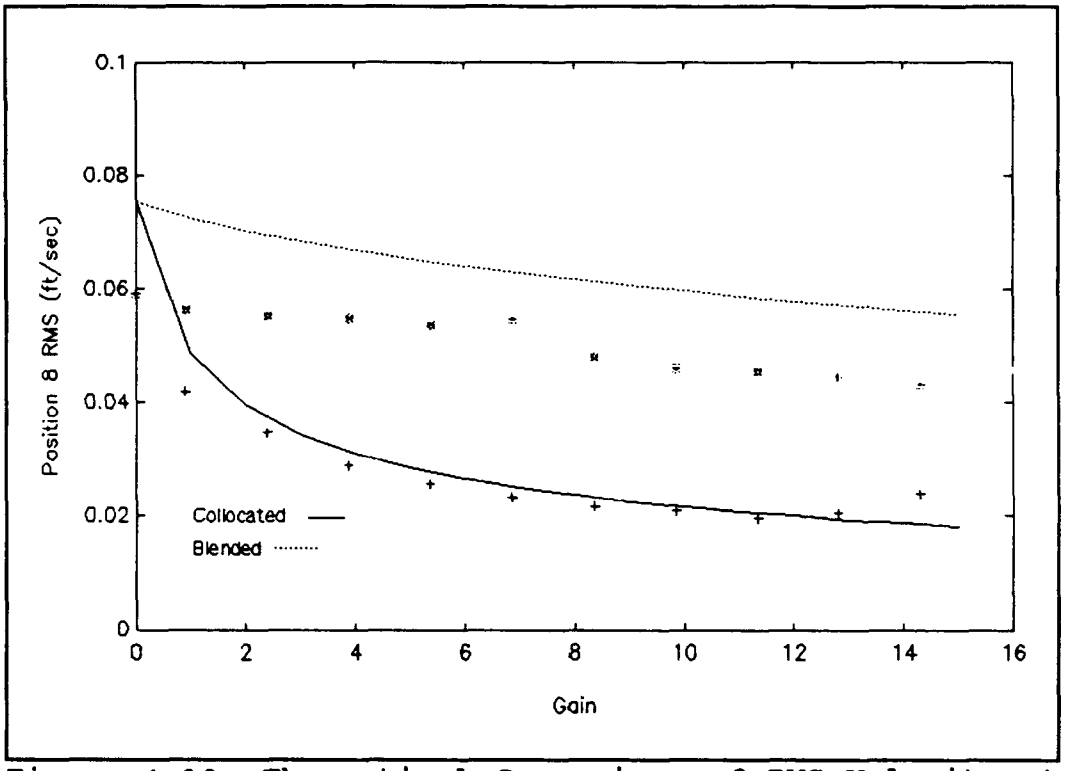


Figure 4.10 Theoretical Comparison of RMS Velocity at Position Eight for both Collocated and Blended Feedback.

shown in Figure 4.11. Characteristic of the results is the fact that the blended measurement control lies below the control effort required for collocated control. This trend is again due to the fact that the blended control has notched out the second mode. As a result, little mode two information is observed and hence little control effort is spent controlling the second mode. Matching the control effort for the two cases of 0.08 Lbf RMS corresponds to a gain of 2.4 for the collocated measurement and 14.3 for the blended measurement with $\alpha = 0.85$. The control laws were then implemented on the PC-1000 and the corresponding closed

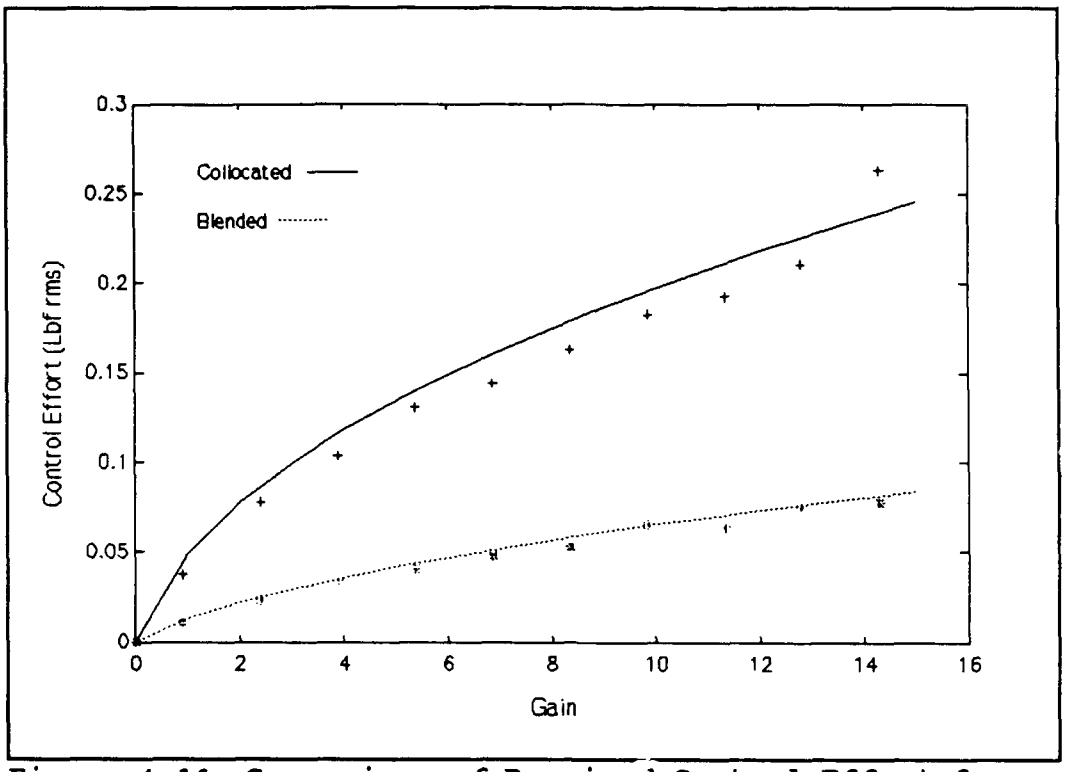


Figure 4.11 Comparison of Required Control Effort for an Increasing Feedback Gain.

loop transfer functions are shown in Figure 4.12 for the measurement taken at position five. It should be noted that the experimental data shown in Figure 4.12 was produced for illustration purposes using a wide bandwidth to show multiple modes. Actual damping values were computed using a much narrower bandwidth at the frequency of the mode of interest as well as using the log decrement method for calculating mode one damping. Table 4.4 contains the values obtained for the damping factor for the first three modes.

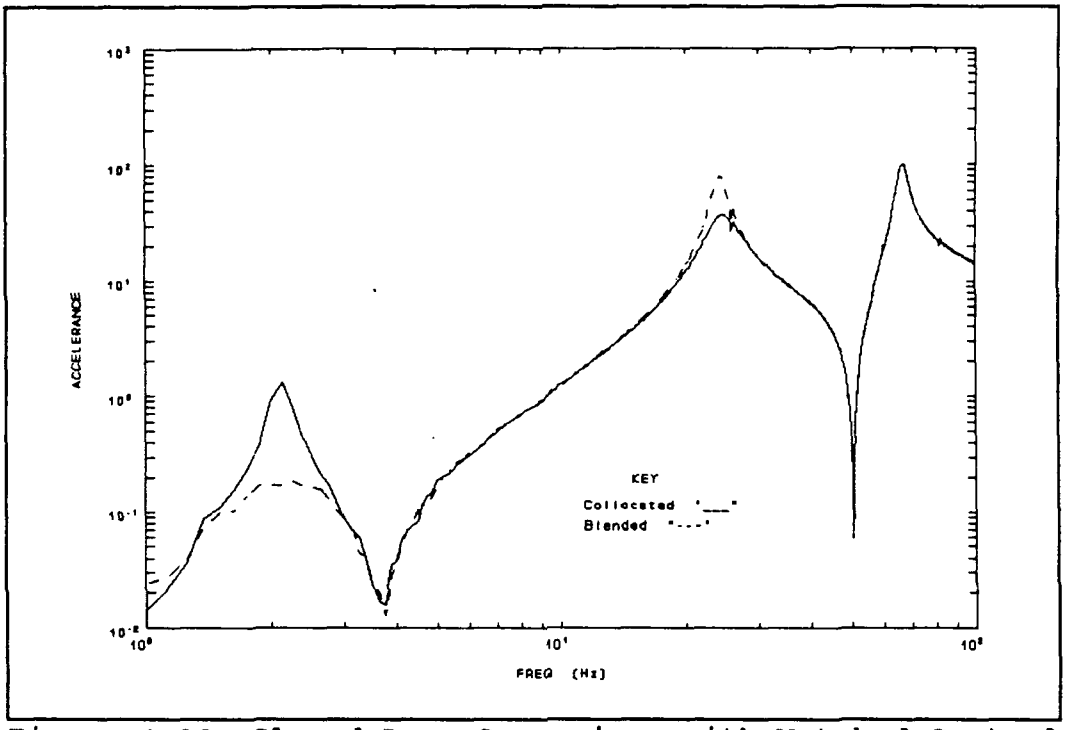


Figure 4.12 Closed Loop Comparison with Matched Control Effort.

Table 4.4 Damping Factors (%) for Matched Control Effort

	collocated		blended		open loop
mode	predicted	measured	predicted	measured	
1	2.1	2.3	28.7	26	1.00
2	6.20	8.0	1.87	2.5	1.20
3	2.32	2.8	2.41	2.8	0.60

As a test of stability, the gain for both control laws was increased and the performance evaluated. Since both systems are minimum phase, the only limit to the gain increase is the limitations on the control equipment. Using only the collocated sensor, gains greater than 14 yielded undesirable results. The high feedback gain produced an audible high frequency pitch from the actuator which was a

result of attempting to drive the actuator at frequencies above its operating bandwidth. The same behavior occurs for the blended measurement, but not until the gain is greater then 40. This result is due to the fact that the non-collocated sensor is close to a node point for the higher frequency modes and is therefore less sensitive to the high frequency limitations of the control equipment.

Evaluating the results above for the matched control effort, it is evident that the collocated measurement is effective in controlling the second and third mode while minimum control is exhibited over mode one. In contrast, the blended measurement is effective at controlling mode one while being ineffective at the higher modes. This suggests decreasing the blending ratio to more evenly distribute the control over the first two modes. This can be accomplished by setting the blending ratio to 0.4 which yields an identical damping value for the first two modes for a given overall gain. The results of using this controller are presented in the next section.

Comparison of Blended to LQG Methods

The above results showed that by adding a second sensor, a second parameter was introduced into the control law and hence both the magnitude and relative ratio between

the first two modes could be controlled. A more conventional approach to achieving this using a single sensor would be to use an estimator to recreate the states and then use proportional feedback on the estimated states. To experimentally compare the results between using state reconstruction and blended techniques a Linear Quadratic Gaussian (LQG) compensator was implemented. An LQG compensator is the combination of a Linear Quadratic Regulator (LQR) with a Linear Quadratic Estimator (LQE). One advantage of using LQG is that the regulator and estimator can be designed independently, with the closed loop poles being the union of the regulator and estimator poles.

LQG Theory The regulator is designed assuming full state feedback with the control law:

$$\underline{u} = -K\,\hat{\underline{x}} \tag{4.14}$$

where $\hat{\underline{x}}$ is an estimate of the state vector. A linear quadratic cost function is defined as:

$$J_k = \int_0^\infty (\underline{x}^T Q_c \underline{x} + \underline{u}^T R_c \underline{u})\, dt \tag{4.15}$$

where Q_c is the state weighting matrix and R_c is the weighting on control usage. Selection of Q_c and R_c are dependent on the relative importance between speed of response and the control effort required. If the state-space pair [A,B] is completely controllable, then a solution for the K matrix used in Eqn 4.14 which minimizes Eqn 4.15 exists. For control on the ACB, Q_c and R_c were chosen such that the eigenvalues of [A-BK] yielded the desired closed loop damping values.

The estimated state vector used in Eqn 4.14 is formed using the following observer equation:

$$\dot{\hat{x}} = A\,\hat{x} + B\,u + L(y - C\hat{x}) \qquad (4.16)$$

The estimator gain matrix L given in the observer equation is found by minimizing the cost function:

$$J_L = \int_0^\infty (x^T Q_e\, x + y^T R_e\, y)\, dt \qquad (4.17)$$

which exists when the pair [A,C] is completely observable. The matrices Q_e and R_e represent the process and measurement noise covariances respectively. To take full advantage of the LQG method, a statistical measure of the process and

measurement noise is required. Since a statistical characterization was not performed, the weighting matrices where chosen such that the estimator poles, (eigenvalues of [A-LC]), had the desired damping. Using previous results form Cristler [18], a 20 - 30 % estimator damping ratio was chosen for initial testing. A more formal discussion of LQG theory is presented in Ridgely and Banda [24].

Implementation of the LQG compensator on the digital controller is performed as follows. Given the state-space equations

$$\dot{\underline{x}} = A\underline{x} + Bu \tag{4.18}$$

$$\underline{y} = C\underline{x} \tag{4.19}$$

Eqns 4.14 and 4.16 for the regulator and estimator can be combined to yield:

$$\dot{\hat{\underline{x}}} = (A - BK - LC)\hat{\underline{x}} + L\underline{y} \tag{4.20}$$

which is the governing equation for the controller. In the development of Eqn 4.20, it is assumed the control (u) sent to the plant is identical to that given in the regulator equation. If the actuator output force is different, due to a saturation limit, the actual control force exerted should

be fedback for the state estimation. The discrete equivalent to Eqn 4.20 is given by [25:296]:

$$\underline{x}_{k+1} = e^{A_{LK}T}\underline{x}_k + A_{LK}^{-1}[e^{A_{LK}T} - I]L\underline{y}_k \tag{4.21}$$

where T is the sample period, and A_{LK} defined as:

$$A_{LK} \triangleq [A - BK - LC] \tag{4.22}$$

The matrix partitions given previously in Eqn 3.15 for the PC-1000 digital controller is then:

$$\begin{aligned} F_{11} &= 0 & F_{12} &= -K \\ F_{21} &= e^{A_{LK}T} & F_{22} &= A_{LK}^{-1}[e^{A_{LK}T} - I] \end{aligned} \tag{4.23}$$

The partitions F_{21} and F_{22} were computed using MATLAB's C2D algorithm. Regulator and estimator gains K and L were computed using the LQR and LQE algorithms in MATLAB.

LQG Results The objective of using the LQG controller was to experimentally compare the blended control using two sensors to the LQG controller using a single collocated sensor. A performance goal of 15% damping for the first two modes
was arbitrarily set. For the blended method, the blend ratio was chosen to provide equal damping on the first two

modes (α = 0.4) and then the gain was selected to yield the 15% target value (k = 12.1). For the LQG design it was decided to use a fourth order model for the estimator to provide the estimates of the first two modes. The estimator model was produced by retaining only the first two bending modes from the FEM model. The estimator gains were chosen by adjusting the noise covariance values in Eqn 4.17 to obtain the desired estimator damping. Numerous iterations on the estimator damping values were tested. The best results were achieved using damping values 2-3 times the desired modal damping values. The lightly damped estimators did not produce the desired modal damping, while the more heavily damped estimators resulted in an excessive dc drift from the controller. Once the estimator design was complete, the regulator gains were computed using Eqn 4.15 by varying the state weightings and the control penalty to yield the desired 15% damping values. The resulting compensator in polynomial form is given below:

$$G_{LQG}(s) = \frac{(s+3.78)(s+20.3\pm80.7i)}{(s+67.5\pm145i)(s+5.58\pm13.4i)} \qquad (4.24)$$

The resulting closed loop responses using the two control laws is shown in Figure 4.12. The obtained modal damping values are tabulated in Table 4.5.

Table 4.5 Damping Factors for Blended and LQG Controllers

	blended		LQG	
mode	predicted	measured	predicted	measured
1	15.0	15	15.0	12
2	15.0	17	15.0	14.5

The results show that both methods were capable of damping modes one and two, although there was a greater discrepancy between the predicted and experimental results for the LQG controller. This is in part due to the fact that only a two mode model was used in the estimator while the measurements still contain information on the higher modes with a potentially destabilizing effect. This is illustrated in Figure 4.13 where the third mode remained close to its open loop value. Use of model suppression techniques or a higher order compensator may produce more predictable results. Additionally, there is a relationship between the estimator damping factors and the achievable damping values which requires further characterization.

Comparing the form of the compensator in Eqn 4.24 to that using a blended method, the simplicity of the blended method is apparent. Both the controllers are minimum phase and are stable for all gain variations within the limits of the equipment.

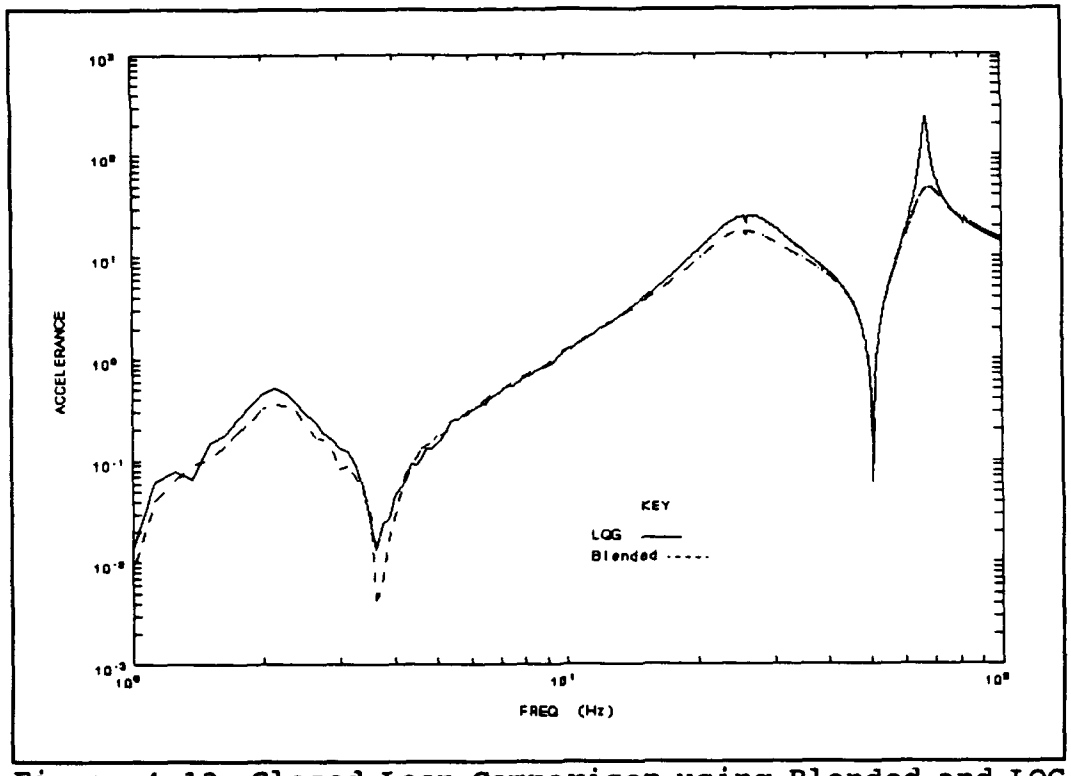


Figure 4.13 Closed Loop Comparison using Blended and LQG Compensation.

Conclusions

Closed loop control on the ACB with end mass was demonstrated using a single measurement feedback and blended measurement feedback. The clear advantage of the collocated measurement case is the global stability aspect, although it was shown that in the presence of controller digital delays and noisy measurements, the stability was limited to the performance of the feedback control equipment. For the non-collocated sensor, closed loop performance was limited by

the amount of natural damping present in the system, and hence pure non-collocated rate feedback has very limited performance for lightly damped structures. A higher order compensator would be required to achieve satisfactory results with the non-collocated measurement.

For the blended measurement, it was shown that blending ratios of .85 and below resulted in stable responses for all positive values of the feedback gain similar to the collocated case. Alternatively, for a matched control effort for a given input disturbance, it was shown that greater damping of the first flexible mode could be achieved than with the collocated sensor alone. The disadvantage of the blended measurement, in addition to the fact that an additional piece of hardware is required, is the decrease in effectiveness of damping the second mode. The inability to dampen the second mode is due to the approximate pole-zero cancellation which occurs as the blending ratio is increased.

Comparing the blended and LQG methods, both methods were capable of adequately controlling the low frequency modes. The LQG compensator was more difficult to design and implement, but required only a single sensor. It does have the limitation of only being able to control modes which are modeled by the estimator, and therefore the compensator

order continues to increase to control the higher modes. Both systems were minimum phase.

In summary, neither the anticipated increase in bandwidth nor a decrease in RMS response was realized using the blended measurement on the ACB. The previous work suggesting this used different output locations when making comparisons. For a fixed output location, such as the position eight sensor on the beam, the bandwidth was limited by the location of the first zero. It was shown that the zero location is not altered using collocated or blended feedback. The decrease in RMS was not achieved due to the poor observability of some of the modes using blended feedback. It does however, have some advantages. In addition to simplicity, the two parameters available provide the ability to set the ratio of control expended on the first two modes using α and then set the overall damping using k. Based on these results, a design tradeoff exists between using an additional sensor with a simple control law to that of a single sensor and a more sophisticated control law. The overall merits of the blended measurement will depend on the actual task and required design specifications and the physical properties of the structure.

V. Closed Loop Control on ACB Without End Mass

Mode Shape Comparisons

A second comparison case of using single and blended measurements was performed using the ACB with the end mass removed. Without the end mass, the modal information sensed by each of the accelerometers is dramatically different. This can easily be seen by comparing the mode shapes for the first four modes of the beam in the two configurations. Figure 5.1 shows the mode shapes for the beam with end mass installed while Figure 5.2 shows the mode shapes with end mass removed. The mode shapes were obtained from the eigenvectors of the ten element FEM model which were used to diagonalize the global mass and stiffness matrices. The same result could be obtained experimentally by taking transfer functions for each of the ten nodes and then extracting the modal information using STAR Modal software. The mode shapes shown were normalized with respect to the maximum displacement for each mode.

For the beam with end mass, the collocated sensor contains information about the first four modes as shown by the amplitude of the mode shape at position five. In contrast, the sensor at the tip is primarily composed of

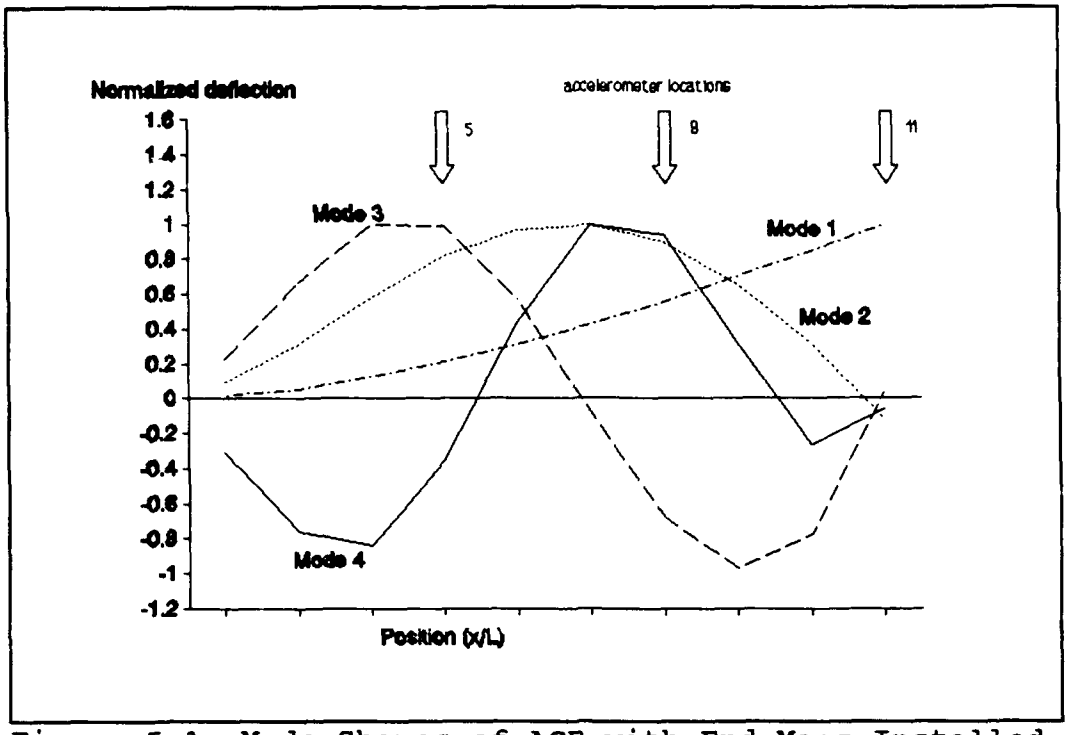


Figure 5.1 Mode Shapes of ACB with End Mass Installed.

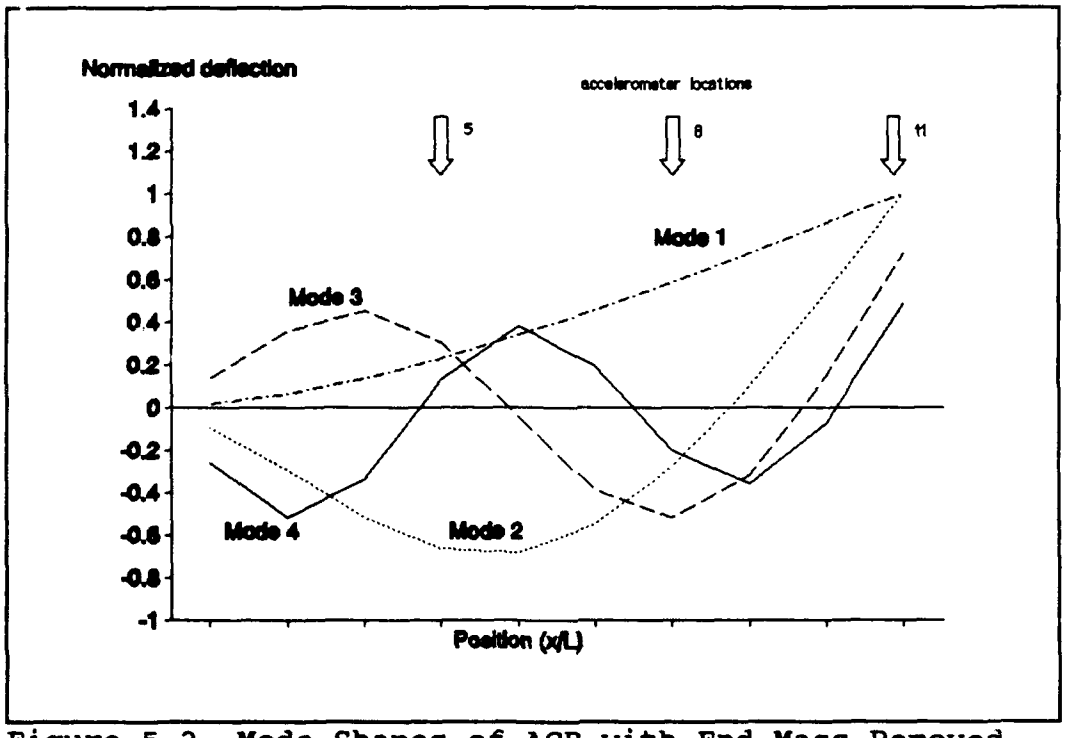


Figure 5.2 Mode Shapes of ACB with End Mass Removed.

mode one information only. For the higher modes, this position corresponds to a node where the beam acts as a fixed-pinned beam for all modes except mode one. When the end mass is removed however, both the position five and position eleven sensor information will contain modal information for the first four modes. Because of this difference, the blending test was repeated for this second configuration to compare and contrast with the first case results.

Open Loop Response

For analytical simulations, the FEM program was rerun setting the mass and rotary inertia terms at the end to zero. An iteration on the beam modulus was done to match the measured natural frequencies as close as possible. Modal damping factors were then added to the model based on the experimental open loop measurements. Comparisons between the analytical frequency response and the measured frequency responses for the collocated and the non-collocated sensor are shown in Figures 5.3 and 5.4 respectively. Again there is good agreement in modeling both the system poles and zeros for each of the measurements. Table 5.1 shows the values of the poles and zeros for the two measurements. Not listed are the zeros at

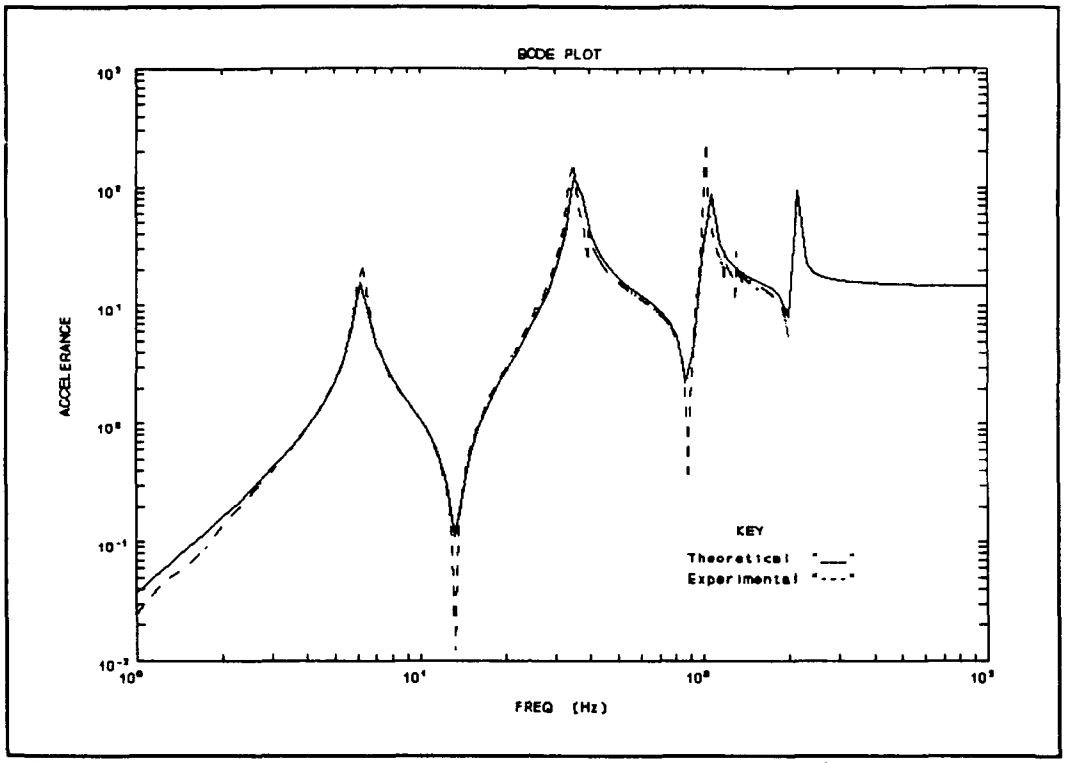


Figure 5.3 Open Loop Response of ACB with End Mass Removed for the Collocated Sensor.

the origin corresponding to velocity and acceleration measurements. Note that again the non-collocated sensor does not have the alternating pole-zero pattern characteristic of the collocated sensor.

Table 5.1 Pole-Zero Locations for ACB Without End Mass

	zeros	
poles (rad/sec)	pos 5	pos 11
±39.3i	±84.5i	±202
±218i	±563i	±840i
±644i	±1307i	±1069i

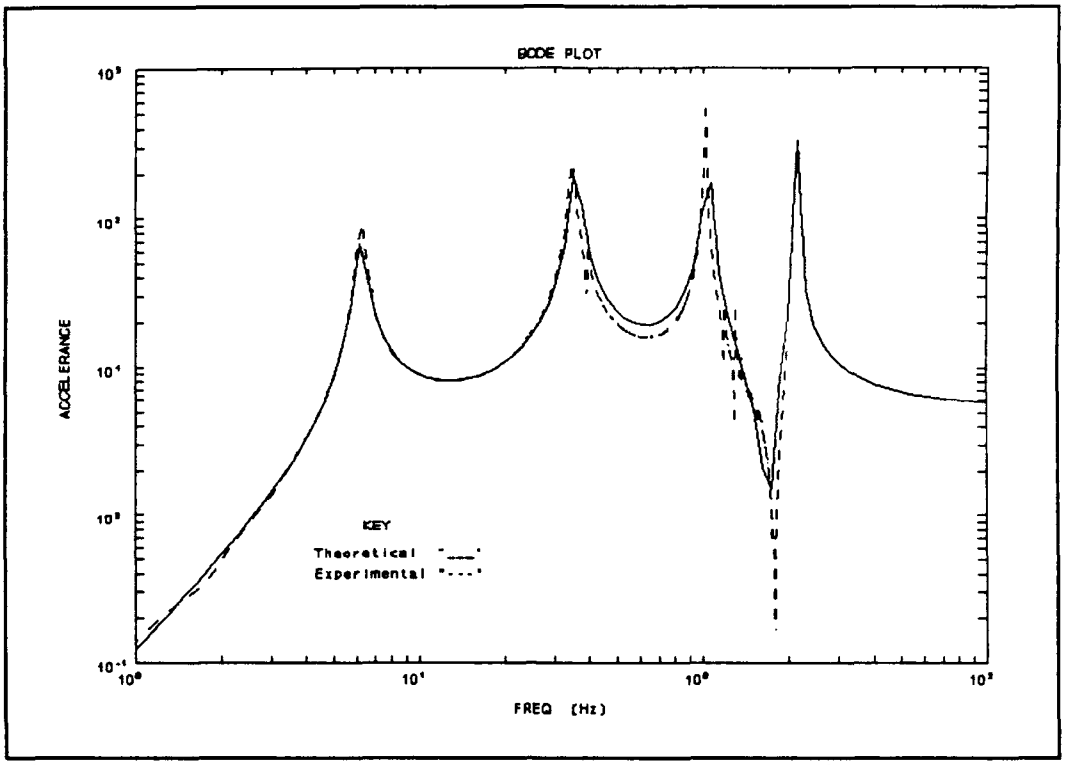


Figure 5.4 Open Loop Response for ACB with End Mass Removed for the Non-Collocated Sensor.

The effect of the blending ratio is determined by observing the open loop zero patterns as the blending ratio is increased as shown in Figure 5.5. The c's mark the zero locations for $\alpha = 0$ and the n's mark the $\alpha = 1$ locations. A value of $\alpha = 0.4$ corresponds to the point where the zeros coalesce on the imaginary axis. Blending ratios greater than this result in real valued zeros and hence a non-minimum phase system. For the beam with end mass installed, the maximum blending ratio was 0.85. Thus, the maximum blending ratio to maintain a minimum phase system is dependent on the modal information contained in the two

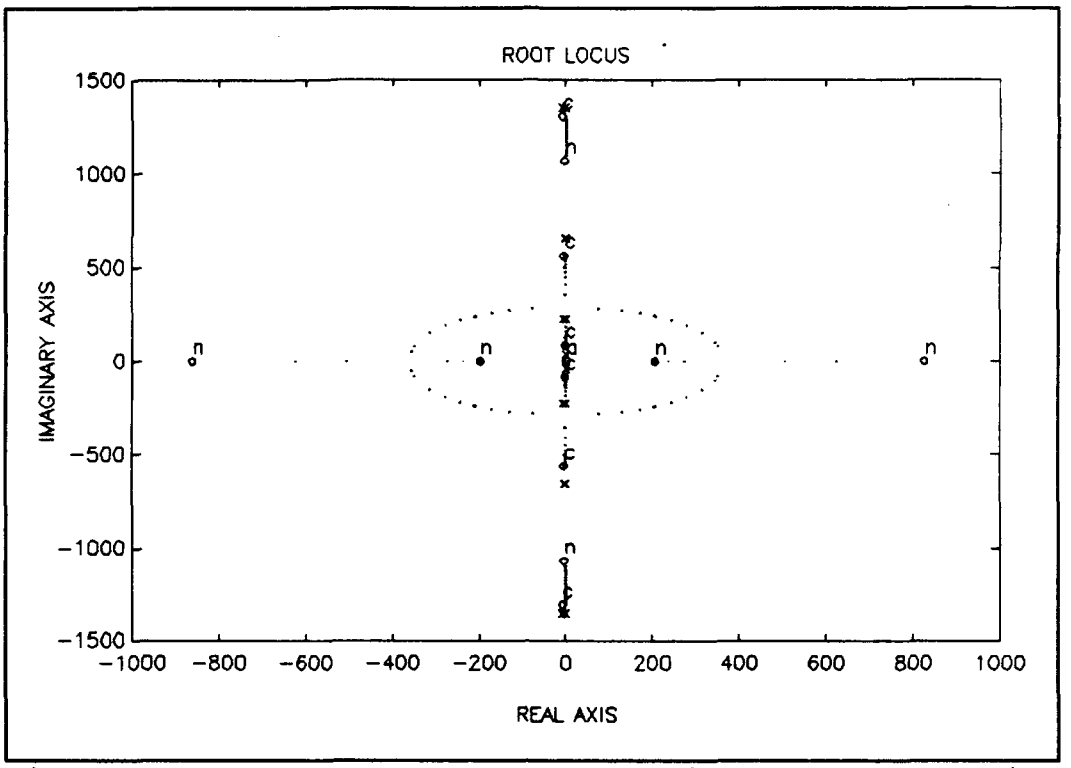


Figure 5.5 Open Loop Zero Locations for a Varying Blending Ratio.

sensor outputs. In both beam configurations, the second mode is the mode which goes unstable under non-collocated proportional feedback. With the end mass removed, the non-collocated sensor contains a greater percentage of mode two information and therefore the system will be NMP for a lower value of the blending ratio.

Closed Loop Results

As was done for the beam with end mass, RMS values of the position eight sensor were measured and plotted against

the proportional feedback gain. A 100 millivolt (0-200Hz) random disturbance was applied to the actuator while measuring the RMS response of position eight sensor for a varying feedback gain. The results are shown in Figures 5.6 and 5.7 for both the RMS response and the control effort. The theoretical results using Eqn 4.10 are shown for comparison. Unlike the results with the end mass in place, the RMS response is now very similar for the two cases. This is a result of the position eight sensor being located close to a node location for the second mode, as can be seen

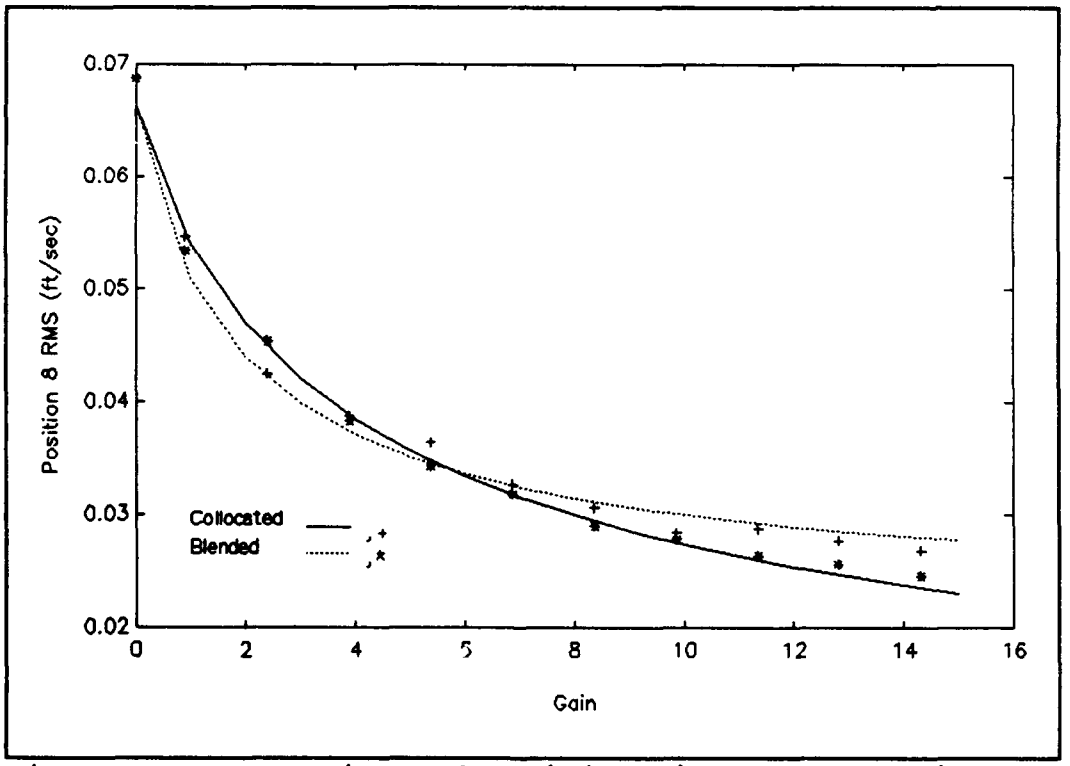


Figure 5.6 Comparison of Position Eight RMS Velocity for Collocated and Blended Feedback.

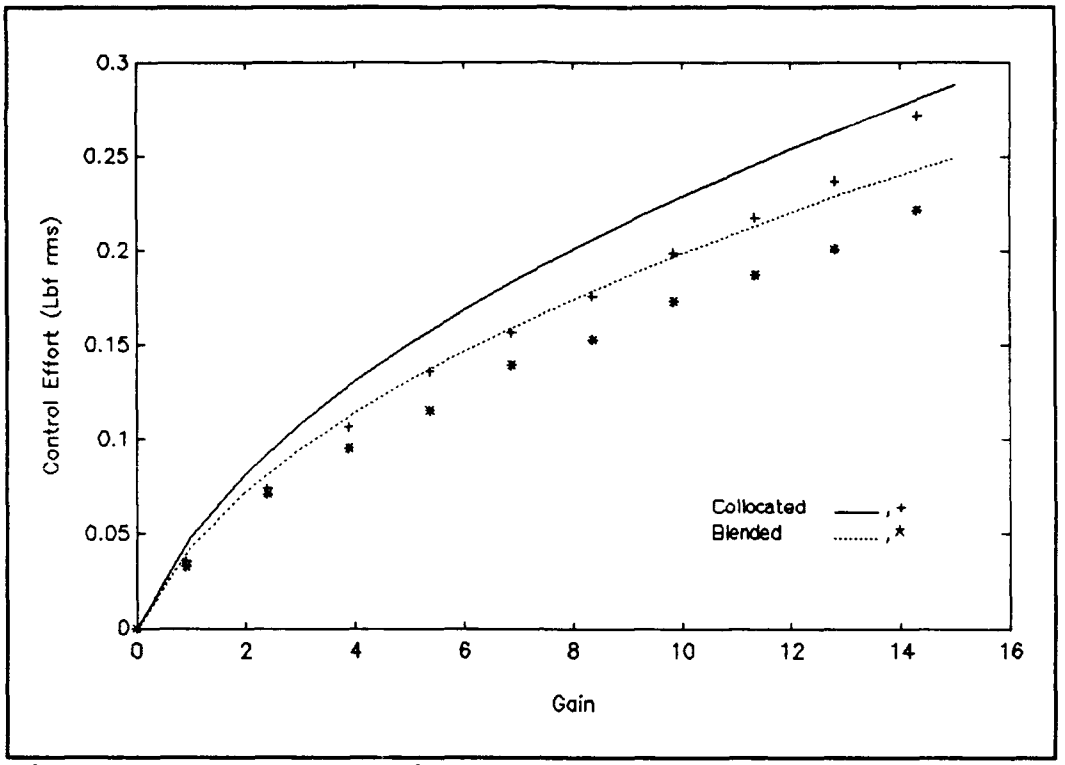


Figure 5.7 Comparison of Control Effort for an Increasing Feedback Gain.

in Figure 5.2. As a result, the near pole-zero cancellation which occurs for the second mode has little effect on position eight performance. The performance may be degraded, however, for other locations along the beam. For a blending ratio of 0.4 (maximum for NMP), the corresponding gains of k = 10 for the collocated and k = 8.8 for the blended were chosen. These values yield a theoretically matched RMS velocity response at position eight. Figure 5.8 shows the experimental closed loop comparison for the collocated and blended control laws. As shown in the plot for the same RMS level, the blended control exercises

greater control (higher damping) for mode one while being less effective for the second mode. Modal damping values obtained using STAR Modal are presented in Table 5.2.

Table 5.2 Damping Factors (%) for Matched RMS Response

	collocated		blended		open loop
mode	predicted	measured	predicted	measured	
1	18.0	17.7	33.4	31.9	3.26
2	21.7	24.0	2.48	3.2	2.50
3	3.58	3.30	4.73	3.5	0.60

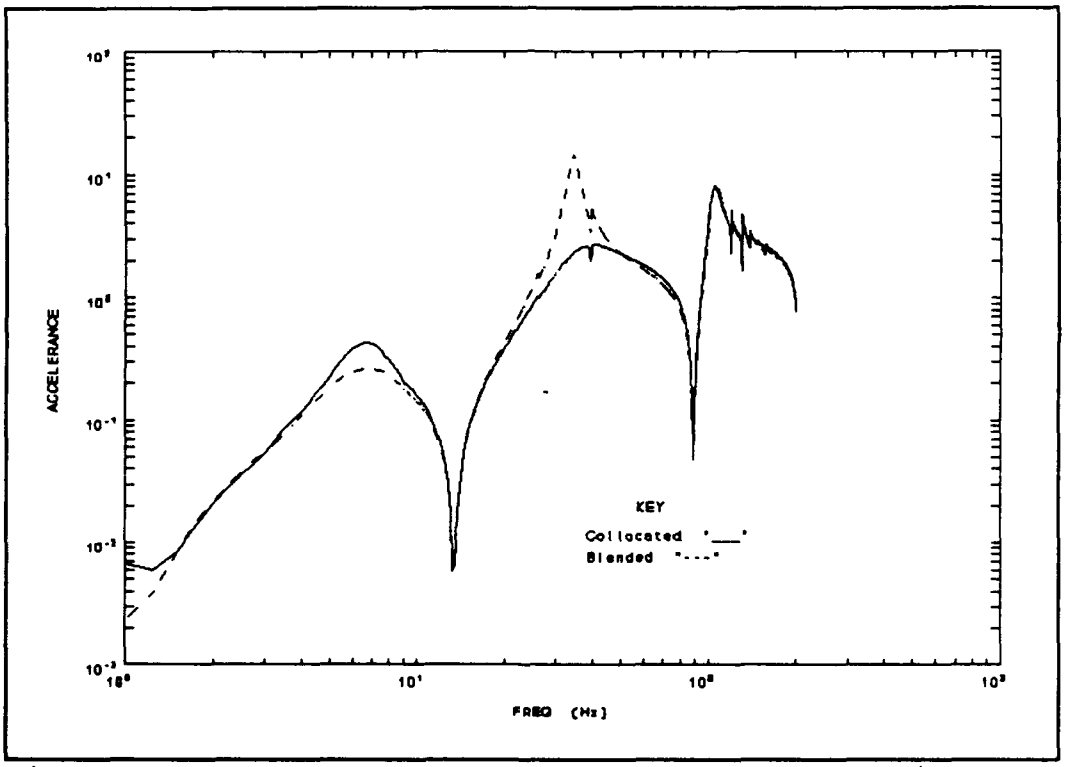


Figure 5.8 Closed Loop Frequency Response Comparison For the ACB Without End Mass.

Comparing the damping ratios using the blended and collocated measurements, similar behavior to the previous

example was exhibited. The blended measurement was extremely effective in damping mode one, while the near pole-zero cancellation at the second mode resulted in the second mode damping remaining at its open loop value. Again, the control effort for the blended was lower than the collocated case because of the notch at the second mode.

Conclusions

Closed loop control on the ACB without end mass was demonstrated for the two control laws. Choosing a blending ratio of 0.4 corresponded to the maximum achievable while maintaining a minimum phase system. For either a matched RMS response or a matched control effort, using the blended control laws enables an increase in the achievable mode one damping with a resulting decrease in ability to dampen mode two. For the ACB without the end mass, adequate control over the first three modes was exhibited using only a collocated sensor. Unless mode one damping was the only concern, little to no overall performance increase is achieved by incorporating the second non-collocated sensor.

Comparing this case to that of the beam with end mass, proper choice of the blending ratio for minimum phase behavior is dependent on the modal information available at each sensor. The blending ratio can be adjusted to yield

maximum mode one information while maintaining a minimum phase system. For a system where the non-collocated sensor contains different modal information than the collocated sensor, such as the beam with end mass, the blending method offers an alternative to increasing compensator complexity to achieve desired closed loop results.

The two cases considered demonstrated the advantages and disadvantages of using a blended measurement. Neither configuration of the beam, however, was a proper analogue to a gimbal structure, the prime focus of the investigation. Unfortunately, a physical gimbal was not available for experimental testing. In lieu of experimental testing on a gimbal, the next chapter will present a theoretical analysis using a blended measurement.

VI. Application of Blended Method to a Torsional Model

A last example of using a blended measurement is explored on a gimbal mechanism modelled as a free-free torsional rod. The torsional rod is analogous to the gimbal structure in that it has the rigid body motion and symmetric modes typical of a gimbal. Although a simple model is used, closed loop performance trends would be similar to those obtained with a more sophisticated model of an actual structure. A simplistic method of minimizing the line of sight errors on a gimbal was the primary reason for exploring the blended method.

Model Development

Using a six element FEM model, a state-space representation of the model was created using the method developed in Chapter III. Two degrees of freedom were modeled for each element corresponding to the axial rotation at each node. For the torsional rod, the mass and stiffness matrices are given as [8:389]:

$$M_{ij} = \frac{\rho I_p L}{6}\begin{bmatrix} 2 & 1 \\ 1 & 2 \end{bmatrix} \qquad K_{ij} = \frac{GJ}{L}\begin{bmatrix} 1 & -1 \\ -1 & 1 \end{bmatrix} \tag{6.1}$$

with ρ, I_p, L and GJ defined as the rod density, polar moment, length and torsional stiffness of the rod respectively. Three sensor locations were chosen for the output, one at each end of the model and one at the midpoint. The outputs at the ends represent the collocated and non-collocated rotation measurements. The midpoint rotation sensor represents the line of sight measurement. A torque input was applied at the first node.

The FEM results were compared to the exact solution by solving for the transfer function between the rotation at any point along the rod and a torque input at the end. The governing equation for a torsional rod in non-dimensional form is:

$$\frac{\partial^2\theta(x,t)}{\partial x^2} - \frac{\partial^2\theta(x,t)}{\partial t^2} = 0 \qquad (6.2)$$

Taking the Laplace transform of Eqn 6.2 and the boundary conditions yield:

$$\begin{gathered} \Theta^{ii}(x,s) + \lambda^2\Theta(x,s) = 0 \\ \Theta^{i}(1,s) = 0, \qquad \Theta^{i}(0,s) = T(s) \\ ()^{i}\Delta\frac{\partial()}{\partial x}, \qquad ()^{ii}\Delta\frac{\partial^2()}{\partial x^2} \\ \lambda^2\Delta - s^2 \end{gathered} \qquad (6.3)$$

It is then straightforward to assume a solution and solve for the constants. The resulting transfer function for an arbitrary location along the beam is given as:

$$\frac{\Theta(x,s)}{T(s)} = \frac{\sin\lambda\sin\lambda x + \cos\lambda\cos\lambda x}{\lambda\sin\lambda} \qquad (6.4)$$

For the collocated sensor, Eqn 6.4 reduces to:

$$\frac{\Theta(0,s)}{T(s)} = \frac{\cos\lambda}{\lambda\sin\lambda} \qquad (6.5)$$

and for the non-collocated sensor at the far end of the rod, the transfer function is given as:

$$\frac{\Theta(1,s)}{T(s)} = \frac{1}{\lambda\sin\lambda} \qquad (6.6)$$

It is clear from Eqn 6.6 that the exact solution has no real axis zeros, and therefore it is not truly a NMP system. Systems of this type, however, do exhibit NMP-like behavior [1].

A comparison of the pole-zero locations between the exact solution and the FEM is contained in Table 6.1. The zeros listed for the non-collocated case in the FEM model are a result of model truncation. The frequency response comparisons between the FEM and the exact transfer function are shown in Figures 6.1 and 6.2 for the two sensor

locations. The FEM accurately models the first few flexible modes and then deviates at higher frequencies as expected for a low order model.

Table 6.1 Pole-Zero Locations for a Torsional Rod

poles (rad/sec)		col zeros		non-col zeros	
exact	FEM	exact	FEM	exact	FEM
0,0	0,0	$\pm\pi/2i$	$\pm1.58i$	-	±14.7
$\pm\pi i$	$\pm3.18i$	$\pm3\pi/2i$	$\pm4.83i$	-	±14.7
$\pm2\pi i$	$\pm6.58i$	$\pm5\pi/2i$	$\pm8.42i$	-	±14.7

Similar to the blending used on the cantilevered beam, the two rotation sensors (velocity measurements were used

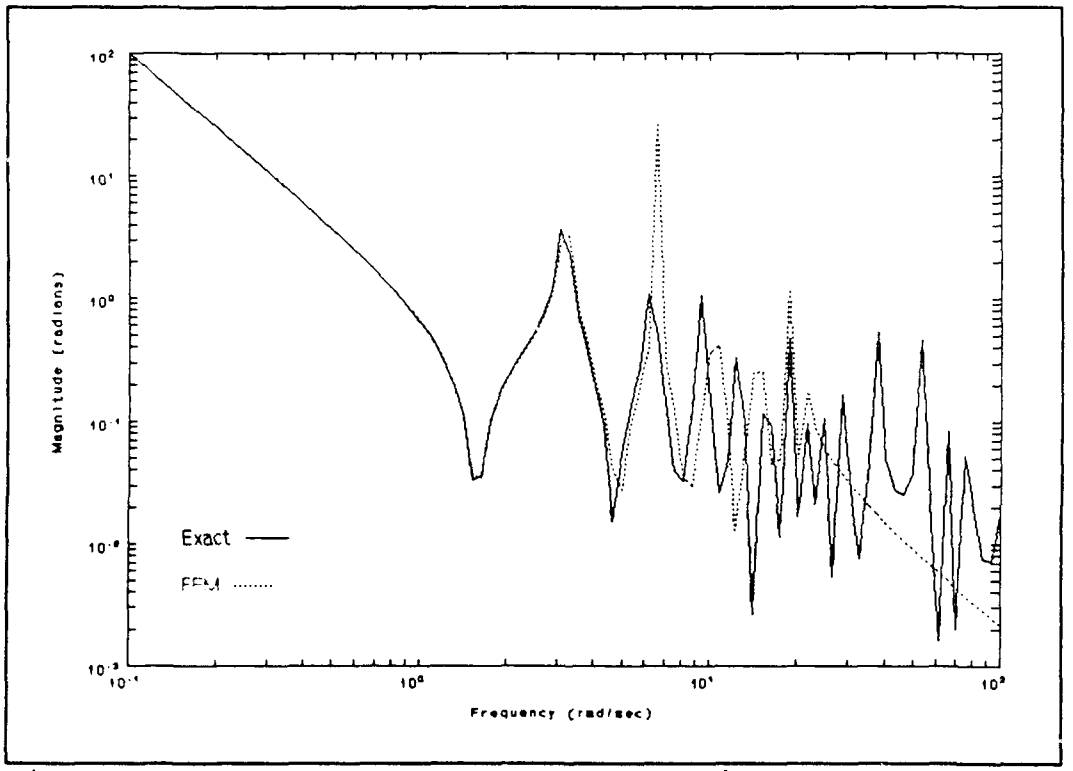


Figure 6.1 Frequency Response Comparison Between Exact and FEM Model for Collocated Sensor on a Torsional Rod.

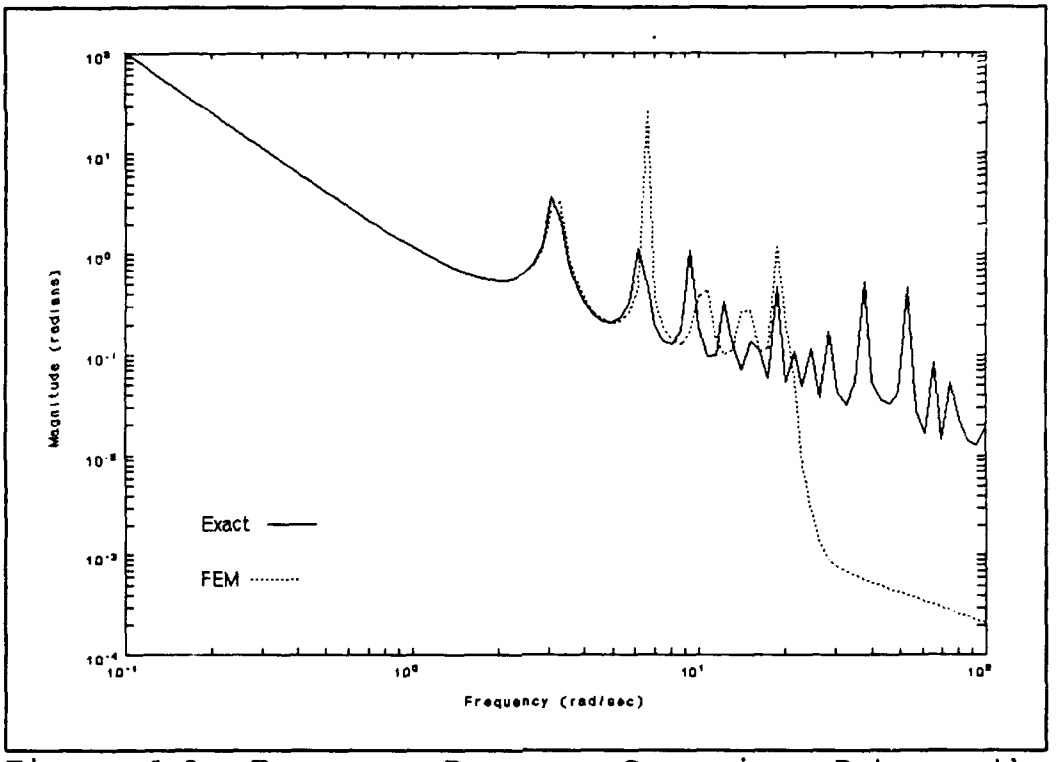


Figure 6.2 Frequency Response Comparison Between the Exact and FEM model for the Non-Collocated Sensor on a Torsional Rod.

with the beam) at each end of the beam were combined as the input to the controller as in Eqn 6.6.

$$\theta_{blend} = (1 - \alpha)\theta_{collocated} + \alpha\theta_{non\text{-}collocated} \qquad (6.6)$$

The pole-zero pattern as a function of the blending ratio is shown in Figure 6.3. As with previous examples, the blended system will remain minimum phase for a range of α. The maximum value of the blending ratio for a minimum phase system is $\alpha = 0.5$ which was expected due to the symmetry of the model.

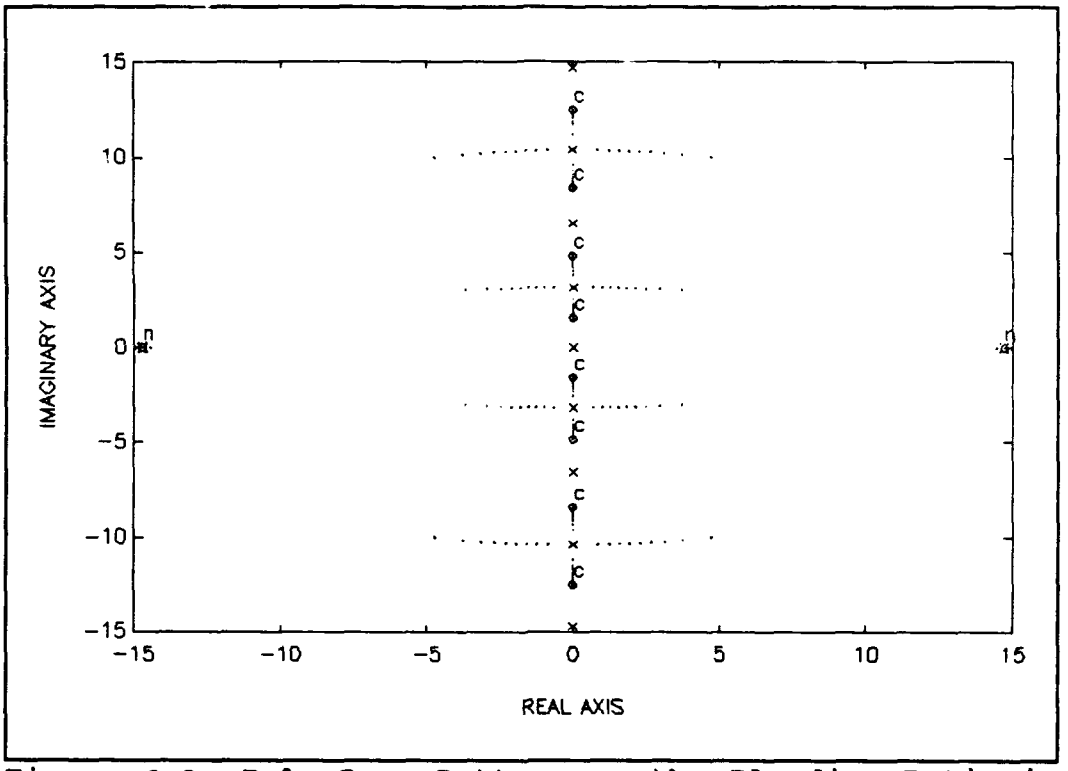


Figure 6.3 Pole-Zero Pattern as the Blending Ratio is Increased for a Torsional Rod.

Unlike the cantilevered beam, pure feedback of the position sensor will not stabilize the system because of the rigid body mode. As a minimum, a PD or lead compensator is required to stabilize the system. For comparison purposes on the rod model, a lead compensator will be used.

Closed Loop Performance Comparison

The lead compensator used takes the form of:

$$G_c(s) = k\frac{(s + z)}{(s + p)} \qquad (6.7)$$

where the zero (z) and the pole (p) are chosen to provide phase lead at the approximate bandwidth. For both the collocated and blended feedback, the values of z and p were set at 1 and 10, respectively, for a target bandwidth just past the first flexible mode. For comparison, the gain value k was set such that both the collocated and blended systems had an identical RMS response at the target bandwidth. A block diagram of the closed loop system is shown in Figure 6.4. MATLAB was used to compute the closed loop state-space models and compare the output response as a

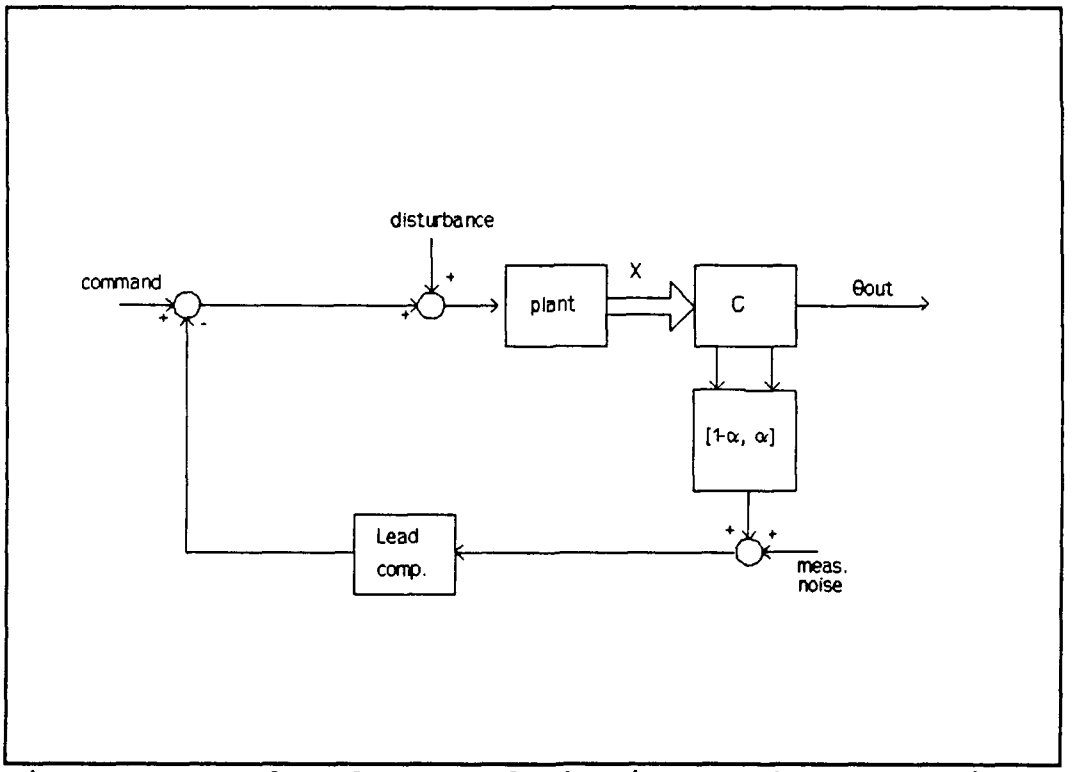


Figure 6.4 Closed Loop Block Diagram for a Torsional Rod.

function of the blending ratio. Computing the RMS response as detailed in Chapter IV, the resulting RMS response at the midpoint sensor is shown in Figure 6.5. The input disturbance was set at 0.1 with ten percent of the disturbance assumed as the measurement noise. As depicted in the figure, the RMS output is insensitive to the blending ratio while the system remains minimum phase ($\alpha < 0.5$). The insensitivity is a result of the midpoint sensor location being at a node for the symmetric modes of vibration. A gain of 10.5 was chosen for the comparison. This value

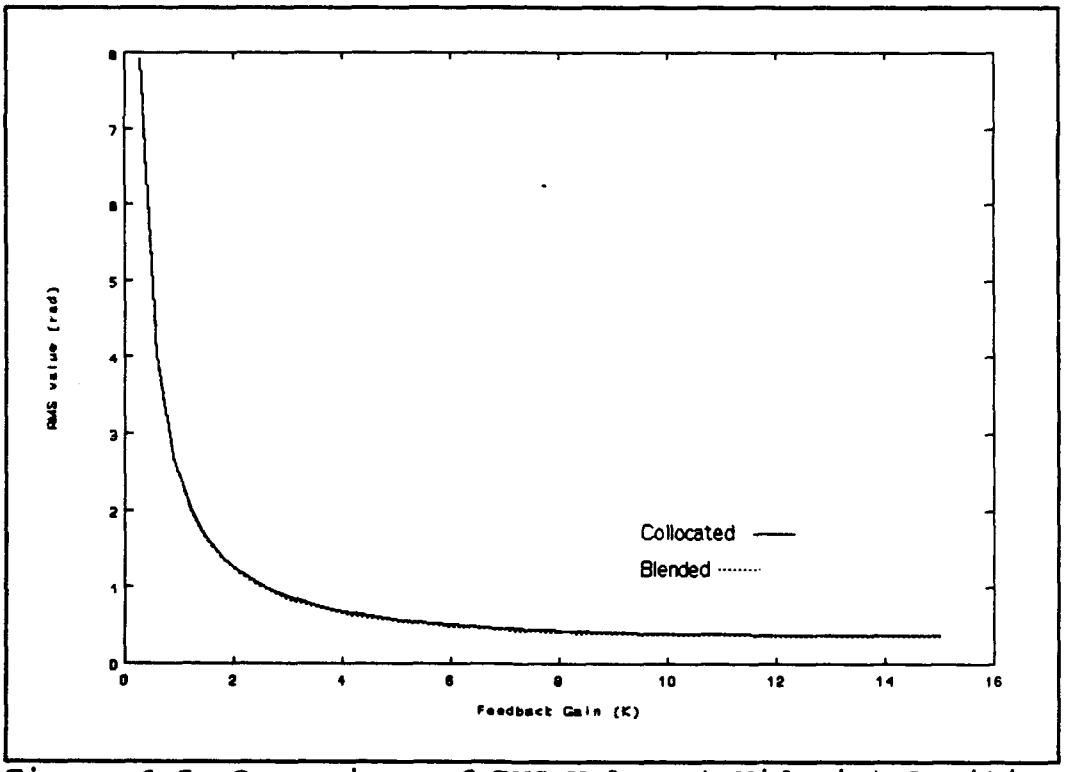


Figure 6.5 Comparison of RMS Value at Midpoint Position for Random Disturbance.

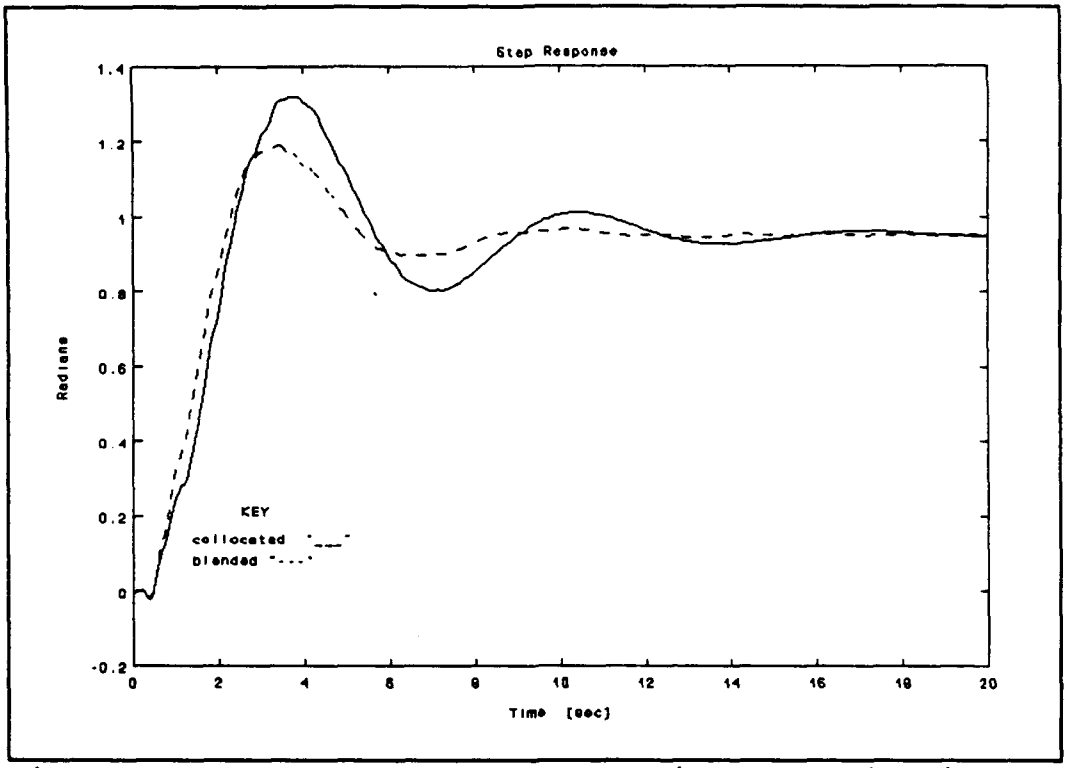


Figure 6.6 Step Response Comparison at Midpoint of Torsional Rod Using Collocated and Blended (α=0.45) Feedback.

represented an operating point where further gain increases did little to improve the RMS response. With the value of the gain chosen, the response to a unit step was compared as shown in Figure 6.6, and the resulting bandwidths in Figure 6.7. The results show the blended system has a faster rise time, a shorter settling time and slightly lower overshoot than the collocated system. There is also some increase in the bandwidth as shown in Figure 6.7, although the location of the first zero, which is identical for both systems, limits the achievable bandwidth increase as previously discussed.

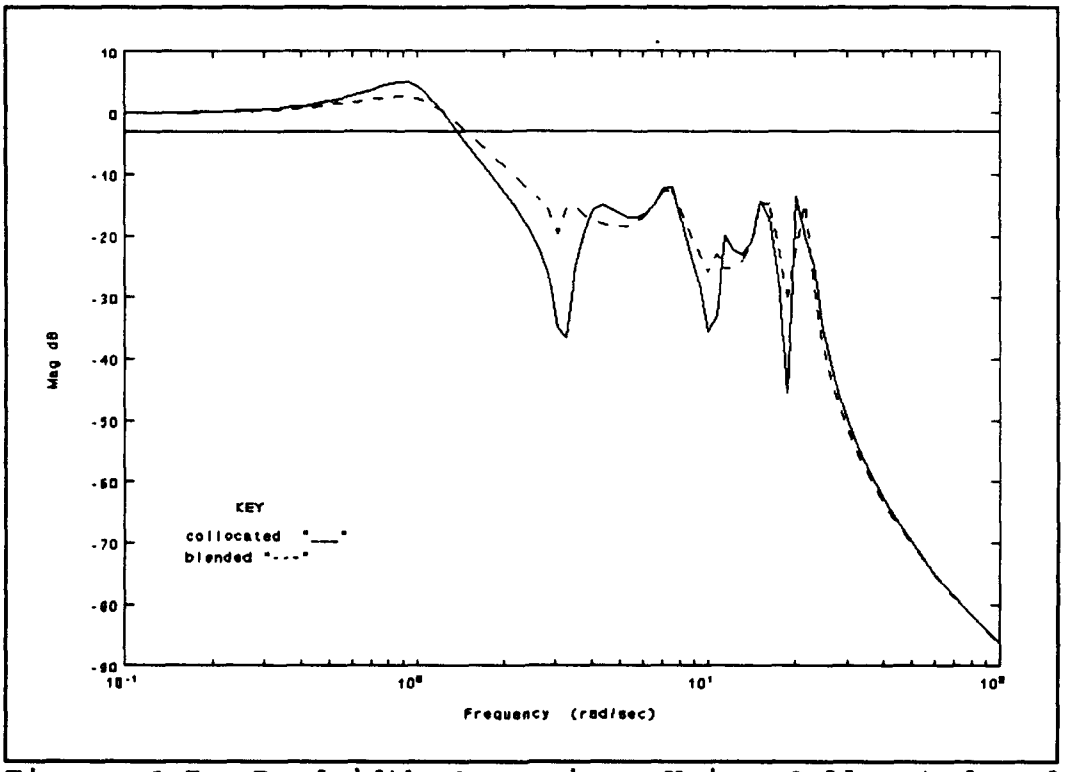


Figure 6.7 Bandwidth Comparison Using Collocated and Blended (α=0.45) Feedback on the Torsional Rod.

From the comparison presented, it appears that better tracking performance can be achieved using a blended measurement when comparing RMS levels, bandwidth, and the step response for the midpoint rotation. This result is somewhat misleading. For the midpoint location, there is a pole-zero cancellation at all the symmetric modes of the rod. Thus, the midpoint represents a node for all the even numbered flexible modes. As shown in the blended pole-zero patterns in Figure 6.3, the zeros coalesce at the even numbered poles and therefore the observation of the even numbered modes is decreased as the blending ratio is

increased. This results in the control effort being exerted on only the odd numbered modes which are the only modes that effect the midpoint rotation. For the ideal model with uncoupled modes and a blending ratio of .5, the midpoint can remain stationary while the ends of the rod oscillate undamped and undetected by the blended measurement. This situation is alleviated by reducing the blending ratio to provide some observation and consequently some damping of the even numbered modes. It is for this reason that α was set to 0.45 in the previous comparison plots. The differences in Figures 6.6 and 6.8 demonstrate how system

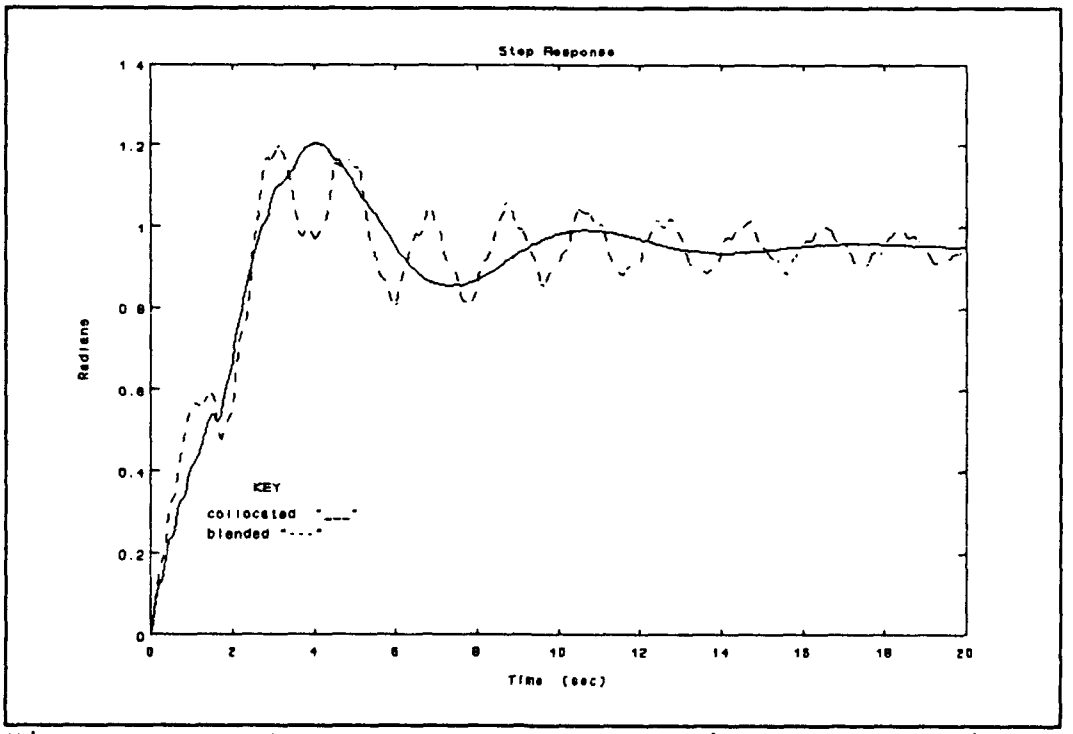


Figure 6.8 Step Response at End Point of a Torsional Rod.

performance is highly dependent on which sensor is chosen as the output, even though in the steady-state (with input removed), the final rotation angle will be identical for all locations along the rod.

Conclusions

A gimbal structure was modeled as a torsional rod and closed loop control was demonstrated using a lead compensator. For blending ratios of $\alpha < 0.5$, the system remained minimum phase. It was shown that a shorter settling time with less overshoot can be achieved using a blended measurement for the midpoint location while adversely effecting the rotational displacements at the ends. Choice of a proper blending ratio will be dependent on the RMS jitter requirements for several locations on the gimbal as well as the symmetry of the actual gimbal. In practice, the lightly damped modes which are nearly unobservable using the blended measurement are undesirable. In a physical model, some modal coupling will be present between modes which will cause the symmetric modes to excite the modes effecting the midpoint location. Due to the observability problems associated with the blended measurement, and no increase in achievable bandwidth nor

decrease in RMS levels, it appears the blended method is not attractive for implementation on an actual gimbal.

VII. Conclusions and Recommendations

An attempt to improve closed loop performance using feedback of the blended ratio of two separate measurements was investigated for several configurations. For all models tested, a blended measurement will yield a minimum phase system for a range of the blending ratio values. The range for which the minimum phase behavior can be maintained can be found by plotting the locations of the open loop zeros as the blending ratio is increased. It was shown that for a beam in bending, computing transmission zeros using an FEM accurately matched the exact solutions using transcendental transfer functions. The zero movement along the imaginary axis was illustrated on the ACB by measuring the frequency response of the blended output. Observing the blended locations of the antiresonances in the frequency response, the range of minimum phase behavior corresponds to the range of blending for which the antiresonances are separated.

The alternating pole-zero pattern on the imaginary axis which guarantees the stability of the collocated sensor/actuator also limits the achievable performance using the blended measurement. As the zeros move towards each other along the imaginary axis, they approach the poles

lying between them. This results in an observation problem for every other mode. The severity of the pole-zero cancellation is dependent on the blending ratio chosen. From the designer's perspective, adding an additional sensor to achieve unobservable modes is not an attractive result. There are configurations, however, where the blended method has its advantages.

As demonstrated in Chapter IV on the ACB with an end mass, the blended measurement represents a simple controller design alternative to using an estimator/regulator combination to adequately control first mode bending. If position control of the end of the beam was the primary concern, this represents an attractive alternative. Controlling the end position (or acceleration) of a flexible beam is a topic receiving considerable attention in the field of robotics and automation. Further investigation of the suitability of this technique to robotics applications should be investigated. A second possible application is in multi-input-multi-output systems where separate sensor/actuator sets can be assigned control of different modes. With proper placement and blending of the sensors and actuators, it may be possible to control all the modes adequately with this simple technique.

Focusing on the primary reason for this investigation, active control of a gimbal structure, neither the increased

bandwidth nor lower line-of-sight RMS levels thought possible at the start of the investigation was achieved. As illustrated in Chapter VI, increasing the contribution of the non-collocated sensor into the measurement leads to observability problems and degrades the performance at other locations on the gimbal.

Appendix A: Calibration Data

Actuator

To use the actuator for either excitation or control requires the computation of a calibration constant in terms of force out per voltage in. The manufacturer provided a calibration constant of 1.9 Lbf/amp (in current mode over the operating range 0-200 Hz). The APS-114 amplifier has a voltage monitor output which yields 4 amps out per volt monitored. The spectrum analyzer was used to obtain the transfer function of control voltage in to the APS-114 monitor voltage out of (.707volts/volt). In this way the total calibration was formed as the product of these three:

$$1.90 \frac{Lbf}{amp} \times 4 \frac{amp}{volt} \times 0.707 \frac{volt}{volt} = 5.37 \frac{Lbf}{volt} \quad (A.1)$$

As a check on the manufacturer's provided constant, a test was performed by mounting an accelerometer directly on the armature of the shaker with the armature unattached from the beam. In this configuration, there is essentially only rigid body motion. This configuration should yield a flat transfer function of accelerance over force. The governing

equation is then just F = ma, or using the measured values:

$$K_f E_f = m K_a E_a \qquad (A.2)$$

where m is the mass of the armature plus accelerometer, K_a is the accelerometer constant, E_f and E_a are the measured voltages of the force and acceleration respectively, and K_f is the desired force constant. Solving for K_f yields:

$$K_f = \left(\frac{E_a}{E_f}\right) m K_a \qquad (A.3)$$

where the ratio of the voltages is the measured value of the transfer function. Using this method and taking an average value of the transfer function over the frequency range produced a calibration constant of 5.4 Lbf/volt and thus the manufacturer's value was accepted as the correct calibration constant.

Accelerometers

The piezo-resistive accelerometers have the advantage of recording dc levels and thus the calibration is obtained by simply reading the output voltage with the accelerometer in the upright position and then taking a second reading in the inverted position. The resulting voltage change

corresponds to a 2g acceleration. The three accelerometers were calibrated in this way with the following results. For all calibrations and tests, the signal conditioner gains were set at 50.

Table A.1 Accelerometer Calibrations

serial #	position	Volt/g	ft/s^2/volt
AH72	5	.885	36.35
BA26	8	.982	35.67
BA51	11	.902	32.78

The above calibrations were assumed constant over the operating range. To verify this assumption the accelerometers were checked against an Endevco accelerometer standard. During this test, both the tested accelerometer and the standard are excited at a known frequency, and the tested accelerometer is then compared against the standard. Although there was some frequency dependance noted, using the constants given above represented an average value over of the operating frequency range.

Integration Circuits

As previously described, the integration circuits contained several stages of amplification between the output

of the accelerometer and input to the digital controller. Rather than calibrate each stage individually, a single calibration constant was obtained by taking the transfer function of the entire integration circuit over the frequency range of interest. The overall circuit gain for an integrator is computed by dividing the measured gain at a given frequency by the frequency (in rad/sec). For an ideal integrator, this value is a constant. An average value of the gain in the 1 - 200 Hz frequency range for each measurement channel is listed in the table below.

Table A.2 Integration Circuit Calibration Factors

position	pre-amp	post-amp	total gain (v/v sec)
5	5	20	64.5
8	5	20	57.4
11	5	20	60.3

To correlate gain values used in the digital controller to those used in modelling, it is simplest to set the reciprocal of the velocity and force calibrations at the PC-1000 input and output channels. For the velocity measurements, values from Table A.1 and A.2 are combined. The reciprocal is then set as the input gain factor to the PC-1000. The PC-1000's output attenuation factor for the shaker is set to the reciprocal of the force calibration constant.

Appendix B: State-Space Models

ACB With End Mass

A =

Columns 1 through 4

0	0	0	0
0	0	0	0
0	0	0	0
0	0	0	0
-6.3541e+005	0	0	0
0	-1.7430e+005	0	0
0	0	-2.2931e+004	0
0	0	0	-1.7341e+002

Columns 5 through 8

1.0000e+000	0	0	0
0	1.0000e+000	0	0
0	0	1.0000e+000	0
0	0	0	1.0000e+000
-9.5655e+000	0	0	0
0	-5.0099e+000	0	0
0	0	-3.6343e+000	0
0	0	0	-2.6337e-001

B =

0
0
0
0
-4.6102e+000
1.0464e+001
7.6929e+000
5.7942e-001

C =

Columns 1 through 4

0	0	0	0
0	0	0	0
0	0	0	0

Columns 5 through 8

-2.4803e-001	5.7156e-001	8.1911e-001	2.0786e-001
6.5142e-001	-3.9427e-001	8.9463e-001	5.5993e-001
-4.2821e-002	1.8246e-002	-1.2273e-001	1.0000e+000

ACB Without End Mass

A =

Columns 1 through 4

0	0	0	0
0	0	0	0
0	0	0	0
0	0	0	0
-1.8288e+006	0	0	0
0	-4.3118e+005	0	0
0	0	-5.0910e+004	0
0	0	0	-1.5319e+003

Columns 5 through 8

1.0000e+000	0	0	0
0	1.0000e+000	0	0
0	0	1.0000e+000	0
0	0	0	1.0000e+000
-1.6228e+001	0	0	0
0	-7.8798e+000	0	0
0	0	-1.1282e+001	0
0	0	0	-2.5519e+000

B =

0
0
0
0
8.2318e+000
1.2985e+001
-1.2786e+001
4.9621e+000

C =

Columns 1 through 4

0	0	0	0
0	0	0	0
0	0	0	0

Columns 5 through 8

1.3231e-001	3.0766e-001	-6.6519e-001	2.3091e-001
-2.0014e-001	-5.1377e-001	-2.7479e-001	5.9141e-001
4.8728e-001	7.2424e-001	1.0000e+000	1.0000e+000

Appendix C: MATLAB FEM Program

```
function [A,B,C,D]=bildabcd(E,mplate)
%
%  function [A,B,C,D]=bildabcd(E,mplate)
%  This program returns the state-space model for a ten
%  element cantilevered beam in bending.  The states
%  represent the velocity measurements at the nodes
%  The modulus and the end mass are input to match exp data.
%  The length of the tenth element is 1 inch longer due to
%  the plate thickness.
%

kbig=zeros(22,22);
mbig=zeros(22,22);
p=5.3727;
a=5.3932e-3;
l=0.58958;
l10=.63125;
iz=3.31115e-6;

mgen=[156,22*l,54,-13*l;
22*l,4*l*l,13*l,-3*l*l;
54,13*l,156,-22*l;
-13*l,-3*l*l,-22*l,4*l*l];

kgen=[12,6*l,-12,6*l;
6*l,4*l*l,-6*l,2*l*l;
-12,-6*l,12,-6*l;
6*l,2*l*l,-6*l,4*l*l];

mgen10=[156,22*l10,54,-13*l10;
22*l10,4*l10*l10,13*l10,-3*l10*l10;
54,13*l10,156,-22*l10;
-13*l10,-3*l10*l10,-22*l10,4*l10*l10];

kgen10=[12,6*l10,-12,6*l10;
6*l10,4*l10*l10,-6*l10,2*l10*l10;
-12,-6*l10,12,-6*l10;
6*l10,2*l10*l10,-6*l10,4*l10*l10];

kel=(E*iz/l^3)*kgen;
mel=(p*a*l/420.)*mgen;

kel10=(E*iz/l10^3)*kgen10;
mel10=(p*a*l10/420.)*mgen10;
```

```
for I=1:2:17
   mbig(I:I+3,I:I+3)=mbig(I:I+3,I:I+3) + mel;
   kbig(I:I+3,I:I+3)=kbig(I:I+3,I:I+3) + kel;

mbig(19:22,19:22)=mbig(19:22,19:22)+mel10;
kbig(19:22,19:22)=kbig(19:22,19:22)+kel10;

% add lumped masses
mbig(21,21)=1.9426e-3 + mbig(21,21) + mplate;
mbig(22,22)=mplate*.0630787 +mbig(22,22);
mbig(15,15)=1.9426e-3 + mbig(15,15);
mbig(9,9)=21.4610e-3 + mbig(9,9);

% partition matrix
M=mbig(3:22,3:22);
K=kbig(3:22,3:22);

% put in state-space form
[phi,lam]=eig(K,M);
wn2=diag(diag(inv(M*phi)*K*phi));
A=zeros(40,40);
A(21:40,1:20)=-wn2;
B=zeros(40,1);
Cp=zeros(3,20);
F=zeros(20,1);
F(7,1)=1;
B(21:40,1)=inv(M*phi)*F;
Cp(1,7)=1;
Cp(2,13)=1;
Cp(3,19)=1;
A(1:20,21:40)=eye(20);
C=zeros(3,40);
C(:,21:40)=Cp*phi;
D=zeros(3,1);
```

Appendix D: Analog Gain Control

To accommodate different feedback gains without having to reprogram the PC-1000, an analog adjustable gain circuit was built. This circuit was used to measure output and control levels as a function of the feedback gain. The circuit consists of an amplifier and an adder as shown in Figure D.1. The gain was set by varying the value of the feedback resistor using a decade resistor box. The adder is placed after the amplifier to enable the addition of the random input without amplifying the random signal. This circuit was used in series with the PC-1000. The velocity measurements were calibrated and blended using the PC-1000 and then amplified using the analog circuit.

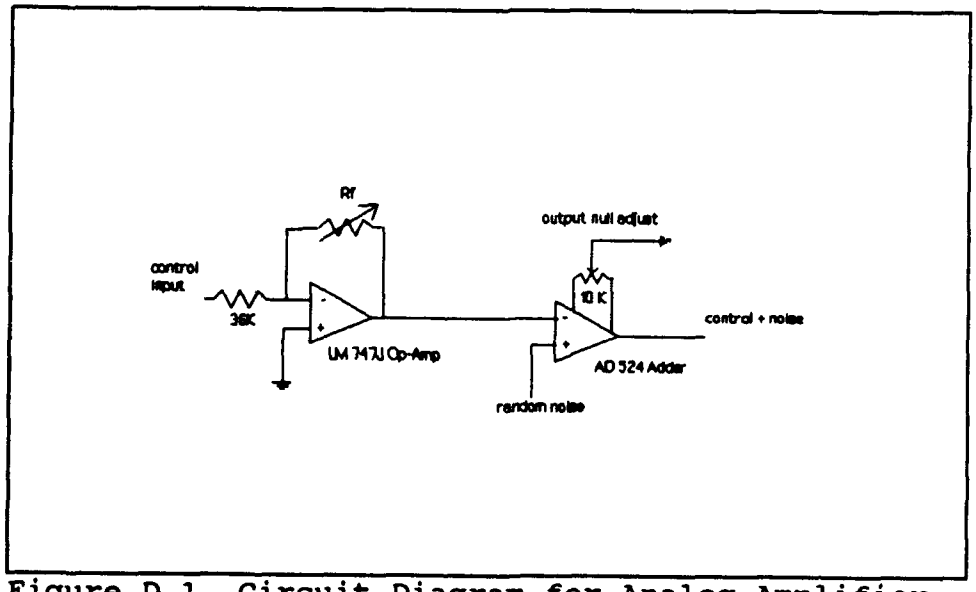


Figure D.1 Circuit Diagram for Analog Amplifier.

The calibration constant of the shaker was included when calculating the amplifier gain. The calibration curve is shown in Figure D.2.

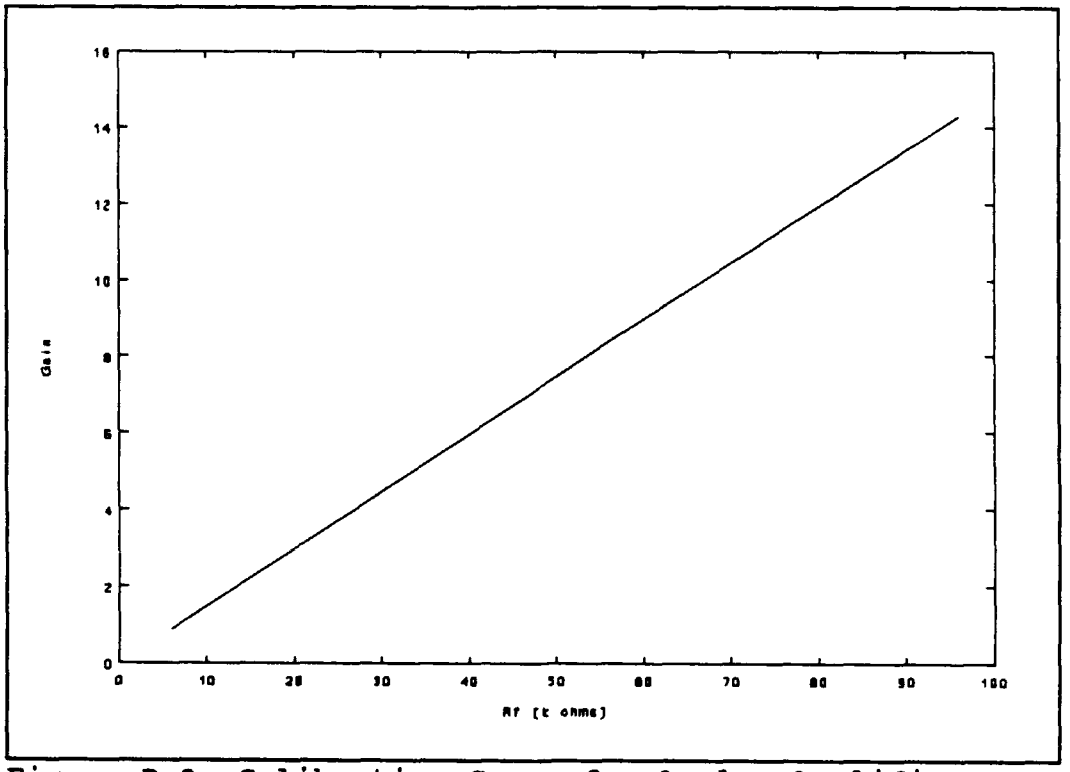


Figure D.2 Calibration Curve for Analog Amplifier.

Bibliography

1. Lee, W. C. Effects of Colocation and Non-Colocation of Sensors and Actuators on Flexible Structures, MS Thesis, Air Force Institute of Technology, Wright-Patterson AFB OH, 1991.

2. PC-MATLAB, Sherborn, MA: The Mathworks Inc., 1992.

3. Rao, S. V. and M. Westerheide. "Reduced Order Robust Controllers for an Experimental Flexible Grid", 1990 American Control Conference, San Diego CA, May 23-25, 1990.

4. Misra, P. "On the Control of Non-Minimum Phase Systems", 1989 American Control Conference, Pittsburgh PA, June 21-23, 1989.

5. Park, Jahng-Hyon and Haruhiko Asada. "Design and Control of Minimum Phase Flexible Arms with Torque Transmission Mechanisms", 1990 IEEE International Conference on Robotics and Automation, Cincinnati OH May 13-18, 1990.

6. Junkins, L. Mechanics and Control of Large Flexible Structures, American Institute of Aeronautics and Astronautics, 1990.

7. Lim, K. B. "A Method for Optimal Actuator and Sensor Placement for Large Flexible Structures", AIAA Guidance, Navigation and Control Conference, Portland OR, August 20-22, 1990.

8. Craig, Roy R. Structural Dynamics, An Introduction to Computer Methods, New York: John Wiley & Sons, 1981.

9. Wie, Bong and Arthur E. Bryson, Jr. "Modeling and Control of Flexible Space Structures", Dynamics and Control of Large Flexible Spacecraft: Proceedings of the Third Symposium, Blacksburg VA, June 15-17, 1981.

10. Wolfram, Stephen. Mathematica: A System for Doing Mathematics by Computer. Redwood City CA:Addison-Wesley, 1988.

11. Timeshenko, S and others. Vibration Problems in Engineering. New York: John Wiley & Sons, Inc., 1974.

12. Martin, Gary D. On the Control of Flexible Mechanical Systems, PhD dissertation, Dept of Aeronautics and Astronautics, Stanford University, Stanford CA, May 1978.

13. Jacques, David R. Baseline Experiment for Active Control of Structural Vibrations, MS Thesis, Air Force Institute of Technology, Wright-Patterson AFB OH, 1989.

14. PC-1000 Systolic Array Processor Operations Manual, Systolic Systems Inc., Campbell CA, 1988.

15. Tektronix 2642A Operating Manual, Tektronix Inc. Campbell CA, 1991.

16. Star Modal Operating Manual, Structural Measurement Systems Inc., San Jose CA, 1992.

17. McCall, Robert C. Experimental Feedback of Fractional Order States of a Lightly Damped Structure, MS Thesis, Air Force Institute of Technology, Wright-Patterson AFB OH, 1992.

18. Cristler, Thomas. Active Vibration Control of a Cantilevered Beam with Three Elastic Coordinates, MS Thesis, Air Force Institute of Technology, Wright-Patterson AFB OH, 1987.

19. Yang, David L. Fractional State Feedback Control of Undamped Viscoelastically-Damped Structures, MS Thesis, Air Force Institute of Technology, Wright-Patterson AFB OH, 1992.

20. Acoustic Power Systems. Instruction Manual - Electro-Seis Model 113-LA Shaker, Carlsbad CA 1989.

21. Hallauer, W. L. and G. R. Skidmore. "Active Vibration Damping Experiments at VPI & SU: Overview and Recent Results", Dynamics and Control of Large Flexible Spacecraft: Proceedings of the Third Symposium, Blacksburg VA, June 12-14, 1985.

22. Franklin, Gene F. and others. Feedback Control of Dynamic Systems, New York: Addison-Wesley, 1991.

23. Kwakernaak, H. and R. Sivan. Linear Optimal Control Systems New York: Wiley-Interscience, 1972.

24. Ridgely, D. Brett and Siva S. Banda. Introduction to Robust Multivariable Control. AFWAL -TR-85-3102. WPAFB OH: Control Dynamics Branch, Flight Dynamics Laboratory, September 1985. (AD-A165891)

25. Reid, J. Gary. Linear Systems Fundamentals. New York: McGraw-Hill Book Company, 1983.

Vita

Captain Richard G. Cobb was born on 9 January 1958 in Queens, New York. He entered the Air Force in September 1981. While serving as a weapons control system specialist on F4-D aircraft at Homestead AFB, he was selected for the Airman Education and Commissioning Program. He graduated top of his class from the Pennsylvania State University's Aerospace Engineering Department in May, 1988. After commissioning, he served as the Global Positioning System's (GPS) launch operations officer at Cape Canaveral AFS where he managed daily operations leading to the successful launch of the first ten Block II GPS satellites. Captain Cobb entered the Air Force Institute of Technology in June 1991. He married Lisa Cordeiro in September of 1982, and has two sons, Gregory and Ryan.

Permanent Address: 808 Grace Street
Baldwin, NY 11510